Electrochemical and Structural Analysis of Li-ion Battery Materials by *in-situ* X – Ray Absorption Spectroscopy

by

Soojeong Kim

A dissertation submitted in partial fulfillment
of the requirements for the degree of
Doctor of Philosophy
(Chemistry)
in the University of Michigan
2015

Doctoral Committee:

Professor James E. Penner-Hahn, Chair
Associate Professor Bart M. Bartlett
Professor Mark E. Meyerhoff
Professor Levi T. Thompson Jr

© Soojeong Kim

2015

To my parents, Taegon and Meesook, with the utmost gratitude for their unconditional love and support.

With all my love, always.

ACKNOWLEDGEMENTS

First of all, I am indebted to my Ph.D. advisor, Professor James E Penner-Hahn, for his guidance during my graduate studies in Michigan. The primary reason I was able to conduct this research and prepare this dissertation is because I selected an advisor who truly cares about his students and who has gone to extraordinary lengths to help us succeed. I am deeply grateful for the time he spent to educate me as a scientist, and for his endless encouragement. I am proud to come from his lab knowing that I am ready to tackle any challenge, and I am eager to see what exciting science emerges from the Penner-Hahn group in the near future.

Second, I appreciate all the help provided by Dr. Aniruddha Deb, a research scientist in our group. Aniruddha taught me electrochemistry from the beginning when I first join Penner-Hahn group. He helped me a lot and provided me great opportunities and a good atmosphere for doing research about lithium ion batteries. Aniruddha and Jim both gave me much heartwarming encouragement which allowed me to get over all the difficulties that I faced during my graduate studies. Without both Jim and Aniruddha's support, I would not be able to overcome all the difficulties that I faced during my graduate studies.

Also I appreciate all the help provided by Prof. Bart Bartlett, Prof. Mark Meyerhoff, and Prof. Levi Thompson as my committee members. I sincerely appreciate their feedback and encouragement during my candidacy exam and data meeting. Without their support I could not finish my Ph.D. studies. I would like to thank Prof. Goodson, Prof. Lim, Prof. Maldonado for

giving me a chance to do my rotation opportunity in their lab and those opportunities gave me a thought what I really want to do for research. It was great experience.

I also would like to thank Prof. Monroe from chemical engineering department for giving me a chance to use a glove box in his research lab. I do appreciate all the support from Monroe group; Lucas, James, and Lin; I especially appreciate help from Lucas who helped me a lot with accessing glove box.

I owe special thanks to my fellow lab member Andrew Crawford. Our friendship went beyond the science. I would like to thank Andrew, who will be doctor soon, for being a supportive friend and colleague who always encouraged me when I needed it. Also, I do appreciate his help with programing work; even though our research topics and techniques were different, his comments and feedback were really helpful.

It would have been impossible for me to have made it this far without the most wonderful family and friends. There are too many people to name, but they know who they are and they are the best. I have to thank my best friend Dr. Jiyoung Hong, for being a great friend here at Michigan. I will keep our friendship forever. I also have to thanks Dr.Jenny Jinjoo Jeong one of my best friends in Ann Arbor, for everything she has done for me. Her continued friendship through our (almost) daily chats helped make me feel not too lonely. And I also appreciate endless support and heartwarming words from Catholic Church members J.D. Sunho Yoon, Dr. Youngki Kim couple, Okjae Lee, Dr. Kyubum Kim, Dr. Annette Cho, and Dr. Yongsoo Yang, who cared me a lot and shared good memories together by entertaining and supportive messages over the years. I also appreciate from Jiyeon Song and Soonam Lee for understanding what it is like to be in grad school and chatting together. Special thanks to my high school friends in

Korea, Narae Eun, Junghyun Park, Wonmi Yang, Minkyoung Kwak, and Juyeon Kim, who support me all the time via text messages and phone calls. Your emotional support, helped me to resist this long journey.

To my brother, Dohyeun, thank you for being my closest confidant over the years. You are such an inspiration to me and I am very lucky and proud to call you my brother.

Finally, I want to thank my parents. I am convinced that if you have people like these that love you, nothing could be impossible. Mom and Dad, words could never ever express how lucky I am to have you as parents. Thank you for being the best role models for who I wanted to become, for always believing in me, for giving me perspective on things when I could only see right in front of me. Finally, thank you for coming to visit me as often as you did. Those visits were always so much fun and made the next stretch of time more efficient. I love you both and will love you forever.

Table of Contents

List of Tables

List of Figures

Abstract

Efficient inexpensive energy storage is essential for widespread adoption of alternatives to fossil fuels. Lithium-ion batteries are a promising technology for energy storage. This dissertation describes the electrochemical and local structural analysis of the Li-ion cathode/anode materials $Li_4Ti_5O_{12}$, $LiMn_2O_4$, $Li_3V_2(PO_4)_3$, and Mg-doped $Li_3V_2(PO_4)_3$) using synchrotron-based X-ray Absorption Spectroscopy (XAS). For the well-known anode material $Li_4Ti_5O_{12}$, XAS provides an explanation for the ‘‘Zero-strain’’ characteristic of the material; there is, as expected, an increase in Ti-O distance reduction but no change in Ti-Ti distance, consistent with the added lithium pulling the oxide anions closer together, allowing the Ti-O distance to expand, with negligible change in the lattice parameter. XAS showed that when the spinel $LiMn_2O_4$ cathode is annealed, there is a slight increase in the average Mn oxidation state. *In-situ* XAS studies of another cathode material, $Li_3V_2(PO_4)_3$, showed the presence of significant kinetic effects such that the measured electrochemical behavior does not represent the bulk vanadium. There are only two distinct vanadium species when the cathode is cycled between 3.0 and 4.5 V. However, when the potential exceed 4.5 V a third vanadium species is formed, consistent with the formation of V^{5+}. The data suggest that a portion of the V^{5+} can migrate to empty Li sites, indicating a possible explanation for capacity loss at high potential. If a portion of the V is replaced with Mg giving $Li_3V_{(2-2/3x)}Mg_x(PO_4)_3$, the electrochemical performance, cycling

retention and stability increase up to X~0.30. *In-situ* XAS of $Li_3V_{(2-2/3x)}Mg_x(PO_4)_3$, x=0.15, 0.30, and 0.45 was used to characterize the structural and electronic consequences of Mg doping. In general, the doped cathodes behave similarly to the undoped parent material, with oxidation of V^{3+} to V^{4+} over 3 – 4.5 V and for the oxidation to V^{5+} at higher potential. As in the undoped material, we see substantial migration of V^{5+} to Li sites, and find evidence, especially for x = 0.15, that this tetrahedral V can be reduced to V^{4+} without returning to the octahedral V site. The most important consequence of doping seems to be a decrease in the kinetic lag that is seen in the undoped material.

CHAPTER I

LITHIUM ION BATTERIES & TECHNIQUES FOR CHARACTERIZING THEM

1.1 INTRODUCTION

Most of the electrical energy used in the world is currently supplied from fossil fuels. Therefore, measures are being adopted in a variety of different fields to help prevent global warming by reducing CO_2 emissions. As a result, the automotive industry has become a focal point when considering the impact of fossil fuel use on the environment. The lithium-ion battery has attracted attention due to its potential for use in hybrid electric vehicles. More importantly, advances in environmental technology, such as the emergence of hybrid electric vehicles in the 1990's, have brought innovation to an era when vehicles have been traditionally powered by gasoline. The key feature of hybrid technology is surrounded by the augmentation of the engine with an electric motor, ultimately achieving improved fuel economy and significantly reducing the amount of CO_2 produced by the burning of fossil fuel. Remarkable efforts have been made in the energy industry to develop alternatives such as solar cells, fuel cells, biofuels and batteries and demand for advanced technology and better energy storage devices has been significantly increasing each year for the past decade. Although motivated by a variety of different needs, the new technologies all consider the potential benefits for our technologically driven, highly mobile and energy challenged society. Especially, lithium-ion batteries have already become widely

used for laptops, cameras, cell phones, etc., and also have gained attention in the consumer market due to their light-weight and rechargeable properties.

1.2 Battery Application

Several electrical energy storage and conversion devices have been considered for use in vehicle applications. Recently, electrochemical systems have been considered as the power sources for hybrid electric vehicles (HEVs). HEVs combine two different systems, an internal combustion engine (ICE) with an electric vehicle (EV) in which an electric motor enables the secondary power supplies. This combination provides better gasoline mileage compared to the typical ICE vehicle, leading to decreased gasoline consumption of HEVs of about 30% compared to usual vehicles.[1] Plug-in hybrid electric vehicles (PHEVs) take this concept one step further by adding additional batteries to the original design. This allows the vehicle to be charged during the night time and being fully powered by stored electric energy during the day time.

General characteristics for different battery applications are displayed in the Ragone plot, as shown in **Figure 1.1**, where the x-axis is a specific power (more acceleration with the same weight) and the y-axis is specific energy (more miles with the same weight). The graph shows these quantities for various batteries, electrochemical capacitors, and fuel cells. The best performance for all three applications is in the lithium-ion system, although the Ni/MH system meets the U.S. Department of Energy's (DOE) goal[2-4] for the hybrid-electric vehicle (HEV) application.[5-7] The figure also shows that none of the batteries has the ability to provide energy close to what is possible with gasoline (IC-E). This figure also suggests that batteries are superior

to capacitors for applications where the time of discharge is greater than the order of seconds. The figure shows that, while Li-ion batteries can easily satisfy HEV & PHEV requirements, the specific energy is much smaller than needed for EVs. Current commercialized HEVs use Ni-MH battery packs due to safety and other reasons and a huge amount of effort is currently being made to replace them with Li-ion battery packs. This is because Li-ion batteries have higher specific capacities than nickel-metal hydride-metal batteries. This thesis explains the structural properties of several Li-ion battery conditions. [8]

Many of the available battery systems do not satisfy the DOE goals[2-4] for battery life cycle and price. For example, EVs have a targeted life cycle of 10 years, but it remains unclear how long current batteries can run because available life time estimates are based on extrapolation from accelerated-aging tests.[9] Also, the life cycle of a battery often decreases with increases in operating temperature. For example, cars driven in places with warm temperatures may show a shorter lifetime than those in colder places. Another important point, cost, is also a major challenge. This is because batteries are expendable supplies that need to be replaced regularly. If the price is too high, then regularly replacing them will be a huge cost burden to customer. Previous studies have found that, for a high-energy Li-ion battery, the main factors involved in adjusting the cost are the cathode-active material (~49%), electrolyte(~23%), anode-active material(~11%), with the rest due to manufacturing and other costs(~17%).[10] This tells us that the price of the raw materials used to make the cathode-active and anode-active materials are the key to the total battery pricing. Materials containing Co and Ni change the final battery price, illustrating the need to focus on developing better cathode active material. The disadvantage of using Co and Ni is resource limitation and high cost.

1.3 Li-Ion Battery Principle

A battery is a system for electrochemical energy conversion and storage where energy is generated by conversion of chemical energy through redox reactions at both the anode and the cathode. The Li-ion battery is one candidate among many different kinds of batteries but is outstanding due to the fact that Li-ion battery shows high energy density and also is the most electropositive metal compared to standard hydrogen electrode.[11] Since Li can be more easily handled (though with care) than other alkali metals and significantly, the lightest and the most electropositive among the alkali metal family. The Li-ion battery has significant advantages over the other batteries. A battery system has three major parts: anode, cathode and electrolyte. During the charge/discharge cycle in a Li-ion battery, Li ions move across the electrolyte between the anode and the cathode. Most Li-ion batteries use liquid electrolytes containing a lithium salt, such as $LiPF_6$, $LiClO_4$, $LiBC_4O_8$, $LiBF_4$, dissolved in a mixture of ethylene carbonate (EC), dimethyl carbonate (DMC), diethyl carbonate (DEC) and ethylmethyl carbonate (EMC), giving the electrolyte high electronic and ionic conductivity. A separator is needed to avoid a short circuit between the anode and the cathode. Plastic film and glass wool can be used as a separator. The basic energy storage in the battery cell can be expressed by the reactions shown in **Figure 1.2** and a schematic diagram of the chemical reaction of the lithium ion battery is displayed in **Figure 1.3**.

1.4 Lithium Ion Battery Motivation and Challenge

The commercial lithium ion battery was first developed by the Sony Co (Japan) more than 20 years ago, and its layered compounds consist of lithium cobalt oxide ($LiCoO_2$) as the cathode (positive electrode), graphite (C) as the anode (negative electrode), and an electrolyte with a non-aqueous Li-ion conducting medium. Numerous variants of the basic lithium-ion cell chemistry have been developed.[9] Lithium cobalt oxide and lithium manganese oxide were the first to be produced in commercial quantities but lithium iron phosphate is taking over for high power applications because of its improved safety performance. Lithium cobalt oxide is well known for its mature, proven, and industry-standard battery technology characteristics that provide long life cycle and very high energy density. However, the use of Co is unfortunately associated with environmental and toxic hazards.[12-14] To reduce cobalt use, doped materials such as $LiCo_{1/3}Ni_{1/3}Mn_{1/3}O_2$[15,16] and $LiNi_{1-y-z}Co_yAl_zO_2$[17,18] have been used for advanced lithium-ion batteries. Compared to $LiCoO_2$, these offer lower cost, higher energy and power, as well as highly improved safety. However, these still require the use of cobalt.

Lithium manganese oxides can form in mainly two types of structures, as shown in **Figure 1.4.** In the layered $LiMnO_2$[19,20] transition metals can migrate irreversibly during delithiation, resulting in capacity loss. Upon electrochemical delithiation of the first two materials, disproportion of Mn^{3+} into Mn^{2+} and Mn^{4+} ions occurs and Mn^{2+} ions subsequently migrate into vacant sites in lithium layers via low-energy pathways, boosting structural rearrangement to spinel structure.[21] In contrast, the spinel structure of $LiMn_2O_4$ is connected by MnO_6 octahedra, and thus is more stable due to good lithium ion mobility while cycling.[21,22] Lithium manganese oxide provides a higher cell voltage than Co-based chemistries, with voltages as high as 3.8 to 4.1 V, but the energy density is about 20% less than for Co. It also provides additional benefits including lower cost and higher temperature performance.[23-26]

Lithium manganese oxide cells are also widely available but they are not yet as common as lithium cobalt oxide cells. Also, Mn, unlike Co, is a safer and more environment-friendly material.[27-29]

In addition to simple lithium metal oxides, the lithium metal polyanion framework has been also popular. Among the polyanion frameworks, the most representative material is lithium iron phosphate.[30-33] Lithium iron phosphate provides great thermal and chemical stability, and thus offers better safety characteristics than other cathode materials.[34-36] Phosphate cells are incombustible even if mishandled during charge or discharge, and they can withstand high temperatures without decomposing. Phosphate chemistry also offers a longer cycle life.[8,37-39] Finally, the phosphate framework is quite stable and provides structural stability over a long period and thus is beneficial for extensive cycling and safety issues. Another characteristic of the phosphate framework is that various types of atomic arrangements and crystal structures can be adopted without any disruption to the fundamental local structure, allowing for the formation of different types of materials based on cation/anion substitution. However, there are some drawbacks to the lithium metal polyanion framework including poor conductivity and slow lithium ion diffusion.[40] In order to solve some of the disadvantages, the phosphate framework has been modified by using different transition metals in place of Fe. Recent developments have produced a range of new environment-friendly cathode active materials such as lithium vanadium phosphate.[41-44]

Graphite is the most common commercial anode material for lithium ion batteries, due to its flat and low working potential, reasonable cost, and long cycle life. However, when the maximum Li^+ goes into the anode, graphite has a stoichiometry of LiC_6. This provides a

maximum specific capacity of 372 mAh/g.[45] The limited Li storage capacity (Li ion storage sites within a sp^2 hexagonal carbon structure[46]) and high cost of production of artificial graphite produced at very high temperatures are recognized as their main disadvantages.[46-50] In addition, the Li-ion transport rates within graphite are slower than 10^{-6} cm^2 s^{-1} leading to a low power density of the battery.[50] Therefore, in order to enhance the power density, much research has been done to find better anodes. In addition to modifications to graphite, many studies have examined different materials which can be alternatives to graphite. One of the representative materials is lithium titanate $Li_4Ti_5O_{12}$.[51-53] $Li_4Ti_5O_{12}$ has recently gained an increasing amount of recognition. $Li_4Ti_5O_{12}$ was studied in superconductor research in the 1980's, and at that time was found to intercalate lithium in a reversible process.[54] In the titanate system, Li ions occupy both tetrahedral (8a sites) and octahedral (16d sites) oxygen coordination. This allows up to 3 mol of Li per formula unit of $Li_4Ti_5O_{12}$, giving a theoretical capacity of 175 $mAhg^{-1}$ with $Li_7Ti_5O_{12}$. Later studies found that $Li_4Ti_5O_{12}$ is a zero-strain material, which in theory could allow for very high charge/discharge currents.[55,56] If no volume change takes place, the charge/discharge process is not limited by movement within the material, and thus nothing should block the ionic diffusion paths, which in turn could mean that high capacity could be achieved with high currents.[57-61] $Li_4Ti_5O_{12}$ displays excellent cycling stability and power delivery, making it an ideal component in a hybrid electric vehicle battery.

To be effective commercially, a Li-ion battery should satisfy several points: [62]

1) **Cost:** The cost is determined by the materials used and the manufacturing and assembling process. Although Co is often used for the cathode, it is expensive and cheaper materials such as Fe, Ni and Mn are preferred.

2) **Chemical and Mechanical Stability:** The electrodes must retain: a) their mechanical properties and chemical composition; b) structure and surface over time; and c) temperature in an operational environment. Mechanical and chemical stability can also be affected by reactions of the electrolyte, by phase changes, and by corrosion. Finally, chemical change may lead to poor conductivity, thus compromising the battery.
3) **Safety:** All consumer and commercial batteries must be safe in a normal operating environment and, ideally under conditions of mild abuse.
4) **Cycle life:** For commercial applications, the battery system needs to supply at least 4000 deep discharge cycles. This requires a very robust system and reversible electrode reactions. There should be minimal side reactions or structural transformation during the charge/discharge process.

X-ray Absorption Spectroscopy (XAS) is a structural method used to characterize a variety of modern battery anode and cathode materials. In this thesis, I have used the XAS to characterize the electronic structure of Li-ion-intercalated cathode/anode materials to elucidate the reaction mechanism of the electrochemical process in the actual cycling system. The goal of this work is to understand the chemical changes happening in a real battery under operating conditions, which ultimately may give an idea of battery material modifications that may give an improved battery. Modifications could be made by substituting different transition metals that can solve the problems of current battery cost issues (instead of using "Co" in the oxide-based system) and safety (do not perform well below about 0℃) issues (instead of using "Fe" in the phosphate system). If XAS can provide an idea whether newly designed or modified materials

face any structural distortion or degradation during charge/discharge cycling, this information will be useful and beneficial.

1.5 X-ray Absorption Spectroscopy (XAS)

X-rays have sufficient energy to eject one or more core electrons from an atom. Each core electron has a well-defined binding energy, and when the energy of the incident X-ray is scanned across one of these energies, there is an abrupt increase in the absorption coefficient. This is the so-called "absorption edge" of the element, as shown in **Figure 1.5**. XAS refers to the details of how x-rays are absorbed by an atom at energies near and above the core-level binding energies of that atom. It has been used to investigate the local structural environment of metal ions for over 40 years. The technique can be divided into X-ray absorption near edge structure (XANES) and extended X-ray absorption fine structure (EXAFS), as shown in **Figure 1.5** (b).[63-67] All atoms have core level electrons, and thus XAS spectra can be measured for essentially every element on the periodic table. Importantly, crystallinity is not required for XAS measurements, making it one of the few structural probes available for non-crystalline and highly disordered materials. One of the advantages is that XAS is element specific, permitting the investigation of the chemical environment of all of the constituent elements in a single composite material.[68] Because of its versatility, XAS has applications in an enormous variety of electrochemical systems, including battery electrode materials and additives in electrodes.

The core electron can be excited into unoccupied bound or continuum states, as shown in **Figure 1.5** (a). The key fact is that the photoelectrons act as very sensitive probes that can feel

the charge distribution and the arrangement of the neighboring atoms around the absorbing core atom. The bound atom excitation process can be understood by means of multiple scattering. The low energy portion of the spectra is the XANES region and the near-edge structure ends approximately where the electron wavelength equals the distance from the absorbing atom to its nearest neighbors,[69] about 40–50 eV above the edge. In the XANES region, the kinetic energy of the electron is small and the scattering from neighboring atoms is stronger than at higher energies. [69]

XANES strongly depends on the local geometry of the material (coordination number and ligand symmetry). The pre-edge region feature is caused by electronic transitions to empty bound states. The pre-edge region in XANES provides information about the absorber's local geometry, electronic state around the absorber, number of neighbors, ligand symmetry, and valence state.[70] This unique information is generally impossible to obtain using crystallography.[71,72] The edge energy can be defined as the energy at some specific absorbance (i.e. half maximum) or can be taken as the energy of the first inflection point. The edge energy typically increases by several eV per oxidation unit. Most of the changes happening in the XANES spectra depend on the ligand identity and geometry and thus can be used to provide qualitative information about the ligation of an unknown site and/or quantitative information based on comparison with model compounds molecular orbital symmetry.[71,73]

The pre-edge transition immediately prior to the main absorption feature for the first row transition metals is due to a 1s → 3d transition. The intensity of the pre-edge region (which allows 1s → 3d transition) can be used to determine the geometry of the material complexes. It is well known that an intense pre-edge peak is observed in K-edge XANES of a compound

possessing tetrahedral (T_d) centers, whereas low intensity peaks show up for compounds with octahedral (O_h) symmetry(see **Figure 1.6**).[74] Also, the pre-edge peak intensity decreases with an increase in the coordination number of a central atom. This idea has been utilized as a significant tool for determining the coordination of the various unknown samples. 1s → 3d transitions happen in the centrosymmetric complexes with dipole-forbidden (ΔL = 2), quadrupole allowed transitions. In a nano-centrosymmetric environment hybridization mixes p and d states, and the dipole-allowed (s → p) transition gives an increase in intensity. In octahedral geometry, 3d-4p mixing is forbidden by symmetry, give a low intensity to the 1s → 3d peak. [71,75] The intensity is weak but not zero because of distortion, either static or vibronic, and also because of weak quadrupole coupling[76,77]

There has been previous work use XAS to interpret processes at the cathode of lithium ion batteries. For example, based on the XANES spectrum in **Figure 1.7**, it was concluded that charge compensation by lithiation/delithiation can be achieved by the oxidation/reduction between Ti^{4+} and Ti^{3+} by measuring the main edge energy shifts either to the right (oxidation) or left(reduction) during charge/discharge cycling.[56] In **Figure 1.7**, the energy change in four points A (1s → 3d peak), B (the first inflection point), C (the second inflection point) and D (principal maximum) can be used as a tool to measure energy difference in order to calculate oxidation change happening while cycling. All four points show a decrease in energy on discharge and an increase in energy during charge. The weak peak at ~4972 eV (labeled **A** in **Figure 1.7**) is identified as a 1s → 3d transition, and can be used to characterize the electronic structure of the Ti. Only a single peak is observed in the 1s → 3d region which means that neither the shape (i.e., full-width at half-maximum intensity) nor the intensity of the 1s → 3d transition changes during cycling.[56]

Extended X-ray Absorption Fine Structure (EXAFS) refers to the oscillations in the absorption coefficient on the high-energy side of X-ray absorption edges, ranging from 30 eV to about 1000 eV above the edge. The fluctuations of the absorption coefficient are caused by the atomic arrangement surrounding the absorbing atom[77-79] which gives a unique signature to the specific material. It is also highly dependent on the detailed atomic structure and electronic properties of the specific material. As shown in **Figure 1.8**, when x-ray energy is absorbed by a central atom (blue), a photoelectron wave is propagated outward. This outgoing wave is backscattered off neighboring atoms (red and green) and interferes with itself at the origin. Because of the ratio of the absorber-neighbor distance to the photoelectron wavelength, it is interfering constructively with respect to the first shell (red) and destructively with the second shell (green). These quantum interference effects cause an energy-dependent variation in the X-ray absorption probability, which is proportional to the X-ray absorption coefficient, a measurable quantity. When properly decoded, these modulations provide information about the structure, atomic number, structural disorder, and thermal motions of neighboring atoms.[80]

EXAFS oscillation can be described by **Eq. 3.4** in Chapter III, but it is not a convenient form for visualizing the information content of an EXAFS spectrum. Fourier transformation can be used to visualize the frequencies contributing to EXAFS and is used to decompose oscillatory signals into different constituent frequencies. Transformation from k (in $Å^{-1}$) and R (in Å) gives a pseudo-radial distribution function. As a consequence of the phase shift ϕ (k) in the EXAFS equation (**Eq. 3.4** in Chapter III), the apparent distances in the Fourier transform (FT) are shifted by about −0.5 Å. The FT is useful for obtaining a qualitative understanding of a system. However, FTs are subject to several potential artifacts and cannot be used for quantitative data analysis. FT of an EXAFS spectrum is actually a complex number with both real and imaginary

components.[67,81,82] Typically, however, only the modulus of the FT is plotted. This is useful for visualizing the major contributions to the EXAFS spectrum, but should never be used for quantitative data analysis.

1.6 *In-situ* Measurement

XAS is an ideal method for *in-situ* studies of electrochemical systems because both the probe and signal are penetrating X-rays, allowing air sensitive samples to be measured through a protective aluminum window; other spectroscopies (UV-vis, soft x-ray, etc.) are often unable to penetrate both the electrode material and the window. The main characterization method in this thesis was performed using *in-situ* studies with electrochemical cells that permit X-ray Absorption Spectroscopy (XAS) on the intact, functional electrodes. In contrast to much of the published EXAFS of cathode materials, which have emphasized *ex-situ* measurements,[83-85] a unique point in this thesis is that all the measurements were performed *in-situ*. *In-situ* measurements have several advantages, the most obvious being that they avoid the possibility of changes in sample condition as a consequence of *ex-situ* handling and thus accurately correlate experimental spectroscopic and electrochemical results. These results were obtained from electrode materials under realistic operating conditions.[73] Unlike *ex-situ*, *in-situ* measurements allow one to perform a complete experiment without exposure to an external environment.[73,86] A second advantage is that there is no change in the sample during charge and discharge, as compared to *ex-situ* measurements, where a different sample must be prepared for each different state of charge.[73,86,87] This eliminates any spectral changes that could result from differences in sample preparation, and makes the measurements much more sensitive to small spectral changes.

In general, quantitative determination of bond length within EXAFS analysis allows the accuracy of ± 0.02 Å and precision of ± 0.004 Å.[67] Therefore, *in-situ* measurements are favorable in terms of offering very precise results without optimizing the precision.

1.7 General Organization

This thesis focuses on electrochemical and local structural analysis of the cathode/anode materials used in the lithium ion battery systems. Chapter II describes an anode system and Chapter III & IV & V present information about two cathode systems.

Chapter II discusses the electrochemical and local structural analysis of a mesoporous $Li_4Ti_5O_{12}$ anode made by hydrothermal synthesis. This synthetic method has been shown to improve the voltage profiles and charge/discharge dynamics of the material, since the mesoporous lithium titanate microspheres show good cycling performance and high capacity retention at a high number of cycling. The main focus of this chapter is to describe the functioning of this promising anode material at the molecular level. The work has been published as Soojeong Kim et al. "The Electrochemical and Local Structural Analysis of the Mesoporous $Li_4Ti_5O_{12}$ Anode". *Journal of Power Sources* 268 (**2014**) 294-300

Chapter III discusses the spinel $LiMn_2O_4$, a well-known material that has recently drawn considerable interest for use as a cathode material for rechargeable lithium batteries. In order to investigate the potential of this material, X-ray Absorption Spectroscopy was performed to determine the electronic structure of $LiMn_2O_4$ before and after annealing. Since annealing is

known to improve the material performance, the structural and oxidation state consequences of annealing are determined.

Chapter IV reports on the electrochemical and structural analysis of $Li_3V_2(PO_4)_3$ based on a Principal Component Analysis (PCA) method at different cycling rates. Monoclinic $Li_3V_2(PO_4)_3$ displays high capacity and has emerged as one of the most promising phosphate candidates for cathodes. In this chapter *in-situ* x-ray absorption method shows, for the first time, that kinetic effects play an important role in the behavior of $Li_3V_2(PO_4)_3$ and also shows the structural consequences exceeding the standard cut-off voltage of 4.5 V.

Chapter V uses the same technique explained in Chapter IV but with a different material. $Li_3V_{(2-2x/3)}Mg_x(PO_4)_3/C$ (x=0.15, 0.30, and 0.45) was chosen because previous studies have shown that Mg doping improves the electronic conductivity, specific capacity, cycle performance, and rate capability. This chapter discusses the structural consequences of Mg doping of $Li_3V_2(PO_4)_3$ and based on these observation it is possible to we are able to provide an atomic scale explanation for the observation that 30% Mg doping gives the optimum electrode behavior.

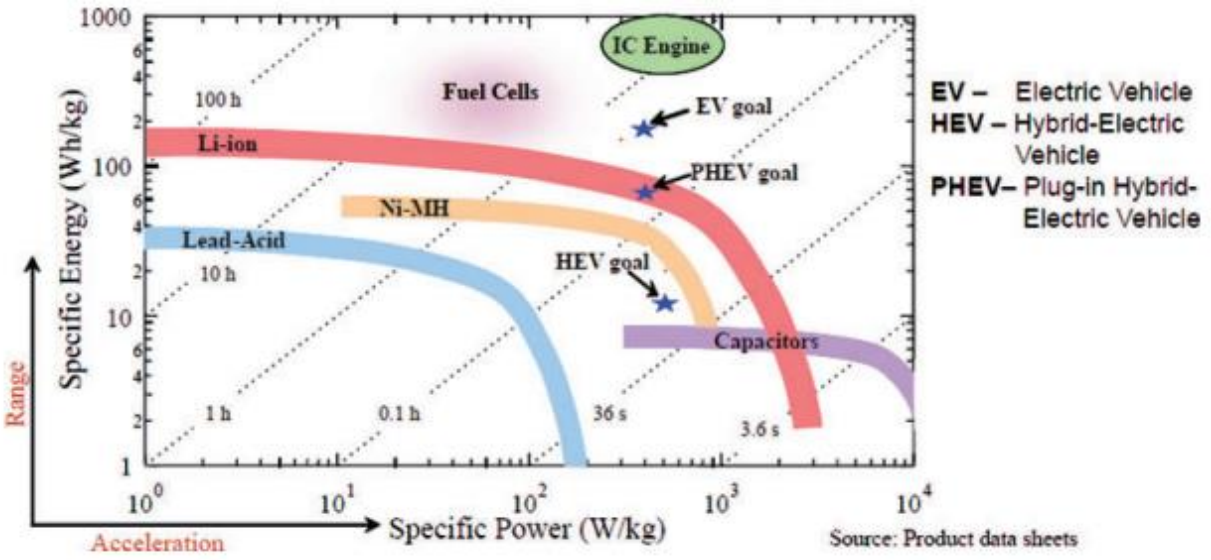

Figure 1.1 Ragone plot comparing the system-level performance of three battery chemistries, capacitors, fuel cells, and the internal combustion (IC) engine. Information is drawn from product data sheets. The Li-ion category is meant to reflect the performance of the Li_xC_6/Li_yCoO_2 chemistry. Ni-MH: nickel-metal hydride. Ragone plot is from on line article from LBNL, reference [88]

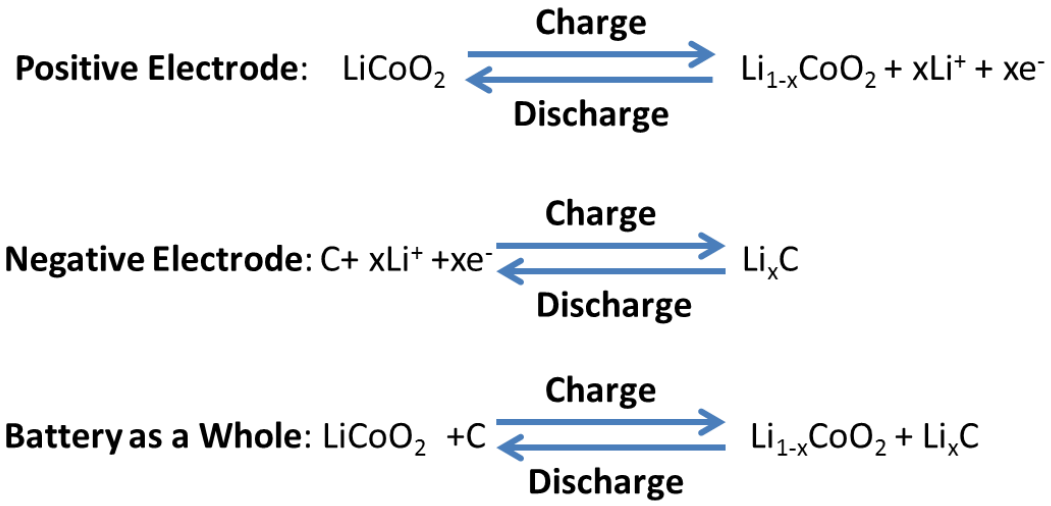

Figure 1.2 Reactions in a Li-ion battery

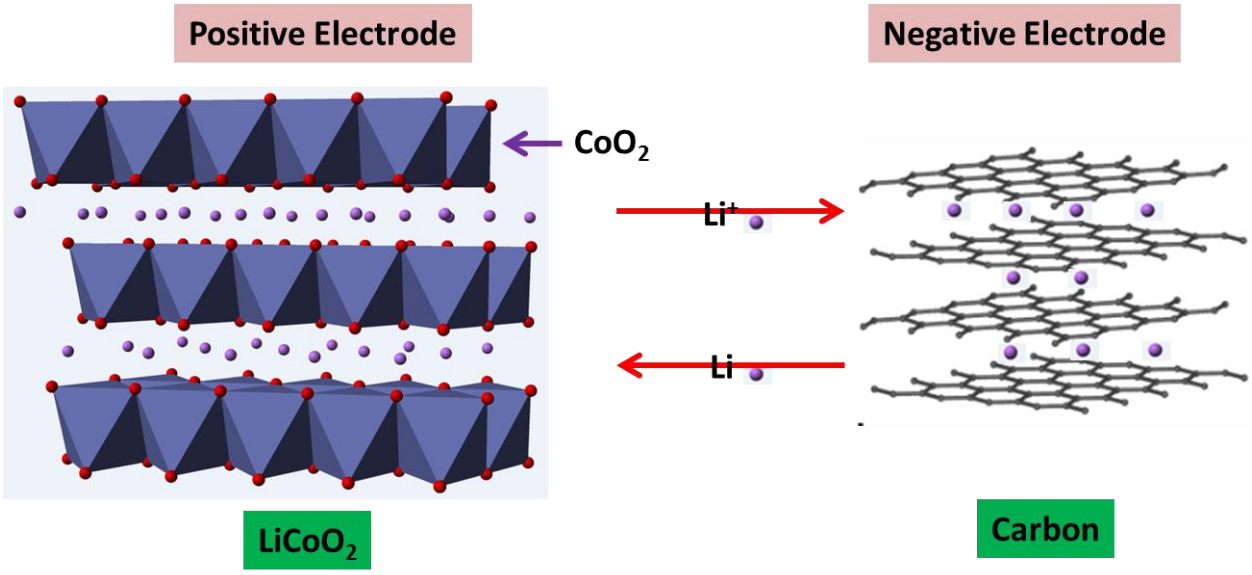

Figure 1.3 Schematic diagram of the chemical reaction of the lithium ion battery (modified from, http://en.wikipedia.org/wiki/Allotropes_of_carbon#mediaviewer/File:Eight_Allotropes_of_Carbon.png, and http://en.wikipedia.org/wiki/Lithium_cobalt_oxide#mediaviewer/File:Lithium-cobalt-oxide-3D-polyhedra.png[89])

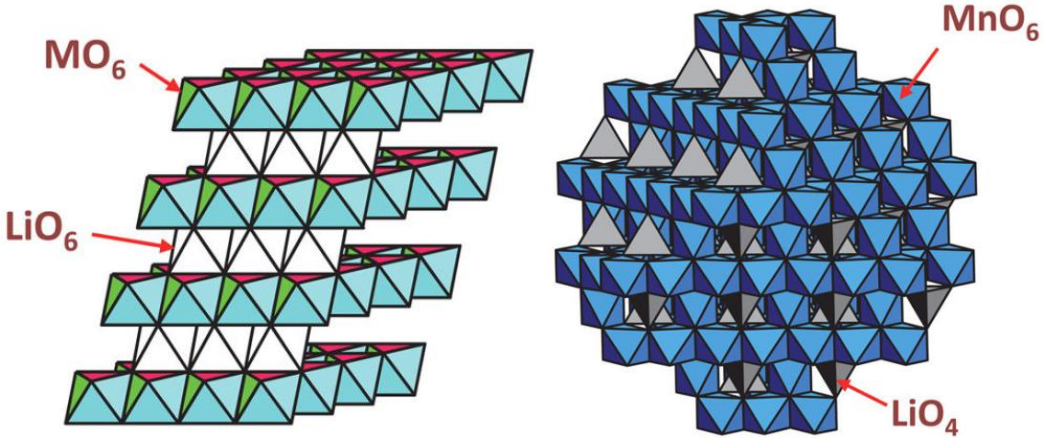

Figure 1.4 Lithium manganese oxides in two main structures "Layered Oxide $LiMnO_2$" (left) and "Spinel oxide $LiMn_2O_4$" (Right). Adapted from Figure 1 in reference.[90]

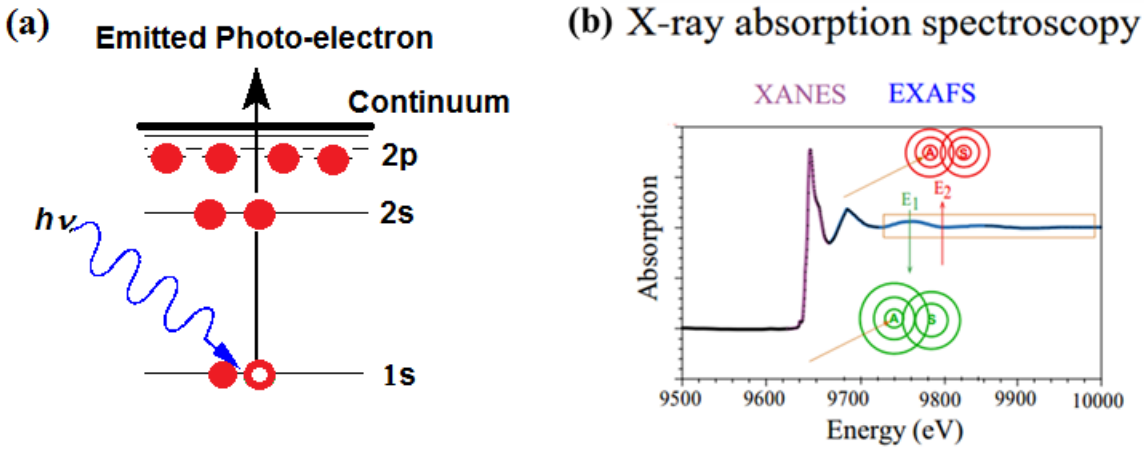

Figure 1.5 (a) Electron excitation process scheme and (b) XAS spectra including both X-ray Absorption Near Edge Structure (XANES) and Extended X-ray Absorption Fine Structure (EXAFS), [(b) from jphgroup XAS_course lecture: www.umich.edu/~jphgroup/XAS_Course/Harbin/Lecture1.pdf]

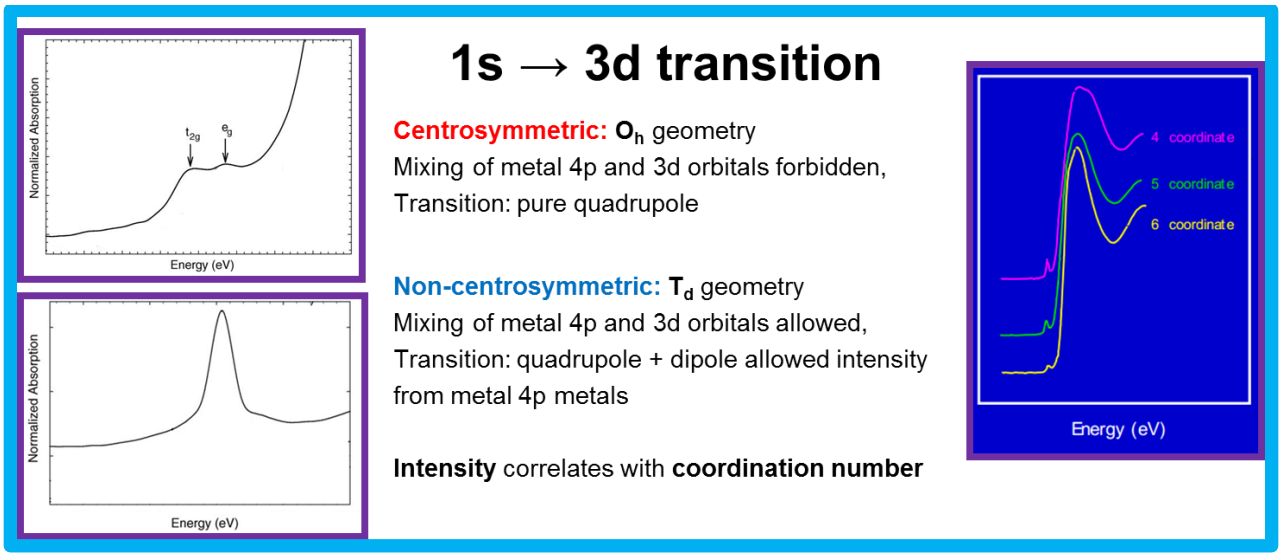

Figure 1.6 Scheme 1: sketch of the 1s → 3d transition in the pre-edge region

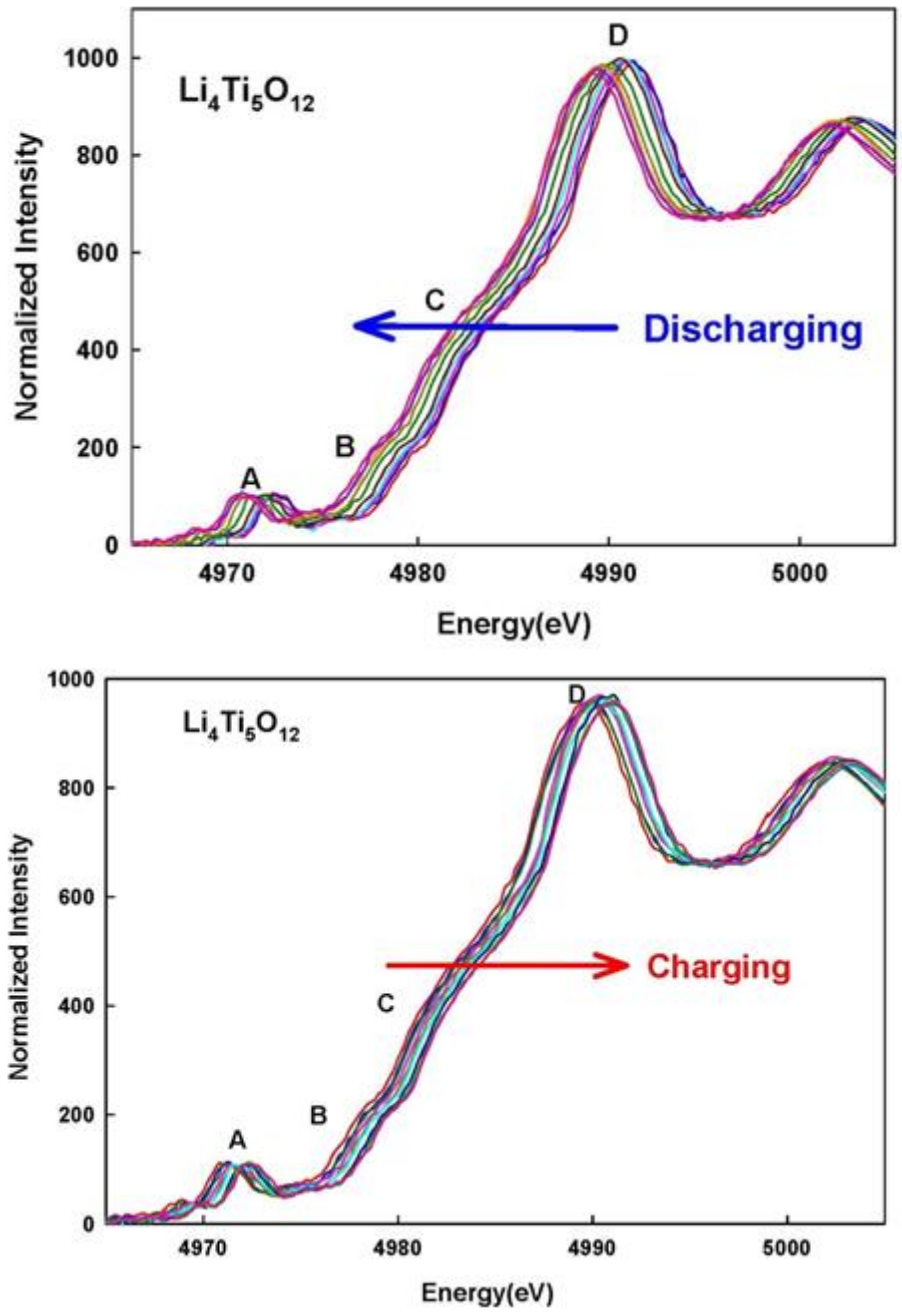

Figure 1.7 *In-situ* Ti-K edge XANES during discharge and charge. The galvanostatic cycling of the *in-situ* studies was performed at a current density of 175 mA g^{-1}, between 2.5 V and 1.0 V[56]

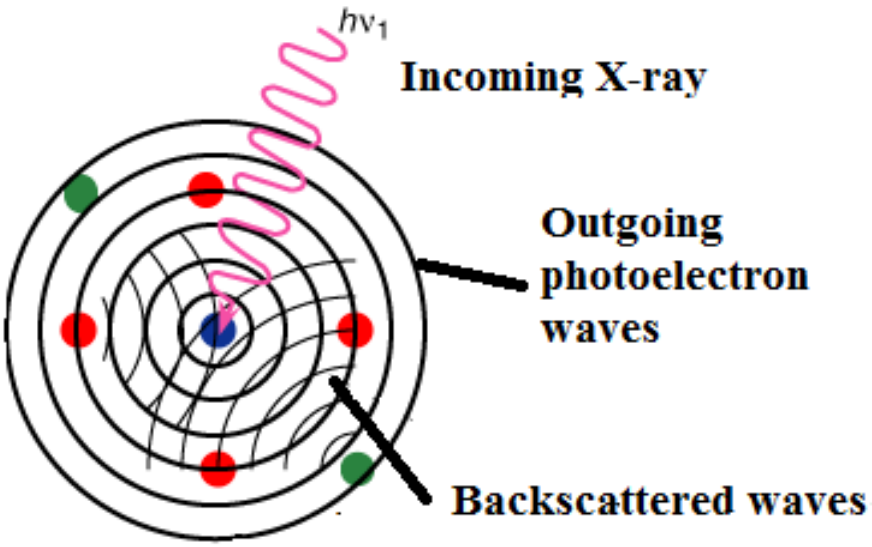

Figure 1.8 Schematics of interference of outgoing and backscattered photoelectron wave in the EXAFS oscillations. Figure was used with permission http://www.lanl.gov/orgs/nmt/nmtdo/AQarchive/04summer/XAFS.html

1.8 REFERENCES

(1) Nelson, R. F. *J Power Sources* 2000, *91*, 2.
(2) http://www.uscar.org/commands/files_download.php?files_id=262002.
(3) http://www.uscar.org/commands/files_download.php?files_id=272002.
(4) http://www.uscar.org/commands/files_download.php?files_id=118 2007.
(5) Cairns, E. J.; Albertus, P. *Annu Rev Chem Biomol* 2010, *1*, 299.
(6) Maier, J. *Angew Chem Int Edit* 2013, *52*, 4998.
(7) Palacin, M. R. *Chem Soc Rev* 2009, *38*, 2565.
(8) Zaghib, K.; Dontigny, M.; Guerfi, A.; Charest, P.; Rodrigues, I.; Mauger, A.; Julien, C. M. *J Power Sources* 2011, *196*, 3949.
(9) Reddy, M. V.; Rao, G. V. S.; Chowdari, B. V. R. *Chem Rev* 2013, *113*, 5364.
(10) Gaines L, C. R. *Costs of lithium-ion batteries for vehicles.* , Argonne Natl. Lab., Argonne, Ill., 2000.
(11) Tarascon, J. M.; Armand, M. *Nature* 2001, *414*, 359.
(12) Ohzuku, T.; Ueda, A.; Nagayama, M.; Iwakoshi, Y.; Komori, H. *Electrochim Acta* 1993, *38*, 1159.
(13) MacNeil, D. D.; Lu, Z. H.; Chen, Z. H.; Dahn, J. R. *J Power Sources* 2002, *108*, 8.
(14) Tan, K. S.; Reddy, M. V.; Rao, G. V. S.; Chowdari, B. *J Power Sources* 2005, *147*, 241.
(15) Lin, F.; Markus, I. M.; Nordlund, D.; Weng, T. C.; Asta, M. D.; Xin, H. L. L.; Doeff, M. M. *Nat Commun* 2014, *5*.
(16) Ohzuku, T.; Makimura, Y. *Chem Lett* 2001, 642.
(17) Guilmard, M.; Croguennec, L.; Denux, D.; Delmas, C. *Chem Mater* 2003, *15*, 4476.
(18) Jo, M.; Noh, M.; Oh, P.; Kim, Y.; Cho, J. *Adv Energy Mater* 2014, *4*.
(19) Goodenough, J. B.; Thackeray, M. M.; David, W. I. F.; Bruce, P. G. *Rev Chim Miner* 1984, *21*, 435.
(20) Thackeray, M. M.; Johnson, P. J.; Depicciotto, L. A.; Bruce, P. G.; Goodenough, J. B. *Mater Res Bull* 1984, *19*, 179.
(21) Thackeray, M. M.; David, W. I. F.; Bruce, P. G.; Goodenough, J. B. *Mater Res Bull* 1983, *18*, 461.
(22) David, W. I. F.; Goodenough, J. B.; Thackeray, M. M.; Thomas, M. G. S. R. *Rev Chim Miner* 1983, *20*, 636.

(23) Reddy, M. V.; Raju, M. J. S.; Sharma, N.; Quan, P. Y.; Nowshad, S. H.; Emmanuel, H. E. C.; Peterson, V. K.; Chowdari, B. V. R. *J Electrochem Soc* 2011, *158*, A1231.
(24) Sharma, N.; Reddy, M. V.; Du, G. D.; Adams, S.; Chowdari, B. V. R.; Guo, Z. P.; Peterson, V. K. *J Phys Chem C* 2011, *115*, 21473.
(25) Xia, Y. Y.; Yoshio, M. *J Electrochem Soc* 1997, *144*, 4186.
(26) Xia, Y. Y.; Yoshio, M. *J Power Sources* 1997, *66*, 129.
(27) Ferg, E.; Gummow, R. J.; Dekock, A.; Thackeray, M. M. *J Electrochem Soc* 1994, *141*, L147.
(28) Gummow, R. J.; Dekock, A.; Thackeray, M. M. *Solid State Ionics* 1994, *69*, 59.
(29) Gummow, R. J.; Thackeray, M. M. *J Electrochem Soc* 1994, *141*, 1178.
(30) Barker, J.; Saidi, M. Y.; Swoyer, J. L. *Electrochem Solid St* 2003, *6*, A53.
(31) Wang, D. Y.; Li, H.; Shi, S. Q.; Huang, X. J.; Chen, L. Q. *Electrochim Acta* 2005, *50*, 2955.
(32) Uchida, S.; Yamagata, M.; Ishikawa, M. *J Power Sources* 2013, *243*, 481.
(33) Wang, L.; Sun, W. T.; Tang, X. Y.; Huang, X. K.; He, X. M.; Li, J. J.; Zhang, Q. W.; Gao, J.; Tian, G. Y.; Fan, S. S. *J Power Sources* 2013, *244*, 94.
(34) Doeff, M. M.; Hu, Y. Q.; McLarnon, F.; Kostecki, R. *Electrochem Solid St* 2003, *6*, A207.
(35) Martin, J. F.; Yamada, A.; Kobayashi, G.; Nishimura, S. I.; Kanno, R.; Guyomard, D.; Dupre, N. *Electrochem Solid St* 2008, *11*, A12.
(36) Delmas, C.; Maccario, M.; Croguennec, L.; Le Cras, F.; Weill, F. *Nat Mater* 2008, *7*, 665.
(37) Padhi, A. K.; Nanjundaswamy, K. S.; Goodenough, J. B. *J Electrochem Soc* 1997, *144*, 1188.
(38) Huang, H.; Yin, S. C.; Nazar, L. F. *Electrochem Solid St* 2001, *4*, A170.
(39) Yamada, A.; Chung, S. C.; Hinokuma, K. *J Electrochem Soc* 2001, *148*, A224.
(40) Liu, J.; Banis, M. N.; Sun, Q.; Lushington, A.; Li, R. Y.; Sham, T. K.; Sun, X. L. *Adv Mater* 2014, *26*, 6472.
(41) Saidi, M. Y.; Barker, J.; Huang, H.; Swoyer, J. L.; Adamson, G. *Electrochem Solid St* 2002, *5*, A149.
(42) Yin, S. C.; Grondey, H.; Strobel, P.; Anne, M.; Nazar, L. F. *J Am Chem Soc* 2003, *125*, 10402.

(43) Yin, S. C.; Grondey, H.; Strobel, P.; Huang, H.; Nazar, L. F. *J Am Chem Soc* **2003**, *125*, 326.
(44) Huang, H.; Yin, S. C.; Kerr, T.; Taylor, N.; Nazar, L. F. *Adv Mater* **2002**, *14*, 1525.
(45) Skowronski, J. M.; Knofczynski, K. *J New Mat Electr Sys* **2006**, *9*, 359.
(46) Zheng, T.; Reimers, J. N.; Dahn, J. R. *Phys Rev B* **1995**, *51*, 734.
(47) Dahn, J. R.; Zheng, T.; Liu, Y. H.; Xue, J. S. *Science* **1995**, *270*, 590.
(48) Sato, K.; Noguchi, M.; Demachi, A.; Oki, N.; Endo, M. *Science* **1994**, *264*, 556.
(49) Persson, K.; Hinuma, Y.; Meng, Y. S.; Van der Ven, A.; Ceder, G. *Phys Rev B* **2010**, *82*.
(50) Persson, K.; Sethuraman, V. A.; Hardwick, L. J.; Hinuma, Y.; Meng, Y. S.; van der Ven, A.; Srinivasan, V.; Kostecki, R.; Ceder, G. *J Phys Chem Lett* **2010**, *1*, 1176.
(51) Kang, S. H.; Pol, V. G.; Belharouak, I.; Thackeray, M. M. *J Electrochem Soc* **2010**, *157*, A267.
(52) Li, S. R.; Chen, C. H.; Xia, X.; Dahn, J. R. *J Electrochem Soc* **2013**, *160*, A1524.
(53) Yang, Z. G.; Choi, D.; Kerisit, S.; Rosso, K. M.; Wang, D. H.; Zhang, J.; Graff, G.; Liu, J. *J Power Sources* **2009**, *192*, 588.
(54) Ronci, F.; Reale, P.; Scrosati, B.; Panero, S.; Albertini, V. R.; Perfetti, P.; di Michiel, M.; Merino, J. M. *J Phys Chem B* **2002**, *106*, 3082.
(55) Colbow, K. M.; Dahn, J. R.; Haering, R. R. *J Power Sources* **1989**, *26*, 397.
(56) Kim, S.; Fang, S. H.; Zhang, Z. X.; Chen, J. Z.; Yang, L.; Penner-Hahn, J. E.; Deb, A. *J Power Sources* **2014**, *268*, 294.
(57) Wu, K.; Yang, J.; Zhang, Y.; Wang, C. Y.; Wang, D. Y. *J Appl Electrochem* **2012**, *42*, 989.
(58) Scharner, S.; Weppner, W.; Schmid-Beurmann, P. *J Electrochem Soc* **1999**, *146*, 857.
(59) Peramunage, D.; Abraham, K. M. *J Electrochem Soc* **1998**, *145*, 2609.
(60) Albertini, V. R.; Perfetti, P.; Ronci, F.; Reale, P.; Scrosati, B. *Appl Phys Lett* **2001**, *79*, 27.
(61) Du Pasquier, A.; Huang, C. C.; Spitler,T.*JPowerSources* **2009**,*186*,508.
(62) Winter, M.; Brodd, R. J. *Chem Rev* **2004**, *104*, 4245.
(63) Crozier, E. D. *Nucl Instrum Meth B* **1997**, *133*, 134.
(64) Lee, P. A.; Citrin, P. H.; Eisenberger, P.; Kincaid, B. M. *Rev Mod Phys* **1981**, *53*, 769.
(65) Scott, R. A. *Method Enzymol* **1985**, *117*, 414.
(66) Penner-Hahn, J. E. *Coordin Chem Rev* **1999**, *192*, 1101.

(67) Penner-Hahn, J. E. *Coordin Chem Rev* 2005, *249*, 161.
(68) Yi, Y. B.; Wang, C. W.; Sastry, A. M. *J Eng Mater-T Asme* 2006, *128*,73.
(69) Penner-Hahn,J.E.;X-rayAbsorption spectroscopy http://www.umich.edu/~jphgroup/XAS_Course/Harbin/CCC2_XAS.pdf.
(70) Uribe-Laverde, M. A.; Das, S.; Sen, K.; Marozau, I.; Perret, E.; Alberca, A.; Heidler, J.; Piamonteze, C.; Merz, M.; Nagel, P.; Schuppler, S.; Munzar, D.; Bernhard, C. *Phys Rev B* 2014, *90*.
(71) Deb, A.; Bergmann, U.; Cairns, E. J.; Cramer, S. P. *J Synchrotron Radiat* 2004, *11*, 497.
(72) Young, N. A. *Coordin Chem Rev* 2014, *277*, 224.
(73) Deb, A.; Bergmann, U.; Cramer, S. P.; Cairns, E.J.*J ApplPhys* 2005,*97*.
(74) Yamamoto, T. *X-Ray Spectrom* 2008, *37*, 572.
(75) Kawai, J.; Yamamoto, T. *X-Ray Spectrom* 2008, *37*, 203.
(76) Peterson, M. L.; Brown, G. E.; Parks, G. A.; Stein, C. L. *Geochim Cosmochim Ac* 1997, *61*, 3399.
(77) Stern, E. A. *Phys Rev B* 1974, *10*, 3027.
(78) Lytle, F. W.; Sayers, D. E.; Stern, E. A. *Phys Rev B* 1975, *11*, 4825.
(79) Stern, E. A.; Sayers, D. E.; Lytle, F. W. *Phys Rev B* 1975, *11*, 4836.
(80) Bunker, G. *Introduction to XAFS: A Practical Guide to X-ray Absorption Fine Structure Spectroscopy*; ,Cambridge University Press, 2010 Vol. 1 edition .
(81) Gaur, A.; Shrivastava, B. D.; Srivastava, K.; Prasad, J.; Raghuwanshi, V. S. *J Chem Phys* 2013, *139*.
(82) Gaur, A.; Shrivastava, B. D.; Srivastava, K.; Prasad, J. *J Appl Phys* 2013, *113*.
(83) Ohzuku, T.; Ueda, A. *Solid State Ionics* 1994, *69*, 201.
(84) Ueda, A.; Ohzuku, T. *J Electrochem Soc* 1994, *141*, 2010.
(85) McBreen, J. *J Solid State Electr* 2009, *13*, 1051.
(86) Johnson, C. S.; Kropf, A. J. *Electrochim Acta* 2002, *47*, 3187.
(87) Balasubramanian, M.; Sun, X.; Yang, X. Q.; McBreen, J. *J Power Sources* 2001, *92*, 1.
(88) Srinivasan, V. Batteries for Vehicular Applications [Online Early Access]. http://bestar.lbl.gov/venkat/files/batteries-for-vehicles.pdf.
(89) http://en.wikipedia.org/wiki/Lithium_cobalt_oxide#mediaviewer/File:Lithium-cobalt-oxide-3D-polyhedra.png, http://en.wikipedia.org/wiki/Allotropes_of_carbon#mediaviewer/File:Eight_Allotropes_of_Carbon.png
(90) Masquelier, C.; Croguennec, L. *Chem Rev* 2013, *113*, 6552.

CHAPTER II

THE ELECTROCHEMICAL AND LOCAL STRUCTURAL ANALYSIS OF THE MESOPOROUS $Li_4Ti_5O_{12}$ ANODE

This work has been published as:

Soojeong Kim, Shaohua Fang, Zhengxi Zhang, Jizhang Chen, Li Yang, James E Penner-Hahn, Aniruddha Deb. The Electrochemical and Local Structural Analysis of the Mesoporous $Li_4Ti_5O_{12}$ Anode. *Journal of Power Sources* 268 (**2014**) 294-300.

2.1. INTRODUCTION

Rechargeable Li-ion materials are widely used in hybrid electric vehicles, portable electronic devices, and advanced electrochemical energy storage devices due to their relatively high energy/power density, safety, and cycle life.[1-4] Nevertheless, there remain major impediments to their further adoption for many industrial needs. Li-ion intercalation materials lack sufficient power density and cycle life. For robust automotive applications the choice of the electrode materials is determined by cost factors as well as the ability to deliver the necessary energy (and power) without undergoing material degradation/failure. In order to overcome these limitations, efforts have been made to find new materials for both the cathode and the anode, to understand at the molecular level how these new classes of electrode materials function in

electrochemical energy storage devices, and to use this knowledge to inform the design of new materials which will lead to the improvement of the total battery system.[4,5]

One particular problem with Li-ion materials is the fact that lithiation and delithiation can cause significant volume changes which, in turn, can result in severe degradation of the electrodes, strongly limiting the lifetime of the battery. One promising candidate anode material is the mesoporous spinel (space group, Fd-3 m) $Li_4Ti_5O_{12}$, that consists of cubic close packed oxygen ions with lithium ions occupying tetrahedral (8a) and octahedral (16c, 16d) sites, and Ti, partly substituted by Li, occupying the octahedral 16d sites. An advantage of $Li_4Ti_5O_{12}$ is its "zero-strain" property, in which the lithiated and delithiated phases show almost identical lattice parameters.[6,7] In contrast to graphite, where lithium intercalation leads to exfoliation and structural stain, lithium can freely intercalate into the crystal lattice of lithium titanate and deintercalate without significant structural deformation. A second advantage of $Li_4Ti_5O_{12}$ as an anode is its safety compared to conventional graphite anodes; long cycling of graphite electrodes can result in the formation of metallic lithium dendrites which can cause a short circuit.

However, a major limitation of $Li_4Ti_5O_{12}$ as an anode material is the fact that bulk $Li_4Ti_5O_{12}$ has poor electronic conductivity which limits its capacity at high charge/discharge rates.[8,9] In an effort to overcome this limitation, various morphologies have been explored, including nanowires, nanotubes, nanorods, nanosheets and nanoparticles with the goal of maximizing the effective surface area in order to minimize conductivity limitations and thus maximize the rate.[10] We have chosen to work with $Li_4Ti_5O_{12}$ in the form of hollow microspheres because nanostructures of this sort have been shown to have shortened diffusion distances and higher surface areas, thus promising higher charge/discharge rates.[11-15] But we should also

mention here as a drawback the hollow structure leads to a decrease in volumetric energy density. In comparison with graphite, mesoporous $Li_4Ti_5O_{12}$ microspheres present several attractive features including a flatter voltage profile, higher surface area, greater stability to repeated cycling, and good lithium-ion mobility.

The hydrothermal synthesis technique[10,16] was used to produce layered hydrous lithium titanate which was transformed by thermal treatment to $Li_4Ti_5O_{12}$ microspheres assembled from nanosheets. This hollow microsphere structure is interesting due to its large surface area and thin walls, and it has been theoretically predicted[17-19] that this should lead to a decrease in the current density per unit surface area and to shorter Li-diffusion lengths in the solid phase, ultimately giving improved voltage profiles and charge/discharge dynamics. These promising points motivated us to investigate this material using *in-situ* X-ray absorption spectroscopy (XAS) in order to fully characterize its structural properties under real operating conditions.

2.2 EXPERIMENTAL

2.2.1 Electrode preparation

Samples were prepared at Shanghai Jiao Tong University, in Shanghai, China. Typically, 1 mL H_2O_2 aqueous solution (30%) and 0.618 g titanium tetraisopropoxide (TTIP) were added to 20 mL of 0.5 M LiOH aqueous solution, followed by stirring at room temperature for 0.5 h. This suspension was transferred into a 30 mL autoclave, which was maintained at 130 ˚C for 20 h and then cooled to room temperature naturally. After centrifugation the white precipitate was washed with water, dried at 80 ˚C, and was then calcined in a muffle furnace at 500 ˚C for 2 h in air. The

electrochemical properties of the samples have been investigated by galvanostatic methods. For preparing working electrodes, a mixture of $Li_4Ti_5O_{12}$, acetylene black, and polyvinylidene fluoride (PVDF) binder at a weight ratio of 80:10:10 was pasted on pure copper foil. The nano structural $Li_4Ti_5O_{12}$, presents exceptionally high rate performance and excellent cycling stability. Capacity of up to 132 mAh g^{-1} are obtained after 200 cycles at 10,000 mAg^{-1} (57 C), proving that this material is promising for high-rate applications.[10,20] Material characterization, electron microscopy, surface area determination, and electrochemical characterization were carried out by Professor Yang and his research group in SJTU, China.[20]

2.2.2 *In-situ* XAS experiments

Electrochemical XAS cell assembly was conducted in an argon-filled glove box. The separator was punched to give a disk with an outer diameter of 20 mm. The separator was placed on top of the electrode $Li_4Ti_5O_{12}$ soaked in 1 M $LiPF_6$ electrolyte, dissolved in 50 wt% ethylene carbonate (EC) and 50 wt% dimethylcarbonate (DMC) obtained as a solution from BASF. Finally, a lithium foil, counter-electrode was punched to give a disk with an outer diameter of 14 mm and an inner diameter of 8 mm and placed on top of the separator which was soaked with electrolyte. Kapton film (25.4μm thickness) was utilized as the x-ray window for this *in-situ* electrochemical reaction cell. More detailed information on the design of this reaction cell can be found in Deb et. al.[21]

For the XAS measurements, electrochemistry was performed using a Princeton Applied Research VERSASTAT potentiostat to cycle the electrochemical reaction cell. XAS measurements were performed while the electrochemical cell was cycled at a current density of

175 mA/g (1 C) between 1.0 and 2.5 V (vs. Li/Li^+) (**Figure 2.1**). Two model compounds, Ti_2O_3 (Ti^{3+}) and TiO_2 (Ti^{4+}), were measured as XANES references.

In-situ XAS measurements were performed as previously described.[22] Spectra were measured in transmission mode at the DND-CAT sector 5, at the Advanced Photon Source, using a water cooled Si(111) double crystal monochromator and a beam size of 0.3 X 4 mm^2 so that the beam could pass completely through the *in-situ* cell X-ray window. The incident photon flux was ~10^{10} photons/s. The X-ray flux before and after the electrode sample was measured using N_2 filled ion chambers. A Ti foil reference and a third ion chamber were placed behind the sample in order to provide an internal energy reference with the first inflection point of the Ti foil defined as 4966 eV. The monochromator was scanned from 200 eV below to 800 eV above the Ti K absorption edge. The data was truncated in the *k* range of 1.0 -10.5 $Å^{-1}$ due to poorer signal to noise ratio at higher values of *k*. Scans (using 5 eV steps in the pre-edge region, 0.5 eV steps in the near-edge region and 0.05 $Å^{-1}$ steps in the EXAFS region) were taken at each applied voltage. The data were integrated for 1 s per step in the pre-edge, 1.5 s per step in the near edge region and 1.5 to 25 s per step in the EXAFS region for a total scan time of about 40 min. Two scans were made at each potential and averaged.

The XANES data shown here were analyzed using the MBACK program,[23] and the EXAFS data were analyzed using the IFEFFIT[24] software package. A pre-edge background and a cubic spline EXAFS background were subtracted and the EXAFS oscillations were normalized to the appropriate Victoreen function modeling the absorption decrease above the edge[25]. An E_0 value of 4987.2 eV was used to calculate *k*. The EXAFS, $\chi(k)$, was weighted by k^3 in order to correct for the damping at high *k*. Fourier transforms were calculated as $k^3\chi(k)$ over a *k* range of

1.0 -10.5 $Å^{-1}$. The EXAFS fitting was done by IFEFFIT package using FEFF9[26] to calculate *ab initio* phase and amplitude parameters.

2.3 RESULTS and DISCUSSION

2.3.1 XANES of Charge/Discharge

The XANES spectrum for as-prepared $Li_4Ti_5O_{12}$ is compared with those for authentic Ti(III) and Ti(IV) models in **Figure 2.2**. Although the detailed structure of the XANES spectrum of $Li_4Ti_5O_{12}$ is different from that of either model, the edge energy is essentially the same as that of the TiO_2 model compound, suggesting that the oxidation state of Ti in the as−prepared material is primarily tetravalent Ti^{4+}. XANES spectra for the $Li_4Ti_5O_{12}$ anode during discharge and charge are shown in **Figures 2.3-2.4**, respectively. The edge shifts to lower energy on discharge and returns to higher energy during the charge cycle. To a first approximation, the edge shape is unchanged during electrochemical cycling, indicating that there is no significant change in the Ti environment. A variety of different points might be used to define the edge energy. These are labeled on **Figure 2.3**, **A** (1s → 3d transition), **B** (first inflection point), **C** (second inflection point) and **D** (principal maximum). All four points show a decrease in energy on discharge, although points **B** and **C** are somewhat sensitive to the details of the edge shape and thus somewhat more variable. The energy of point **A** as a function of discharge/charge capacity is shown in **Figure 2.5**, and the energies for all 4 points are tabulated in **Tables 2.1** and **2.2**. Using either **A** or **D**, the decrease in edge energy during discharge is 1.8 -2.1 eV (an average of ~2 eV), while during charge the increase in edge energy is 1.6 -1.8 eV (an average of 1.7 eV).

The data in **Figures 2.2-2.5** provide direct evidence that electrons are added to and removed from a band of primarily Ti character during cycling. For the model compounds, the change in energy on going from Ti(III) to Ti(IV) is ~3.8 eV, with the peak shifting from 4987.5 to 4991.3 eV as shown in **Figure 2.2**. This empirical correlation of ~3.8 eV per unit change in oxidation state allows us to estimate the change in average oxidation state from the change in edge energy, with an estimated uncertainty of ~10% based on the variability in edge shift, depending on which point is measured. The *in situ* XANES data thus suggest that during complete discharge the Ti is reduced to an average oxidation state of ~ $Ti^{3.5+}$, while during charging the Ti is re-oxidized back to an average oxidation state of ~ $Ti^{3.9+}$. It is noteworthy that at the start of the charge cycle (capacity of 11.7 mAh/g, shown in **Table 2.2**), the Ti has already returned ~40% of the way to the starting energy, suggesting that there was some relaxation in the discharged battery. If the XANES estimate of average oxidation state is correct, this would imply a stoichiometry of $Li_{6.5}Ti_5O_{12}$ in the fully discharged material.

The XANES region for a relatively ordered material such as $Li_4Ti_5O_{12}$ depends on the details of the atomic arrangements within 5-10 Å of the Ti. While this means that changes in XANES structure are a sensitive reporter of changes in local structure, it also effectively precludes quantitative analyses of XANES structure, since there are far more adjustable parameters than there are observable spectral features. Thus, while the lack of any significant change in XANES shape during charge or discharge provides direct evidence that there are no significant structural perturbations to the local Ti environment, it also makes it difficult to make any quantitative statements about Ti structure based on the XANES.

The weak peak at ~4972 eV (labeled **A** in **Figure 2.3**) is identified as a 1s → 3d transition, and can be used to characterize the electronic structure of the Ti. While there should, in principle, be two or more resolved 1s → 3d transitions due to crystal-field splitting, we observe only a single peak. This is not surprising given the expected 100g value of ~1.8 eV[27] and the modest resolution of the Si (111) monochromator. Measurement that have resolved the 1s → 3d transitions have typically used higher resolution monochromators. (e.g. Si (311))[28] Neither the shape (i.e., full-width at half-maximum intensity) nor the intensity of the 1s → 3d transition changes during cycling, although (as noted above) the energy of the peak shifts with the rest of the edge. From model compound studies, it is known that the 1s → 3d transition is most intense for 4-coordinate Ti and least intense for 6-coordinate Ti.[29,30] The low intensity of the 1s → 3d transition in mesoporous $Li_4Ti_5O_{12}$ is consistent with an octahedral Ti environment as expected for $Li_4Ti_5O_{12}$, and the lack of change in intensity indicates that this geometry is retained during discharge.

2.3.2 EXAFS for $Li_4Ti_5O_{12}$

The EXAFS data provides information about the local structure of the Ti ions in $Li_4Ti_5O_{12}$. The Fourier transforms (FT, **Figures 2.6-2.7**) show that in all cases the EXAFS is dominated by Ti-O nearest-neighbor scattering and Ti-Ti next-nearest-neighbor scattering. Although Li must also be present in the environment around the Ti, the Li atoms are too light to make a detectable contribution to the EXAFS. The lack of any significant change in the FTs confirms the conclusion from the XANES that the local Ti environment does not change significantly during discharge or charge cycling. The data for each state of charge were fit using

a Ti-O shell and a Ti-Ti shell with the bond length (R) and Debye-Waller factor (σ^2) for each shell treated as variable parameters and complete fit data are given in **Table 2.3**. For these fits, ΔE_0 was fixed at 0 since the E_0 value (4987.2 eV had been previously calibrated as the best E_0) in fits of model compounds. The Ti-O and Ti-Ti coordination number was fixed at 6, given that the octahedral site (16d) in $Li_4Ti_5O_{12}$ is occupied with a 1:5 ratio of Li: Ti (shown in **Eq 2.1**) and only the latter is expected to give a detectable EXAFS signal. The mechanism of Li intercalation into $Li_4Ti_5O_{12}$ is shown below in **Eq 2.1**:

$$[Li_3]^{\mathbf{8a}}[LiTi_5]^{\mathbf{16d}}[O_{12}]^{\mathbf{32e}} + 3Li^+ + 3e^- = [Li_6]^{\mathbf{16c}}[LiTi_5]^{\mathbf{16d}}[O_{12}]^{\mathbf{32e}}$$

The number of free octahedral sites limits the Li-insertion capacity $Li_4Ti_5O_{12}$ can accommodate $3Li^+$ per unit cell without unit cell parameter change. The intercalation/deintercalation processes are based on the phase transition of the spinel structure $Li_4Ti_5O_{12}$ to the NaCl super structure $Li_7Ti_5O_{12}$, permitting the reduction of $3Ti^{4+}$ ions out of 5, which corresponds to the theoretical capacity of 175 mAh/g.[31]

A close observation of the FTs during the discharge and charge (**Figures 2.6 - 2.7**) shows that the amplitude for the Ti-O peak decreases from the beginning of discharge to 49.7 mAh/g and then remains almost the same until 85.6 mAh/g and then starts to decrease again till 210.5 mAh/g. During the charge cycle, the Ti-O peak slowly increases in intensity throughout the cycle although it never recovers the amplitude of the as-prepared sample.

The accuracy of EXAFS bond length determination is typically taken as ~0.02 Å[32] and the observed Ti-O distance for $Li_4TI_5O_{12}$ is in agreement with the Ti-O distance predicted from neutron diffraction data for $Li_4TI_5O_{12}$ (1.99 Å).[33] However, the precision of EXAFS bond-length

determination is much better than its accuracy; we find empricially that the root-mean-square deviation in duplicate bond length measurements (see **Table 2.3**) is 0.0019 Å. As a consequence, even though the accuracy is only ~0.02 Å, we are nevertheless able to detect small changes in Ti-O distance as a function of charge state. As expected, the average Ti-O distance increases as the Ti is reduced and decreases again as the Ti is reoxidized, as shown in **Figure 2.8**. The total decrease on charging is smaller (~0.007 Å); however, careful examination of the data in **Figure 2.8** suggest that this is not due to irreversibility but rather to partial recovery of the Ti oxidation state prior to initiation of the charge cycle since the starting distance for the charge cycle is already reduced from the endpoint of the discharge cycle. This is similar to the behavior seen for the XANES.

The observed increase in the Ti-O distance (0.012 Å) is significantly smaller than the increase that might have been expected from the difference in the ionic radii of Ti^{4+} (0.75 Å) and Ti^{3+} (0.81 Å). The neutron diffraction data for chemically lithiated for $Li_4Ti_5O_{12}$ was interpreted as showing a movement of oxide anions towards octahedral site 16c as lithiation proceeds, presumably to better shield the added lithium cations.[20] The shift in oxide position leads to a prediction from neutron diffraction that the Ti-O distance will increase by ~0.0213 Å for $Li_{6.5}Ti_5O_{12}$ compared to $Li_4TI_5O_{12}$. Although the actual change that we see is somewhat smaller, our data thus confirm *in-situ* the prediction that was made from chemcially lithiated materials.

As noted previously, an unusual feature of $Li_4TI_5O_{12}$ is the fact that even when discharged down to 0.05 V vs. Li/Li^+ (i.e., to $Li_{8.5}Ti_5O_{12}$), there is only a small, 0.4%, volume expansion.[34] Although small, the 1% increase in Ti-O distance that we see would by itself seem to imply a larger change in unit cell volume on discharge than is seen in the diffraction data. The

explanation for this anomalous result was noted above – the expansion in Ti-O distance results from movement of the oxide anions to better screen the added lithium, with no predicted change in Ti position. Consistent with this, we see no change in the EXAFS-detected Ti-Ti distance, in agreement with the zero-strain behavior seen for micron to nano sized chemically lithiated materials.[33] It is this rigidity that allows the material to undergo repeated redox cycling without degradation. These observations imply that there must also be a decrease in Li-O and Ti-Li distances during discharge. These are not detectable in the present experiment, but have been seen very recently using *in situ* neutron diffraction which gave similar inferred changes in Ti oxidation state during cycling.[35]

2.4 CONCLUSIONS

Mesoporous $Li_4Ti_5O_{12}$ microspheres, assembled from nanosheets, were synthesized successfully and investigated as the anode materials in lithium-ion batteries. The material prepared by hydrothermal reaction showed a large surface area, exhibiting excellent cyclability and high capacity retention. It exhibits high capacity retention of 135 mAh/g even after 4000 cycles and can even be cycled at high current density of 10^4 mA/g. The material shows great promise to applications as an anode material in high rate Li-ion batteries. In order to understand the functioning of this promising anode material at the molecular level, we used *in-situ* x-ray absorption spectroscopy (XAS). *In-situ* x-ray absorption spectroscopy confirmed that electrons are added (on discharge) and removed (on charge) from a band of primarily Ti character; the apparent average oxidation state of the fully discharged material is ~ $Ti^{3.5+}$. The first cycle of charge and discharge EXAFS results showed small changes Ti-O distance but no change in Ti-Ti

distance reflecting the fact that in this material, lithiation has the effect of pulling the oxide anions closer together, allowing the Ti-O distance to expand, as required upon Ti reduction, with negligible change in the lattice parameter.

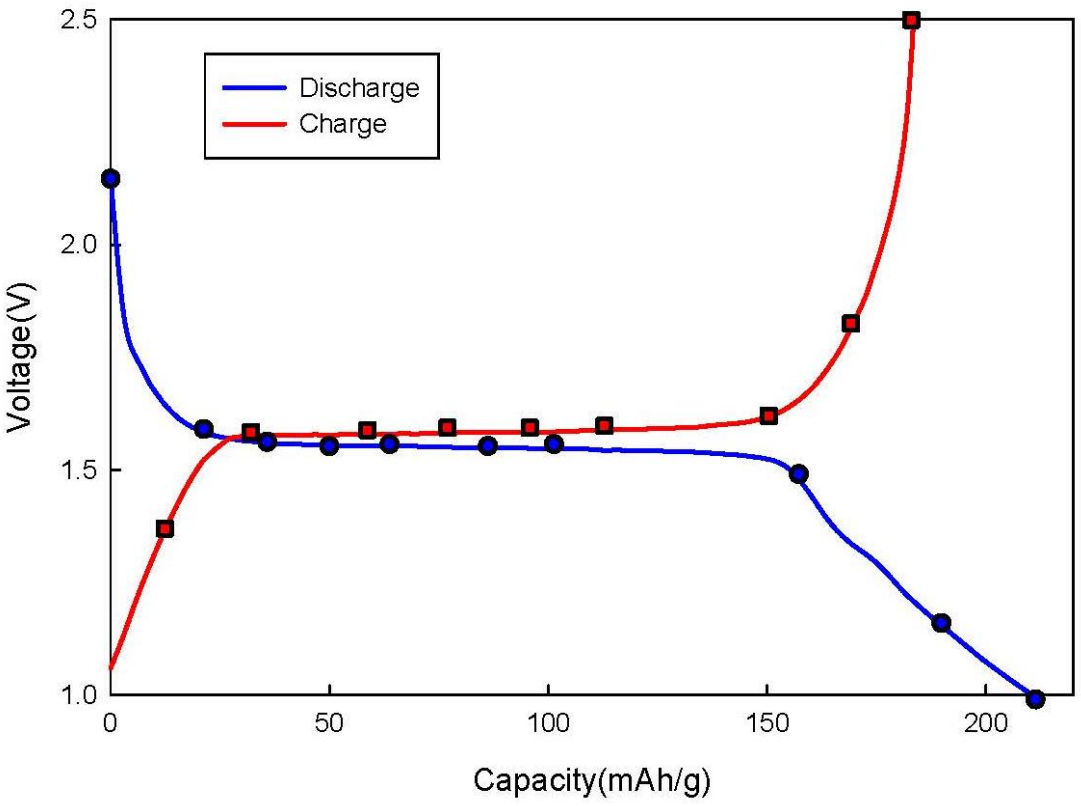

Figure 2.1 Cycling curve of the $Li_4Ti_5O_{12}$ electrode. Labels (circles and squares) shown are the points where the XAS measurements were performed during the discharge/charge cycle.

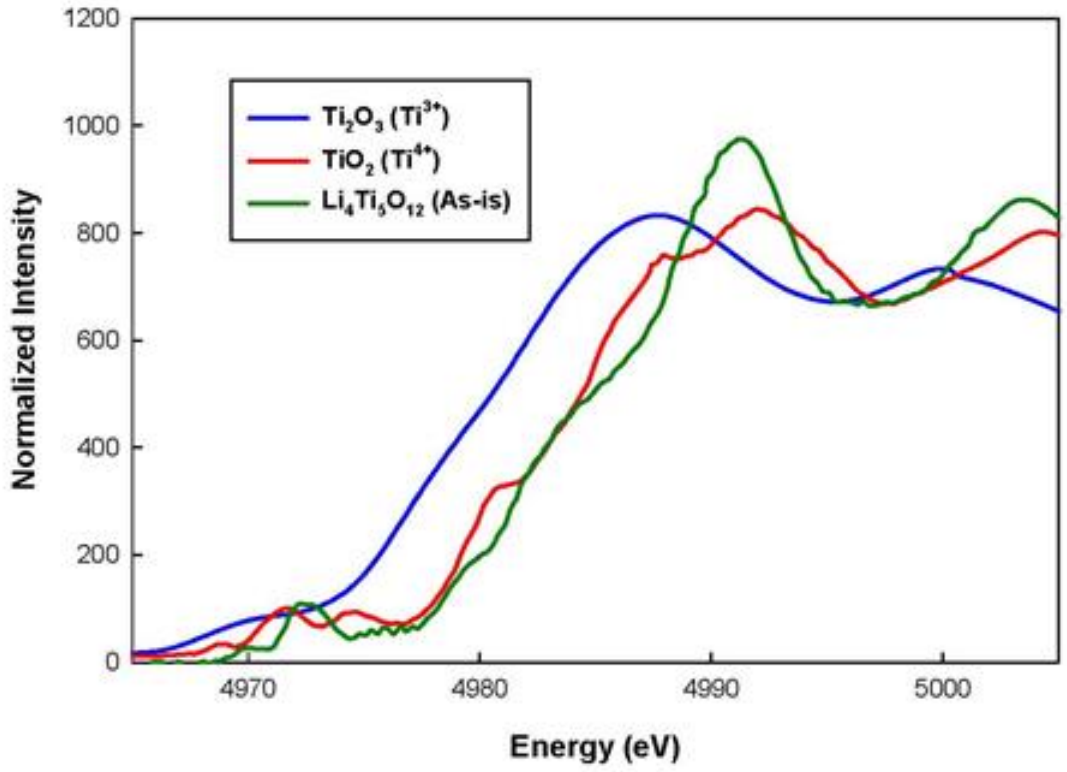

Figure 2.2 Ti-K edge XANES of $Li_4Ti_5O_{12}$ compared to the model compounds Ti_2O_3 and TiO_2.

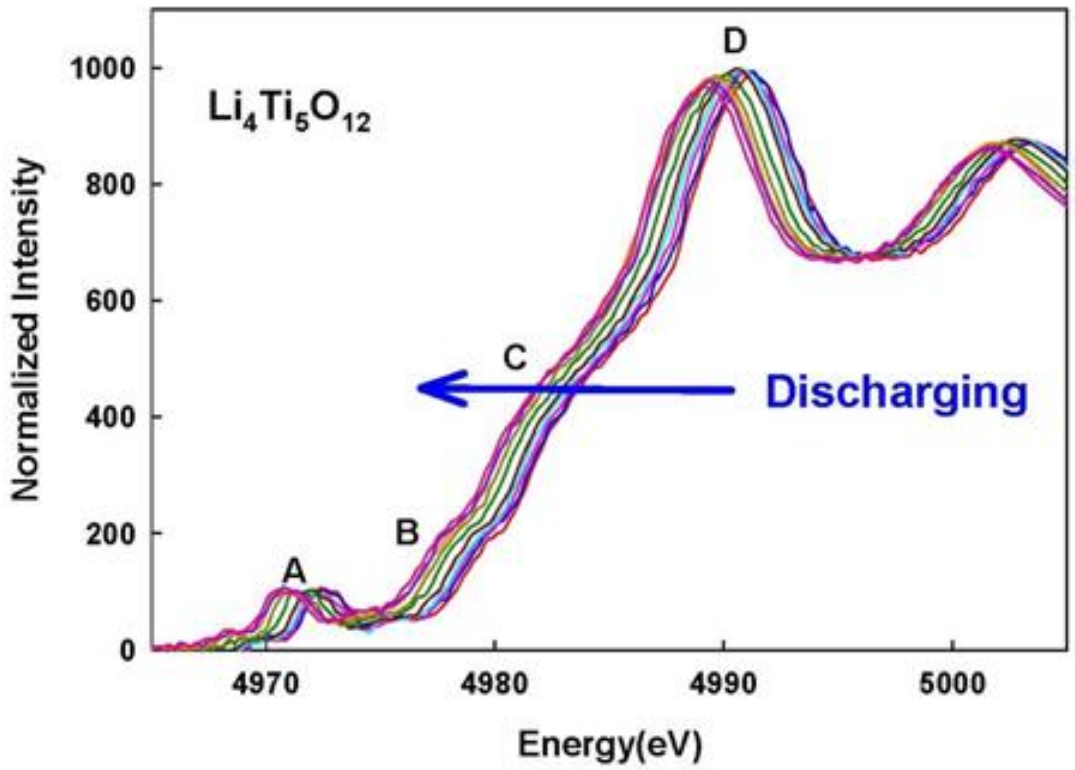

Figure 2.3 *In-situ* Ti-K edge XANES during discharge at capacities shown in **Table 2.1**

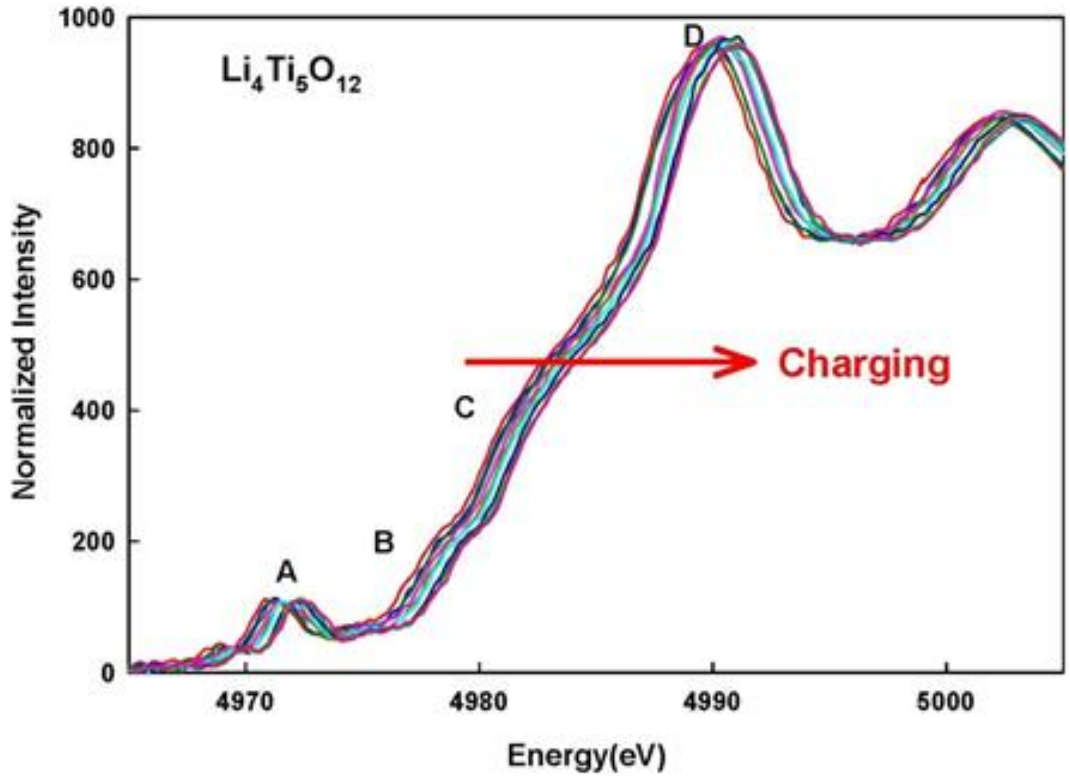

Figure 2.4 *In-situ* Ti-K edge XANES during charge during charge at capacities shown in **Table 2.2**.

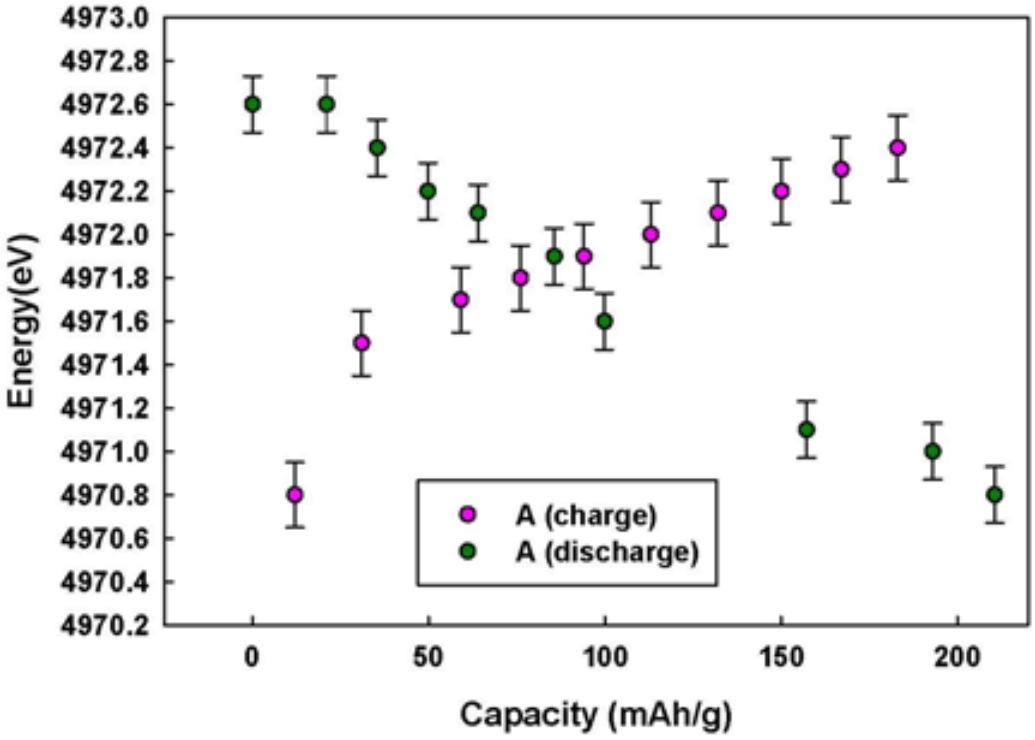

Figure 2.5 Position of Feature A with respect to capacity during cycling. The glavanostatic cyling of the *in-situ* studies was performed at a current density of 175 mA/g, between 2.5 V and 1.0 V. Error bars are the estimated standard deviation in replicate measurements.

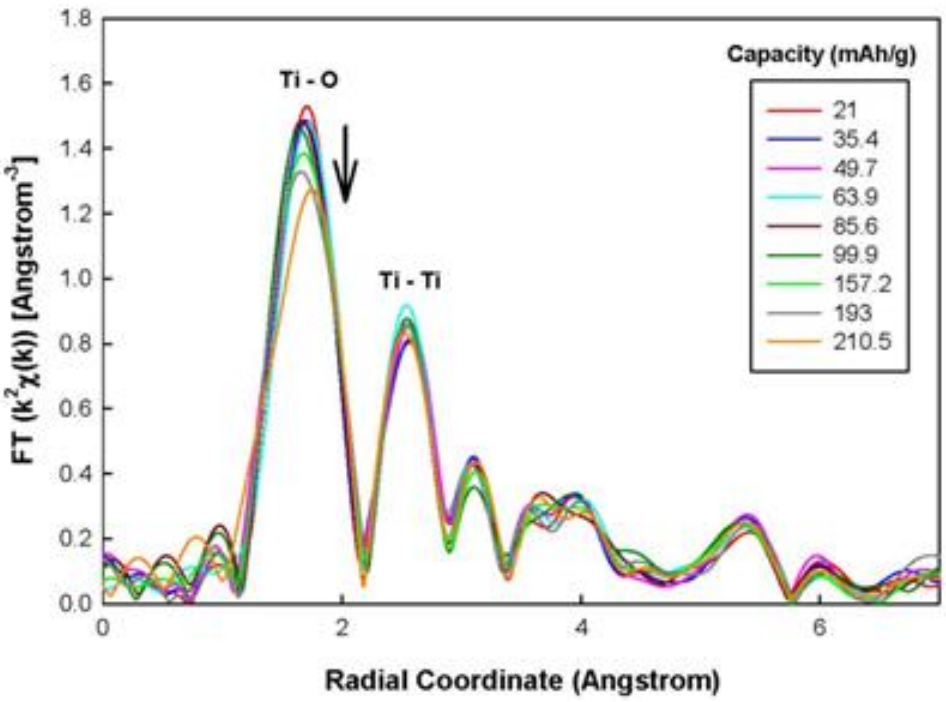

Figure 2.6 Magnitude of the k^3-weighted Fourier transform of $Li_4Ti_5O_{12}$ at the Ti K edge at selected capacity values during the discharge cycle.

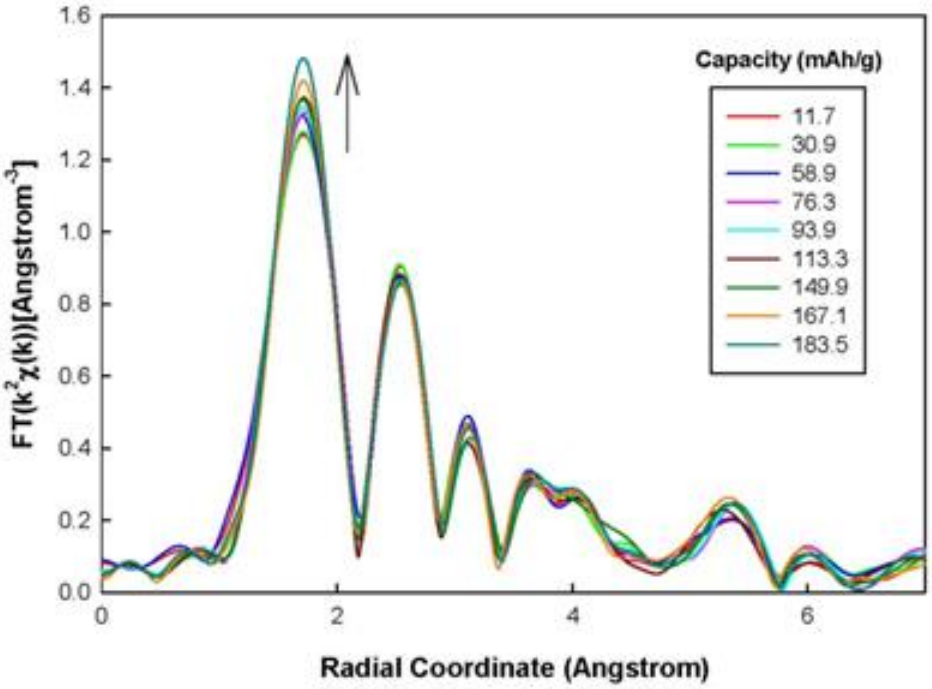

Figure 2.7 Magnitude of the k^3-weighted Fourier transform of $Li_4Ti_5O_{12}$ at the Ti K edge at selected capacity values during the charge cycle.

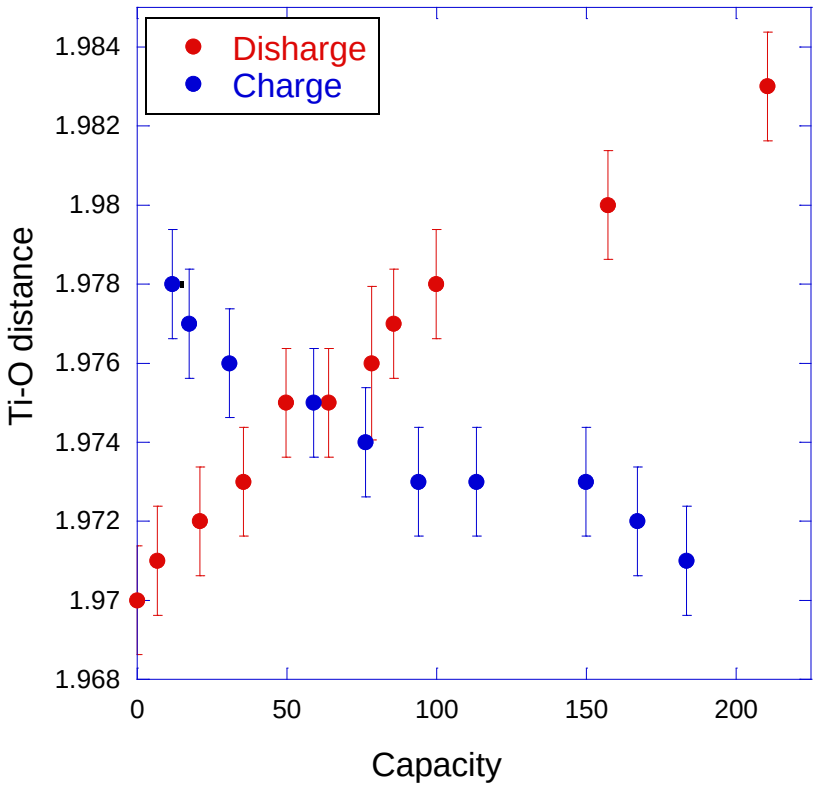

Figure 2.8 Fitted Ti-O bond length for $Li_4Ti_5O_{12}$ during discharge and charge cycle. Error bars are estimated standard error of fitted distance.

Table 2.1 Position of A, B, C and D features in the XANES spectra during discharge.

Capacity(mAhg^{-1})	**Energy (eV)**			
	A	B	C	D
0 (As-is)	4972.6	4978.8	4981.8	4991.3
21	4972.6	4978.7	4981.7	4991.1
35.4	4972.4	4978.5	4981.4	4991.0
49.7	4972.2	4978.2	4981.2	4990.8
63.9	4972.1	4977.9	4981.1	4990.5
85.6	4971.9	4977.6	4980.7	4990.2
99.9	4971.6	4977.3	4980.3	4989.8
157.2	4971.1	4977.1	4980.1	4989.6
193	4971.0	4977.0	4980.0	4989.4
210.5	4970.8	4976.7	4979.7	4989.2

Table 2.2 Position of A, B, C and D features in the XANES spectra during charge.

Capacity(mAhg^{-1})	**Energy (eV)**			
	A	B	C	D
11.7	4971.5	4977.2	4980.3	4989.9
30.9	4971.7	4977.5	4980.5	4990.1
58.9	4971.8	4977.6	4980.7	4990.2
76.3	4971.9	4977.8	4980.8	4990.3
93.9	4972.0	4977.9	4980.8	4990.4
113.3	4972.1	4978.0	4980.9	4990.5
149.9	4972.2	4978.1	4980.9	4990.6
167.1	4972.3	4978.4	4981.3	4990.8
183.5	4972.4	4978.5	4981.5	4990.8

Table 2.3 Best fit results for each state of charge. In all cases except 78.3 $mAhg^{-1}$ (discharge), two spectra were measured for each state of charge. The values reported are from fits to the averaged spectra and (in parentheses) from fits to each individual spectrum. The Ti-O coordination number was fixed at 6, the Ti-Ti coordination number at 6 and ΔE_0 was fixed at 0 eV. The variability in the fitted distances for duplicate scans was used to estimate the rms deviation in bond-length to be 0.0019 Å. These are used to calculate the standard error of the mean values shown in **Figure 2.8**.

Discharge Capacity ($mAhg^{-1}$)	**R_{Ti-O} (Å)**	**$\sigma^2_{Ti-O} \times 10^2$ ($Å^2$)**	**R_{Ti-Ti} (Å)**	**$\sigma^2_{Ti-Ti} \times 10^2$ ($Å^2$)**
0 (As-is)	1.970	1.5	3.03	1.5
6.7	1.971 (1.970,1.971)	1.3 (1.2,1.0)	3.03 (3.03,3.02)	1.6 (1.4,1.2)
21.0	1.972 (1.973,1.972)	1.3 (1.2,1.2)	3.04 (3.04,3.03)	1.4 (1.3,1.1)
35.4	1.973 (1.971,1.975)	1.4 (1.2,1.1)	3.03 (3.03,3.03)	1.4 (1.2,1.3)
49.7	1.975 (1.975,1.974)	1.3 (1.2,1.1)	3.02 (3.02,3.02)	1.4 (1.1,1.2)
63.9	1.975 (1.974,1.976)	1.2 (1.2,1.2)	3.03 (3.02,3.03)	1.4 (1.2,1.4)
78.3	1.976	1.3	3.04	1.4
85.6	1.977 (1.977,1.977)	1.3 (1.3,1.2)	3.04 (3.04,3.04)	1.5 (1.4,1.3)
99.9	1.978 (1.977,1.980)	1.6 (1.5,1.4)	3.03 (3.02,3.03)	1.5 (1.3,1.4)
157.2	1.980 (1.981,1.980)	1.4 (1.4,1.2)	3.03 (3.03,3.03)	1.4 (1.3,1.2)
210.5	1.983 (1.983,1.980)	1.3 (1.2,1.3)	3.03 (3.03,3.04)	1.5 (1.3,1.4)
Charge Capacity ($mAhg^{-1}$)	**R_{Ti-O} (Å)**	**$\sigma^2_{Ti-O} \times 10^2$ ($Å^2$)**	**R_{Ti-Ti} (Å)**	**$\sigma^2_{Ti-Ti} \times 10^2$ ($Å^2$)**
11.7	1.978 (1.978,1.976)	1.3 (1.2,1.2)	3.03 (3.02,3.03)	1.4 (1.3,1.3)
17.4	1.977 (1.977,1.976)	1.3 (1.2,1.2)	3.03 (3.03,3.03)	1.5 (1.3, 1.3)
30.9	1.976 (1.975,1.977)	1.6 (1.4,1.5)	3.03 (3.03,3.04)	1.5 (1.2,1.4)
58.9	1.975 (1.975,1.974)	1.6 (1.5,1.6)	3.03 (3.03,3.02)	1.4 (1.3,1.2)
76.3	1.974 (1.974,1.975)	1.6 (1.3,1.5)	3.02 (3.02,3.02)	1.4 (1.3,1.3)
93.9	1.973 (1.973,1.973)	1.5 (1.4,1.5)	3.03 (3.03, 3.03)	1.5 (1.3,1.3)
113.3	1.973 (1.973,1.972)	1.4 (1.4,1.3)	3.03 (3.03,3.03)	1.5 (1.4,1.4)
149.9	1.973 (1.975,1.972)	1.4 (1.1,1.2)	3.04 (3.04,3.03)	1.5 (1.3,1.4)
167.1	1.972 (1.972,1.972)	1.3 (1.3,1.2)	3.03 (3.03,3.03)	1.5 (1.4,1.3)
183.5	1.971 (1.970,1.973)	1.3 (1.2,1.1)	3.04 (3.04,3.03)	1.5 (1.3,1.3)

2.5 REFERENCES

(1) Whittingham, M. S. *Science* 1976, *192*, 1126.

(2) Cheng, L.; Yan, J.; Zhu, G. N.; Luo, J. Y.; Wang, C. X.; Xia, Y. Y. *Journal of Materials Chemistry* 2010, *20*, 595.

(3) Padhi, A. K.; Nanjundaswamy, K. S.; Goodenough, J. B. *Journal of the Electrochemical Society* 1997, *144*, 1188.

(4) Scrosati, B. *Nature* 1995, *373*, 557.

(5) Jiang, C.; Ichihara, M.; Honma, I.; Zhou, H. S. *Electrochimica Acta* 2007, *52*, 6470.

(6) Wagemaker, M.; Van Der Ven, A.; Morgan, D.; Ceder, G.; Mulder, F. M.; Kearley, G. J. *Chemical Physics* 2005, *317*, 130.

(7) Wagemaker, M.; Simon, D. R.; Kelder, E. M.; Schoonman, J.; Ringpfeil, C.; Haake, U.; Lutzenkirchen-Hecht, D.; Frahm, R.; Mulder, F. M. *Advanced Materials* 2006, *18*, 3169.

(8) Borgel, V.; Gershinsky, G.; Hu, T.; Theivanayagam, M. G.; Aurbach, D. *Journal of the Electrochemical Society* 2013, *160*, A650.

(9) Zhu, G. N.; Wang, Y. G.; Xia, Y. Y. *Energy & Environmental Science* 2012, *5*, 6652.

(10) Chen, J. Z.; Yang, L.; Fang, S. H.; Tang, Y. F. *Electrochimica Acta* 2010, *55*, 6596.

(11) Wang, H. B.; Pan, Q. M.; Cheng, Y. X.; Zhao, J. W.; Yin, G. P. *Electrochimica Acta* 2009, *54*, 2851.

(12) Qiao, H.; Wang, Y. W.; Xiao, L. F.; Zhang, L. Z. *Electrochemistry Communications* 2008, *10*, 1280.

(13) Li, B. X.; Rong, G. X.; Xie, Y.; Huang, L. F.; Feng, C. Q. *Inorganic Chemistry* 2006, *45*, 6404.

(14) Guo, Y. G.; Hu, J. S.; Wan, L. J. *Advanced Materials* 2008, *20*, 4384.

(15) Cao, A. M.; Hu, J. S.; Liang, H. P.; Wan, L. J. *Angewandte Chemie-International Edition* 2005, *44*, 4391.

(16) Tang, Y. F.; Yang, L.; Qiu, Z.; Huang, J. S. *Electrochemistry Communications* 2008, *10*, 1513.

(17) Yang, Z. G.; Choi, D.; Kerisit, S.; Rosso, K. M.; Wang, D. H.; Zhang, J.; Graff, G.; Liu, J. *J Power Sources* 2009, *192*, 588.

(18) Yu, S. H.; Pucci, A.; Herntrich, T.; Willinger, M. G.; Baek, S. H.; Sung, Y. E.; Pinna, N. *J Mater Chem* 2011, *21*, 806.

(19) Lu, J.; Nan, C. Y.; Peng, Q.; Li, Y. D. *J Power Sources* 2012, *202*, 246.

(20) Kim, S.; Fang, S. H.; Zhang, Z. X.; Chen, J. Z.; Yang, L.; Penner-Hahn, J. E.; Deb, A. *J Power Sources* 2014, *268*, 294.

(21) Deb, A.; Bergmann, U.; Cairns, E. J.; Cramer, S. P. *Journal of Synchrotron Radiation* 2004, *11*, 497.

(22) Rumble, C.; Conry, T. E.; Doeff, M.; Cairns, E. J.; Penner-Hahn, J. E.; Deb, A. *Journal of the Electrochemical Society* 2010, *157*, A1317.

(23) Weng, T. C.; Waldo, G. S.; Penner-Hahn, J. E. *Journal of Synchrotron Radiation* 2005, *12*, 506.

(24) Newville, M. *Journal of Synchrotron Radiation* 2001, *8*, 322.

(25) Victoreen, J. A. *Journal of Applied Physics* 1948, *19*, 855.

(26) Rehr, J. J.; Kas, J. J.; Vila, F. D.; Prange, M. P.; Jorissen, K. *Phys Chem Chem Phys* 2010, *12*, 5503.

(27) Degroot, F. M. F.; Fuggle, J. C.; Thole, B. T.; Sawatzky, G. A. *Phys Rev B* 1990, *41*, 928.

(28) Farges, F. *J Non-Cryst Solids* 1996, *204*, 53.

(29) Farges, F.; Brown, G. E.; Rehr, J. J. *Geochimica Et Cosmochimica Acta* 1996, *60*, 3023.

(30) Farges, F.; Brown, G. E.; Rehr, J. J. *Physical Review B* 1997, *56*, 1809.

(31) Ohzuku, T.; Ueda, A.; Yamamoto, N. *J Electrochem Soc* 1995, *142*, 1431.

(32) Penner-Hahn, J. E. *Coordin Chem Rev* 1999, *192*, 1101.

(33) Borghols, W. J. H.; Wagemaker, M.; Lafont, U.; Kelder, E. M.; Mulder, F. M. *Journal of the American Chemical Society* 2009, *131*, 17786.

(34) Zhong, Z. Y.; Ouyang, C. Y.; Shi, S. Q.; Lei, M. S. *Chemphyschem* 2008, *9*, 2104.

(35) Pang, W. K.; Peterson, V. K.; Sharma, N.; Shiu, J. J.; Wu, S. H. *Chem Mater* 2014, *26*, 2318.

CHAPTER III

INVESTIGATION OF ELECTRONIC STRUCTURE OF SPINEL $LiMn_2O_4$ WITH ANNEALING

3.1 INTRODUCTION

This chapter describes characterization of the spinel material $LiMn_2O_4$ using X-ray Absorption Spectroscopy. The $LiMn_2O_4$ (LMO) sample was prepared by the Bartlett group.[1] The spinel $LiMn_2O_4$ is a well-known material that has recently drawn considerable interest for use as a cathode material for rechargeable lithium batteries. In order to investigate the potential of this material, X-ray Absorption Spectroscopy was performed to explore the electronic structure of $LiMn_2O_4$ as a function of annealing state.

Spinel $LiMn_2O_4$ is a candidate for the positive electrode active material within Li rechargeable batteries due to a combination of low cost, benign environmental impact, and high specific energy. Both $LiMn_2O_4$ and delithiated $Li_xMn_2O_4$ possess a spinel structure where the Li atoms occupy the tetrahedral sites and the Mn atoms occupy the octahedral sites. The Mn^{4+} atoms in $LiMn_2O_4$ possess cubic symmetry, whereas the Mn^{3+} atoms undergo a Jahn-Teller distortion that causes an expansion of the spinel lattice. Successive expansion and contraction of the lattice during cycling of the electrode can cause structural breakdown. This is thought to be

major contributor to the capacity fading observed upon repeated cycling which prevents these systems from being successfully commercialized.[2-5] However, the fact that there are many open sites (88% of T_d sites and 50% of O_h sites) allows for various methods to maintain cubic structure during electrochemical cycling by Li substitution on the octahedral sites, or forming oxygen vacancies. [6] Forming oxygen vacancies would lead to a lower oxidation state of Mn which has some harmful effects on the lithium mangano spinel; for example, the structure would undergo a Jahn-Teller distortion by containing Mn^{3+}. Therefore, removing oxygen vacancies, by using hydrothermal synthesis, for example, will be an important issue in LMO studies.

Hydrothermal synthesis of lithium mangano-spinel performed under a pure oxygen atmosphere followed by annealing at 500 C for 4 h in air gives superior electrochemical properties compared to those unannealed sample.[6,7] Annealing is a heat treatment wherein diffusion across grain boundaries yields a stronger material. It is a process that produces conditions by heating, maintaining a suitable temperature, and then cooling slowly. For $LiMn_2O_4$ it is believed that annealing in air can eliminate oxygen vacancies which form during hydrothermal synthesis.[6,7]

Alternatively, it is possible that annealing results in anti-site migration of a portion of the Mn into Li sites. As originally synthesized, $LiMn_2O_4$ has an orthorhombic super lattice structure Fddd, and the annealed sample is cubic (Fd-3m).[6,7] Originally, a super lattice results from charge-ordering of the Mn ions, along with long range-ordering of the lithium ions. This happens when lithium ions are removed from an intermixed layer causing a local distortion in the surrounding atoms, which then energetically favors the further removal of lithium ions from the

same layer. Therefore, we used XAS to determine the consequence of annealing on the local structure of the Mn.

3.2 EXPERIMENTAL

3.2.1 Hydrothermal synthesis and annealing

Compounds in spinel structure were prepared by the Bartlett group following the synthetic procedure discussed in detail in the literature.[1,6,7] It starts with the reaction of 0.158 g (1.00 mmol) $KMnO_4$ in 12 mL 0.1 M LiOH(aq) with 1.00 mmol of acetone. Reactions were carried out in 23 mL PTFE-lined, stainless-steel Parr autoclaves and they were sealed in a Plas-Lab wet box. Lithium hydroxide solution was purged with N_2 gas or O_2 gas prior to sealing in the wet box under the same N_2 or O_2 atmosphere. Autoclaves were heated to 200 ˚C at a rate of 10 ˚C min^{-1}. After a 5 h dwelling time, reactions were cooled to room temperature at a rate of 5 ˚C min^{-1}. Powders were collected by centrifugation and then washed several times with deionized water and dried overnight under vacuum at 120 ˚C. Then, the annealing step was performed in an MTI compact muffle furnace at 500 ˚C for 4 h under room atmosphere.

3.2.2 X-ray Absorption Spectroscopy (XAS), sample preparation & data collection

LMO samples (3−7 mg) were diluted with boron nitride(BN), ground to a fine powder, and pressed in an aluminum frame sealed with Kapton tape on both sides. Duplicate samples were prepared for both the pre-annealed and the annealed LMO. Mn K-edge X-ray absorption spectra were collected at the Stanford Synchrotron Radiation Laboratory (SSRL) on beamline 7-3 at room temperature. The energy was selected using a Si [220] double crystal monochromator

and harmonics were rejected using a Rh-coated flat Si mirror. Data were measured in transmission mode using N_2 filled ion chambers, and the x-ray energy was calibrated by reference to a $KMnO_4$ calibration standard, with the energy of the peak in the $KMnO_4$ pre-edge peak defined as 6543.3 eV. Mn K-edge spectra were collected using 5 eV steps in the pre-edge (6308−6528 eV), 0.2 eV steps from 6528-6558 eV and 0.05 $Å^{-1}$ steps in the EXAFS region to k= 19 $Å^{-1}$. Data collection was integrated for 1 s in the pre-edge, 1.5 s in edge regions, and 1.5 to 25 s (k^2-weighted for k= 2.6 to 8 $Å^{-1}$ and k^3-weighted for k= 8 to 19 $Å^{-1}$) in the EXAFS region for total scan time of roughly 30 min. Two to six scans were averaged for each sample.

3.2.3 Normalization: MBACK

In order to obtain quantitative analysis of near–edge features, it is important to have accurate normalization of X-ray absorption data. Many of the data reduction methods used for XANES data have been adopted from those used for EXAFS data-reduction. In some cases, those general approaches have led to significant errors in normalization. To minimize the errors, an alternative approach called MBACK is used. Data normalized via MBACK showed significantly improved reproducibility and reliability. This provides sufficient precision to distinguish chemically induced spectral changes that are obscured by conventional normalization.[8] MBACK normalizes XAS data by calculating a smooth normalizing function over the entire measured data range, rather than the conventional way which a second-order polynomial was fitted to the raw data in the pre-edge region and extrapolated through the post-edge region.

3.2.4 Fitting program: EDG_FIT (Lorentzian + Gaussian function)

A challenge in analyzing the 1s → 3d region is to separate the very weak 1s → 3d transitions from the intense rising edge. Our approach to this was to fit both the 1s → 3d transition regions and the rising background. The intensities and energies of the pre-edge were quantitated by least-squares fits of the data. The fitting program EDG_ FIT was used to fit the 1s → 3d region with a pseudo-Voigt function. Pseudo-Voigt shaped peaks take into account the convolution of true peak shape (Lorentzian contribution) with the experimental energy resolution (Gaussian contribution). The normalized pseudo-Voigt function is shown below **Eq 3.1-3.3**:

$$f_{pv}(x)=(1-\eta)f_G(x;\gamma_G)+\eta f_L(x;\gamma_L), \quad \textbf{Eq. 3.1}$$

Where, $f_G(x;\gamma_G)$ and $f_L(x;\gamma_L)$ are the normalized Gaussian and Lorentzian functions, with FWMH $\Gamma=2(\ln 2)^{1/2}\gamma_G=2\gamma_L$,

$$f_G(x;\gamma_G)=(1/\pi^{1/2}\gamma_G)\exp(-x^2/\gamma^2_G), \quad \textbf{Eq. 3.2}$$

$$f_L(x;\gamma_L)=(1/\pi\gamma_L)(1+x^2/\gamma^2_L)^{-1} \quad \textbf{Eq. 3.3}$$

η is the parameter which mixes two functions. η (the "Lorentz fraction") and $(1-\eta)$ represent the fractions of each used. In this experiment η equals to be 0.5.[9]

The pre-edge features were modeled by pseudo-Voigt line shapes which are simple sums of Lorentzian and Gaussian functions and the energy position, the full width at half-maximum (FWHM) and the peak height were varied.[10-12] A fixed 1:1 ratio of Lorentzian to Gaussian functions revealed the spectral features of the pre-edge transitions. All spectra were fit with three

peaks centered initially at 6537, 6539, and 6540 eV and with initial threshold energy for the rising edge of 6545 eV. Functions modeling the pre-edge peaks and one function modeling the background were needed to obtain a good match to the data over the range 6530-6540 eV, while functions modeling 1s → 3d transition on the rising edge were needed to obtain a good match to the data over the range 6530-6545eV. RMS (Root Mean Square) error shows the difference of the values predicted by the model and the values actually observed from the sample being modeled. Therefore, RMS error can be used to quantify how well it fits by the standard deviations for the peak energies and intensities which were calculated from all the pseudo-Voigt functions that fit the pre-edge features from all the fits for each sample.[13]

3.2.5 Fitting program: EXAFSPAK

EXAFSPAK is a suite of XAS data analysis programs. The data for each sample were calibrated with reference to the absorption spectrum of a simultaneously-measured sample of $KMnO_4$, with the energy of the pre-edge peak of $KMnO_4$ defined as 6498.30 eV. At least two independent scans were averaged for each sample. The background was removed by first fitting a (-1) order polynomial to the region before the edge: after background subtraction, a four region cubic spline was fit to the EXAFS region (k= 1~11). Monochromator crystal glitches required truncation of the data at 12 $Å^{-1}$. Non-linear least squares curve fitting of the EXAFS data used ab initio phase and amplitude functions calculated by the program FEFF 7.02 (University of Washington),[14,15] assuming pairs of atoms at fixed distances. A scaling factor S_0^2 of 0.9 was used for all fits. The fitting program, OPT in EXAFSPAK was used for the curve-fitting EXAFS data

to obtain structural information. The EXAFS equation, used by OPT in its most complete form is shown below in **Eq. 3.4**:

$$\chi(k)=S^2_0\sum_{i=1}^{n}\frac{N_i S_i(k,R_i)F_i(k,R_i)}{kR^2}\exp\left(\frac{-2R_i}{\lambda(k,R_i)}\right)\exp(-2\sigma_i{}^2k_i{}^2)\sin[2kR_i+\phi_i(k,R_i)+\phi_c(k)]. \quad \textbf{Eq. 3.4}$$

Variable Meaning:

k – Photo-electron wave number, a measure of the photoelectron wavelength, $k = 2\pi/\lambda_e$, and calculated from the X-ray energy above the threshold by $k = [0.262(E-E_0)]^{1/2}$

$\mathbf{S_0^2}$– Amplitude reduction factor due to shake up and shake off losses (otherwise known as the scale factor in OPT).

$\mathbf{N_i}$ – Coordination number for atom type i.

$\mathbf{F_i}$ – Effective EXAFS scattering amplitude functions.

$\mathbf{R_i}$ – Absorber-backscatterer distance for atom i.

$\boldsymbol{\sigma_i}$ – Debye-Waller factor, the mean square deviation in R_i . $\boldsymbol{\varphi_i}$ – Backscatterer EXAFS phase function.

$\boldsymbol{\varphi_c}$ – Central atom EXAFS phase function. OPT adds φ_c and φ_i for each backscatterer. φ_c depends only on the edge and the type of atom that is absorbing, φ_r, on the other hand, depends on R_i and upon the type of back scatterer atom. [16]

Generalized variables for constraints in above equation are path parameters which are $\Delta\mathbf{R}$, $\boldsymbol{\sigma i^2}$, $\mathbf{S_0^2}$, **N**, $\mathbf{E_0}$ and FEFF program calculates $\mathbf{F_i}$ (*k*). Rest of the values are theoretically calculated values such as $\boldsymbol{\varphi_c}(k)$, $\boldsymbol{\lambda}(k)$, and $\mathbf{R_0}$.

3.3 RESULTS

The normalized XANES spectra of annealed and pre-annealed samples are shown in **Figure 3.1**. The two spectra are nearly identical, with only subtle differences. The edge energy for the annealed sample shifts slightly (~0.36 eV) to higher energy than the pre-annealed sample. To understand the difference quantitatively, based on reference spectra[17], 1 valence change of $Mn^{3+} \rightarrow Mn^{4+}$ is approximately 2.7 eV, suggesting that the annealed sample is ≈ 14% more oxidized than the pre-annealed sample. From this result (≈ 14%), the actual manganese valence can be calculated. The pre-annealed sample is 14% less oxidized; therefore, the calculation should be $((Mn^{3+})_{1.28}(Mn^{4+})^{0.72})/2=$ **$Mn^{3.36+}$**n and annealed should be **$Mn^{3.5+}$**. From the standpoint of the calculated result, it is expected but it is not what is seen from this experiment; this would be some kind of pattern that should be seen from the experiment result.

As shown in **Figure 3.1** inset (a), the pre-edge region for Mn in all the spectra exhibits two resolved peaks at around 6536 and 6538 eV, denoted by A and B. It shows that A is slightly better resolved in the annealed sample which may be related to the disordering character of the material without annealing. Inset (b) shows the pre-edge region between 6530 eV and 6580 eV. The pink line in Inset (b) represents minor differences in the pre-edge region from the subtraction of the annealed sample from the pre-annealed one ((annealed-pre-annealed)*10+700). To understand the differences between the two spectra, 1s → 3d pre-edge fitting and area calculation is necessary, giving an area of 87 (for annealed sample) and 81 (for pre-annealed) sample.

As seen in **Figure 3.1**, the highest intensity peak energy from annealed sample shifts towards a higher energy range than the one from pre-annealed sample. This supports the idea that

annealing helps the sample to become more oxidized compared to the samples without the annealing effect. This idea should be verified qualitatively by pre-edge fitting the 1s → 3d region where Mn^{3+} is expected to fit with 3 or 4 peaks (depending on whether B_{2g} and E_g are resolved) and another 2 different peaks for Mn^{4+} (different change and probably shifted to higher energy), giving a total of 5 or 6 peaks. Since we cannot fit all of these, we are forced to fit approximately 3 peaks. **Figure 3.2** shows the fits to the annealed sample using 2 peaks, 3 peaks, and 4 peaks. The red, blue, and green solid lines represent the differences of the experimental data and fitting in order to present how close the fitting has been approached to the real experimental data. The 2 peak fit (blue) is significantly worse than the others and has obvious features above the noise level. It is hard to distinguish between the 3 peak and the 4 peak fit. In order to compare these, further analysis was needed. The 4 peak fits shows huge energy shifts which are physically impossible while the fitted energies with 3 peaks are highly reproducible. We can conclude that no more than 3 peaks could be reliably resolved. As shown in **Figure 3.3,** there is a slight shift (0.5 eV) to the higher energy range in third peak's fit in the annealed sample. The change is relatively small but it is reproducible (see **Table 3.1**), suggesting that it reflects a real variation.

As expected from the similarity in the XANES, there is not much change in the EXAFS for the two samples. In every case, the data can be fit with a single shell of oxygen at an average distances of 1.99 Å. Chemically, this is not reasonable, since Mn(III) will have a Jahn-Teller distortion, giving at least two different Mn-O distances. Rather, this reflects the limited resolution of the EXAFS data. Although there is a small improvement in the fit if two shells of Mn-O nearest neighbors are used, these fits are not well defined. In order to explore whether there might be subtle changes in the Mn-O shells on annealing, a set of fits were performed in

which the total coordination number was held constant at 6 and only the ratio of short (~1.9Å) to long (~2.3Å) shells was changed. These fits are summarized in **Figure 3.4**. The minima in **Figure 3.4** represents the best set of coordination numbers within the assumption that there are two Mn-O shells with a total Mn-O correlation number of 6. In the figure, the annealed sample shows the minimum y value at (N=4.7, N=1.3) combination and the pre-annealed sample shows the minimum at (N=4.6, N=1.4). These are marked by the vertical lines.

3.4 DISCUSSION

As discussed above, annealing significantly improves the cycling stability of $LiMn_2O_4$. Since this is accomplished without any significant change in the diffraction pattern, there are two main possibilities: 1) anti-site mixing, in which a small fraction of the Mn exchanges with Li, and 2) oxidation, in which a small number of oxygen vacancies in the as-prepared material are filled, with a consequent small increase in the Mn(IV):Mn(III) ratio.[6]

One of the most noticeable changes from the annealing process is that the resolved third peak shifts by 0.5 eV (**Figure 3.3**). This makes sense in regards to the small change observed in XANES spectra (**Figure 3.1**) and EXAFS study (**Figure 3.4**). The slight energy shift from **Figure 3.3** is consistent with oxidation of Mn in the annealed sample. These results also correspond to the decrease in oxygen vacancies in the annealed sample compared to the pre-annealed sample, and ultimately lead to more oxidation in the annealed sample than in the pre-annealed sample. This supports the idea that the annealing process may help the material to be a better stabilized structure than before.

Generally, the intensity of the dominant main-edge peak in the ordered materials appears to be greater relative to the edge jump, than in disordered materials of a given composition.[18] The 1s → 3d transition is electric dipole-forbidden for centrosymmetric sites, but can gain intensity through 3d+4p mixing in non-centrosymmetric sites.[11] Although the absolute intensity depends on the details of metal ligation, it is generally the case that for Fe and Mn sites, tetrahedral geometries have 1s → 3d intensities ~4-fold larger than those seen in the corresponding octahedral sites.[13] Therefore, the absence of change in the 1s → 3d area strongly suggests that there is no anti-site mixing. The observed 1s → 3d intensity will be I_{Oct} + I_{Tet}; assuming $I_{Tet}=4I_{Oct}$, and x as the fraction of Mn in tetrahedral sites, the intensity will be $(1+3x)I_{Oct}$. Consequently, even a 1% increase in tetrahedral Mn should give a 3% increase in 1s → 3d intensity. We see no detectable change in 1s → 3d intensity. Empirically, our normalization error is 0.2%, suggesting that there is no significant change in tetrahedral Mn. Also, with the calculation of the increase in 1s → 3d area, the result was annealed sample: (~ 87) and pre-annealed sample: (~81). Thus we can conclude that the increase in 1s → 3d area between annealed and pre-annealed is actually no larger than 0.7%. This sets an upper limit of about 0.2% to 0.3% as the maximum amount of tetrahedral Mn that could be created by annealing. Our data are consistent with there being no tetrahedral Mn sites, within experimental uncertainty.

Since the ligand field splitting is much smaller for tetrahedral Mn, we would expect to see only one resolved 1s → 3d transition, and thus there should be some change in the relative intensities such that octahedral Mn sites show better resolved splitting of the 3d orbitals than tetrahedral Mn sites. The relative intensities of tetrahedral Mn would be expected to give 1 significantly higher peak if some tetrahedral Mn were present in addition to octahedral Mn.

One of the distortions that can occur is the Jahn-Teller distortion from Mn^{3+} in the $LiMn_2O_4$ mixed valence system where tetragonal distortion would occur.[19] By either distortion processes, the symmetry will descend from O_h to D_{4h} and the descent in symmetry causes a partial lifting of the degeneracies among the d orbitals in the octahedral field. Due to the fact that two E_g orbitals of the octahedral field become non-degenerate as A_{1g} (d_z^2) and B_{1g}($d_{x^2-y^2}$) in the tetragonal field and the T_{2g} orbital becomes B_{2g} (d_{xy}) and E_g (d_{xz}, d_{yz}),[13] a significant energy pattern changes should occur if the symmetry changes from O_h to D_{4h}. However, such changes are not observable from any of the figures in this chapter.

The average Mn-O distance decreases slightly from annealed sample as expected for oxidation from Mn^{3+} to Mn^{4+}. As shown in **Table 3.2** the average distance of Mn-O 1.9840 Å and Mn-Mn 2.9001 Å in annealed material for 2 independent measurements; Mn-O 1.9907 Å and Mn-Mn 2.9055 Å in pre-annealed material for 4 independent measurements were fitted by the EXAFSPAK program. The accuracy of EXAFS bond length determination is typically taken as ~0.02 Å and the observed Mn-O distance for $LiMn_2O_4$ is in agreement with the Mn-O distance predicted from neutron diffraction data for $LiMn_2O_4$ (1.9547 Å).[6] The experimental precision for the data can be determined by the standard deviation value. The standard deviations for the 4 independent measurements in pre-annealed material are as follows; Mn-O (± 0.0006) & Mn-Mn (±0.0004), and standard deviations for the 2 independent measurements in annealed material are Mn-O (± 0.0010) and Mn-Mn (± 0.0009) which represent the precision of the data. Therefore, it seems that the precision of EXAFS bond-length determination is much better than its accuracy. As a consequence, even though the accuracy is only ~0.02 Å,[20] we nevertheless are able to detect a small change in Mn-O distance as an effect of annealing. In addition, the

decrease of the average Mn-O distance by the annealing effect is expected and is attributed to the $LiMn_2O_4$ system. **Table 3.2** also presents the average distance of Mn-O and Mn-Mn from the previous neutron diffraction data of annealed and pre-annealed samples in reference.[6] Overall, it is possible to acknowledge that the Mn-O distance in the annealed system decreases a bit, as seen by either method (EXAFS and Neutron diffraction), and this is ultimately consistent with the slight oxidation changes between Mn^{3+} and Mn^{4+}. In addition, there must be more than one Mn-O distance, but it is difficult to resolve the different shell. But starting with the assumption that all of the Mn are octahedral and can be described by a short and a long Mn-O shell, we are able to see a small decrease in the amount of the long Mn-O shell upon annealing (See **Figure 3.4**). The long shell is due to the Jahn- Teller distorted Mn^{3+}, so this is consistent with the conclusion that a small amount of Mn^{3+} is oxidized to Mn^{4+} on annealing. This is because, when Mn gets oxidized towards Mn^{4+}, the averaged distance of Mn-O will shrink, which is shown by the FT results in **Table 3.2**.

3.5 CONCLUSION

It was quite difficult to observe a significant change with annealing for the $LiMn_2O_4$ material through the X-ray Absorption Spectroscopy technique. Overall, almost no substantive change was discovered from this experiment. However, with careful analysis small changes were noticed. For example, one thing that changes is edge energy, even though the change is small. The material was expected to contain $Mn^{3.5+}$, based on result of calculation ($Mn^{3.36+}$), before annealing is somewhat less oxidized than 3.5. It's notable that there is no significant change in the 1s $\rightarrow$3d area. The absence of change allows the exclusion of the formation of more than

0.3% tetrahedral Mn. The average Mn-O distance decreases slightly, as expected for oxidation from Mn^{3+} to Mn^{4+}. There must be more than one Mn-O distance, but it is difficult to resolve the different shell. However, starting with the assumption that all of the Mn are octahedral and can be described by a short and a long Mn-O shell, from these results, we were able to see a small decrease in the amount of the long Mn-O shell upon annealing. The long shell is due to the Jahn-Teller distorted Mn^{3+}, so this is consistent with the conclusion that a small amount of Mn^{3+} is oxidized to Mn^{4+} on annealing. Overall, the change made from annealing was minimal. It will be worth exploring other spectroscopic techniques other than XAS to discover whether annealing affects the change in terms of electronic structure of the $LiMn_2O_4$ material.

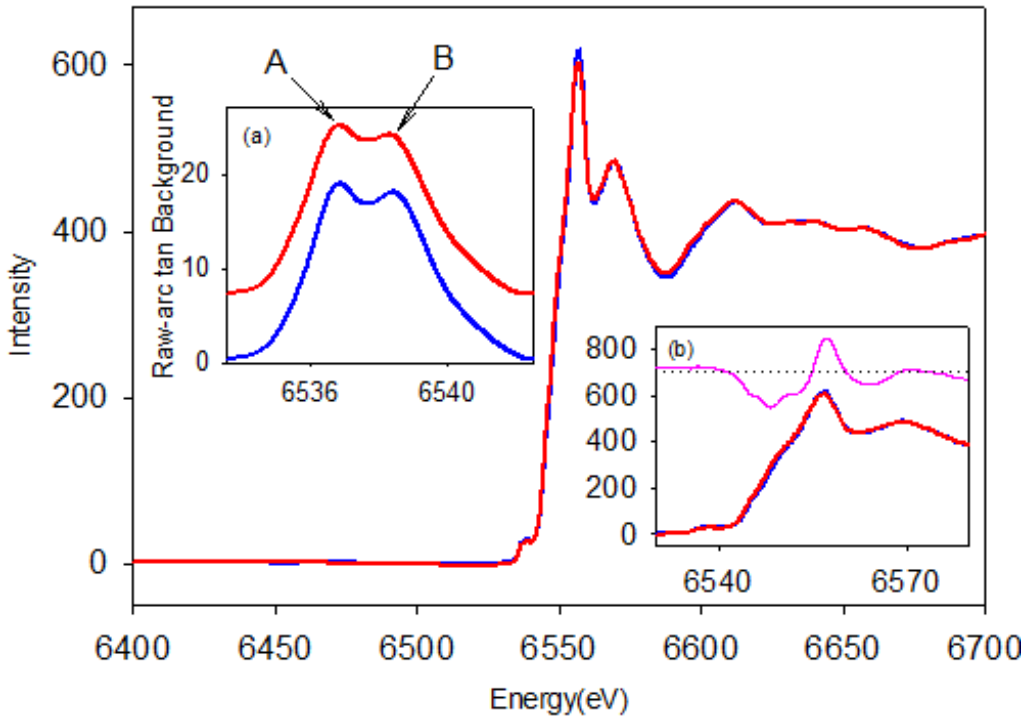

Figure 3.1 Normalized XANES spectra of $LiMn_2O_4$ sample comparison of pre-annealed (red) and annealed (blue) sample. Inset (a) shows the raw-arctan background, A and B (6536 and 6538 eV) indicates the 1s → 3d transition. Annealed (blue) is better resolved than pre-annealed (red). Inset (b) shows the pre-edge region between 6530 eV to 6580 eV, pink solid line ((annealed-pre-annealed)*10+700) shows the difference between the two given plot, black dotted line represents the zero line, at 700.

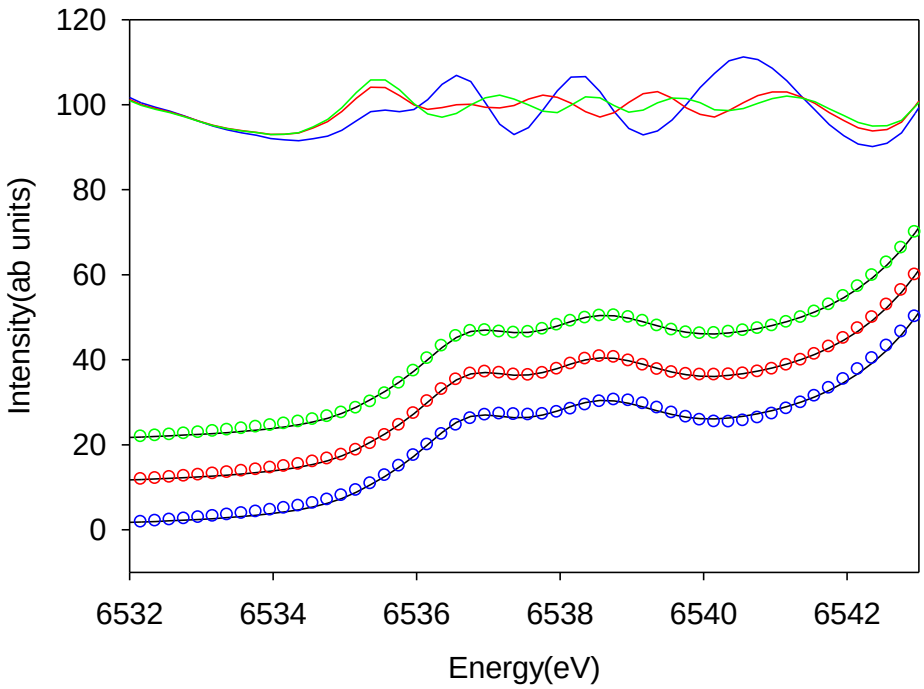

Figure 3.2 The comparison between fit with 2 Voigt peaks, 3 Voigt peaks and 4 Voigt peaks: ◇ (anneal_fit_2peak), ◇ (anneal_fit_3peak), ◇ (anneal_fit_4peak), — ((anneal–anneal_fit_2peak)*10+100), — ((anneal–nneal_fit_3peak)*10+100), — ((anneal–anneal_fit_4peak)*10+100)

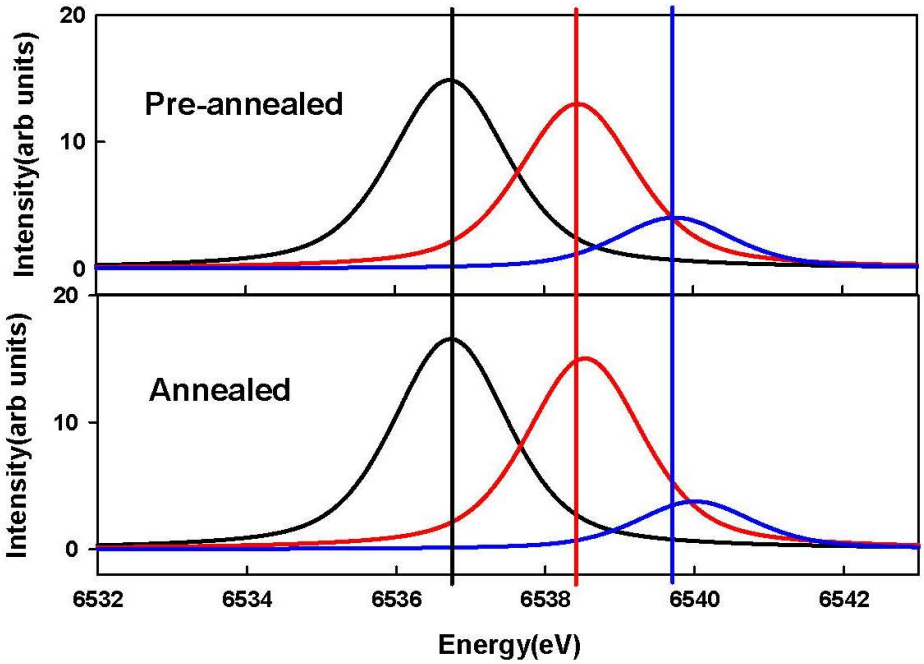

Figure 3.3 Fitting the pre-edge with EDG_FIT program, a comparison between annealed and pre-annealed sample can be made. The changes in the fitted intensities of the 1s → 3d transition from each annealed and pre-annealed samples are based on fitting with 3 peaks. The 3 different Gaussian plots are present, such as Peak1 (black), Peak2 (red), and Peak3 (blue). Only Peak3 is moving towards higher energy from the annealed sample. Fitting with 4 peaks varies significantly with the ones with 3 peaks. Four peaks fitting do not make sense chemically.

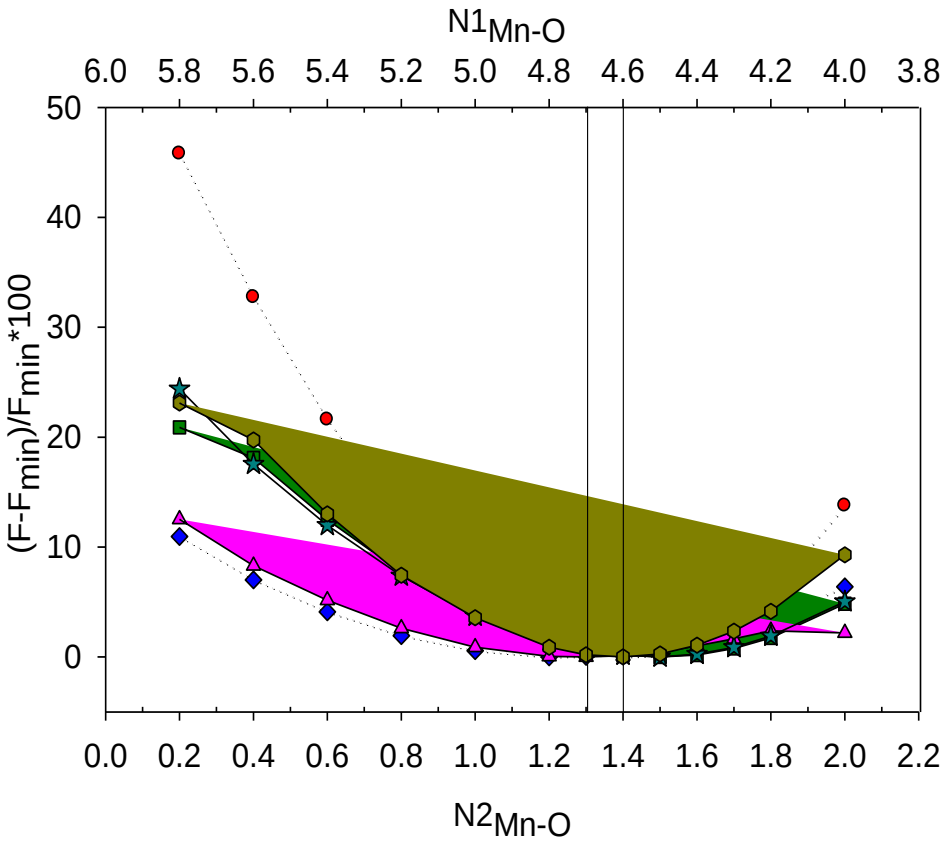

Figure 3.4 anneal1( ), anneal2( ), pre1( ), pre2( ), pre3( ), pre4( ) (a) The comparison of the F factor between annealed and pre-annealed sample in shell splitting, driven by EXAFS fitting with EXAFSPAK. Y axis, $(F-F_{min})/F_{min}*100$: relative deviations of F factor from each sample's minimum F values. The minimum F value marked with vertical lines: $N1_{Mn-O}$=4.7, $N2_{Mn-O}$ =1.3 for annealed sample, and $N1_{Mn-O}$ =4.6, $N2_{Mn-O}$ =1.4 for pre-annealed sample.

Table 3.1 Numerical values of the highest intensity peak of the each Gaussian function from **Figure 3.3** (a) fitting with 3 peaks. Only, peak 3 shows the change not like peak 1 and peak 2. The samples in the table are 4 different pre-annealed samples and 2 different annealed samples.

	Peak 1	**Peak 2**	**Peak 3**
Anneal_1	6536.76	6538.55	6540.35
Anneal_2	6536.71	6538.52	6540.12
Pre-anneal_1	6536.70	6538.53	6539.71
Pre-anneal_2	6536.73	6538.53	6539.74
Pre-anneal_3	6536.73	6538.53	6539.74
Pre-anneal_4	6536.73	6538.53	6539.74

Table 3.2 The comparison of Mn-O, Mn-Mn average distance made out from EXAFS analysis by EXAFSPAK program, and neutron diffraction in ATOMS program.

	EXAFS analysis	**Neutron diffraction**
anneal: Mn-O	1.9840 Å± 0.0010	1.9547 Å±0.0001
pre: Mn-O	1.9907 Å ± 0.0006	1.9617 Å±0.0004
anneal: Mn-Mn	2.9001 Å ± 0.0009	2.9099 Å±0.0001
pre: Mn-Mn	2.9055 Å ± 0.0004	2.9150 Å± 0.0002

3.6 Reference

(1) Bartlett, B. M.; Hao, X. G.; Kuo, Y. T.; Clifford, B. P. *Abstr Pap Am Chem S* 2012, *243*.

(2) Xiang, H. F.; Zhang, X.; Jin, Q. Y.; Zhang, C. P.; Chen, C. H.; Ge, X. W. *J Power Sources* 2008, *183*, 355.

(3) Wu, H. M.; Belharouak, I.; Deng, H.; Abouimrane, A.; Sun, Y. K.; Amine, K. *J Electrochem Soc* 2009, *156*, A1047.

(4) Hassoun, J.; Panero, S.; Reale, P.; Scrosati, B. *Adv Mater* 2009, *21*, 4807.

(5) Maeda, Y.; Ariyoshi, K.; Kawai, T.; Sekiya, T.; Ohzuku, T. *J Ceram Soc Jpn* 2009, *117*, 1216.

(6) Hao, X. G.; Gourdon, O.; Liddle, B. J.; Bartlett, B. M. *J Mater Chem* 2012, *22*, 1578.

(7) Hao, X. G.; Austin, M. H.; Bartlett, B. M. *Dalton T* 2012, *41*, 8067.

(8) Weng, T. C.; Waldo, G. S.; Penner-Hahn, J. E. *J Synchrotron Radiat* 2005, *12*, 506.

(9) Ida, T.; Ando, M.; Toraya, H. *J Appl Crystallogr* 2000, *33*, 1311.

(10) Agarwal, S. B.; Wang, Y. F.; Clayton, C. R.; Herman, H.; Hirvonen, J. K. *Thin Solid Films* 1979, *63*, 19.

(11) Lytle, F. W.; Greegor, R. B.; Sandstrom, D. R.; Marques, E. C.; Wong, J.; Spiro, C. L.; Huffman, G. P.; Huggins, F. E. *Nucl Instrum Meth A* 1984, *226*, 542.

(12) Tyson, T. A.; Roe, A. L.; Hedman, B.; Frank, P.; Hodgson, K. O. *Physica B* 1989, *158*, 398.

(13) Westre, T. E.; Kennepohl, P.; DeWitt, J. G.; Hedman, B.; Hodgson, K. O.; Solomon, E. I. *J Am Chem Soc* 1997, *119*, 6297.

(14) Zabinsky, S. I.; Rehr, J. J.; Ankudinov, A.; Albers, R. C.; Eller, M. J. *Phys Rev B* 1995, *52*, 2995.

(15) Belli, M.; Scafati, A.; Bianconi, A.; Mobilio, S.; Palladino, L.; Reale, A.; Burattini, E. *Solid State Commun* 1980, *35*, 355.

(16) G.N., G.; I.J., P. 1993.

(17) Pennerhahn, J. E.; Fronko, R. M.; Pecoraro, V. L.; Yocum, C. F.; Betts, S. D.; Bowlby, N. R. *J Am Chem Soc* 1990, *112*, 2549.

(18) Manceau, A.; Gorshkov, A. I.; Drits, V. A. *Am Mineral* 1992, *77*, 1133.

(19) Thackeray, M. M.; David, W. I. F.; Bruce, P. G.; Goodenough, J. B. *Mater Res Bull* 1983, *18*, 461.

(20) Penner-Hahn, J. E. *Coordin Chem Rev* 1999, *192*, 1101.

CHAPTER IV

ELECTROCHEMICAL AND STRUCTURAL ANALYSIS of $Li_3V_2(PO_4)_3$

The work in this chapter is in preparation for publication:

Soojeong Kim, Zhengxi Zhang, Senlin Wang, Li Yang, James E Penner-Hahn, Aniruddha Deb " Electrochemical and Structural Investigation of the Mechanism of Irreversibility in $Li_3V_2(PO_4)_3$ Cathodes"

4.1. INTRODUCTION

Materials with a phosphate polyanion framework are considered to be good alternatives to oxide-based cathode materials in the lithium ion battery applications. Specifically, $LiMPO_4$ (M= Co, Mn, Ni, and Fe)[1-4] and $Li_3V_2(PO_4)_3$ (LVP)[5-7] have all shown considerable promise. Both systems contain redox active metals and mobile Li ions within a rigid phosphate frame, and both show good electrochemical capacities and stability. The monoclinic $Li_3V_2(PO_4)_3$ system and its doped variants show excellent promise as a high voltage cathode because of its high reversible capacity, high operating voltage (~4 V), good ion mobility, improved safety characteristic, low environmental impact.[6-9] All three lithium ions can be readily deintercalated giving a high theoretical capacity of 197 mA·h /g.[8-15] The electrochemistry reaction pathway of this cathode is

complex, showing a series of steps on charging, indicating phase behavior corresponding to loss of successive Li ions. In contrast, depending on the maximum charging voltages, the cathode can show no resolved transition or discharge, indicating solid solution on lithium reinsertion [8-15] In order to understand the functioning of LVP at the molecular level we have measured *in-situ* X-ray Absorption Spectroscopy (XAS) at a variety of rates and over a range of potentials. These data allow us to directly correlate average V oxidation states with electrochemical potential, and to characterize at the molecular level the mechanism for high-voltage inactivation.

4.2. EXPERIMENTAL

4.2.1. Preparation of $Li_3V_2(PO_4)_3$/C composites and electrode

The LVP composite electrodes were prepared using hexanedioic acid ($C_6H_{10}O_4$) as the chelating agent, where V_2O_5 and oxalic acid in stoichiometric ratio of 3:1 were dissolved in deionized water and then stirred at 70 °C. With the formation of a blue solution, a stoichiometric mixture of $NH_4H_2PO_4$, Li_2CO_3 and $C_6H_{10}O_4$ was added. This was followed by a 4 h stirring in an air oven at 100 °C, when a gel was formed. The gel was then heated to a temperature of 350 °C for 4 h, in the presence of a nitrogen atmosphere to allow NH_3 and H_2O to escape. Finally the resultant product was heated at 750 °C for another 4 h in the presence of nitrogen. All the reagents used in the experiment were analytical purity and purchased from Sinopharm Chemical Reagent Co., Ltd (SCRC), and used without further purification. For electrochemical and in-situ x-ray studies, composite electrodes were fabricated on an aluminium foil of thickness 25 μm by

the “doctor blade” technique with an electrode thickness of 100μ. The electrode was prepared using 80 wt% active materials, 10 wt% carbon (containing residue carbon in the synthesized active material and carbon black added in fabrication of the electrode), and 10 wt% polylvinylidene fluoride (PVdF) binder. The active material loading for the cathode was in the range of 5–6 mg X-ray powder diffraction (XRD) measurements were conducted by a Rigaku D/max-2200/PC diffractometer. The morphology was analyzed by field emitting scanning electron microscopy (FE-SEM, JEOL JSM-7401F) and transmission electron microscopy (TEM, JEOL JEM-2010). The composite was synthesized by Prof. Yang’s group in Shanghai Jiao Tong University, in Shanghai, China, and the synthetic method was discussed at the paper published from Prof. Yang’s group. [16]

4.2.2. Electrochemistry experiment for $Li_3V_2(PO_4)_3/C$

The charge/discharge cycling was performed continuously at room temperature at the DND-CAT beam line (sector 5), at the Advanced Photon Source, Argonne National Laboratory, with a potentiostat/galvanostat system (Princeton Applied Research, Model Versa) under constant current control. Charging and discharging were performed at a constant current 0.1C (1 C=197 mAh/g) at different cut-off voltages such as 3.0 $\rightleftharpoons$ 4.5 V, 3.0 $\rightleftharpoons$ 4.8 V as shown in **Figure 4.1**.

4.2.3. *In-situ* XAS experiment

The *in-situ* electrochemical reaction cell was assembled in an argon-filled glove box. The glass wool separator was punched to give a disk with an outer diameter of 20 mm and inner diameter of 6mm. The separator was placed on top of the electrode $Li_3V_2(PO_4)_3/C$ soaked in 1 M $LiPF_6$ electrolyte, dissolved in 50 wt % ethylene carbonate (EC) and 50 wt % dimethylcarbonate (DMC) obtained as a solution from BASF. Finally, a lithium foil counter-electrode was punched to give a disk with an outer diameter of 14 mm and an inner diameter of 8 mm and placed on top of the separator which was soaked with electrolyte. Kapton film (25.4 µm thickness) was utilized as the X-ray window for this *in-situ* electrochemical reaction cell. More detailed information on the design of this reaction cell can be found in Deb et al.[17]

For the XAS measurements, cycling of the electrochemical reaction cell was done continuously using a Princeton Applied Research VERSASTAT potentiostat, while the XAS data was collected at the same time. The given capacity values were not measured values but were calculated based on the duration of each scan. For example, one XAS scan takes 0.65 h, current is 0.02828 mA, and mass is 0.00202 g. Therefore, the capacity (mAh/g) turns out to be 9.1 mAh/g. And, given capacity values are at the end of each individual scan. Since this experiment is *in-situ* work, XAS was stopped when the electrochemistry reached a certain potential (cut off voltages). Therefore, some of the last scans can be incomplete and are not included in the data set. For example, when electrochemistry stops at 4.5V, the last scan does not include information of 4.5V. The XAS recorded under two different rates and two different cut-off voltages are shown in **Figures 4.2 - 4.5**, while the model compounds are shown in **Figure 4.13**. In **Figure 4.13**, three model compounds, LVP (V^{3+}), VO_2 (V^{4+}), and V_2O_5 (V^{5+}) were

measured as XANES references. Valence calculations were done based on three model compounds at 0.75 intensity which leads one to the conclusion that 1 valence= 1.85 eV on average.

In-situ XAS measurements were performed in transmission mode at the bending magnet beam line station D of the DND-CAT (Sector 5), at the Advanced Photon Source, using a water-cooled Si(111) double crystal monochromator. The energy resolution of the monochromatic beam was ~1.0 eV. A beam size of about 0.3×4 mm^2 was used for the beam to pass easily through the *in situ* cell X-ray window resulting in an incident photon flux of ~10^{10} photons/s. X-ray flux before and after the electrode was a measured using N_2 filled ion chamber. A V foil reference and a third ion chamber were placed behind the sample in order to provide an internal energy reference, with the first inflection point of the V- foil defined as 5465 eV. For the V K absorption edge the monochromator was scanned from 200 eV below to 800 eV above the edge. Scans (using 5 eV steps in the pre-edge region, 0.5 eV steps in the near-edge region and 0.05 $Å^{-1}$ steps in the EXAFS region) were taken. The data were integrated for 1 s per step in the pre-edge, 1.5 s per step in the near edge region and 1.5 – 25 s per step in the EXAFS region for a total scan time of about 40 min. The scans were made continuously during charge and discharge; and, once the potential reached a cut off voltage (3.0 V, 4.5 V or 4.8 V), the electrochemistry was stopped for 45 min and additional XANES spectra were measured. While measuring the extra XANES, there was no current flowing, thus those extra XANES were expected to be on top of each other. When plotting these, there were no main edge shifts which are reasonable, but when the pre-edge

region was checked, it seemed that the intensity increased between the end of 3rd charge cycle and the start of 4th cycle, which follows the idea of relaxation.

The XANES data shown here were analyzed using the MBACK program,[18] and the EXAFS data presented were analyzed using a combination of EXAFSPAK software package[19] and ATHENA from IFEFFIT package.[20] The raw data was first imported in ATHENA and then exported as a text format and then this data was imported back in EXAFSPAK to do the EXAFS analysis using FEFF9 [21] to calculate *ab initio* phase and amplitude parameters. The resulting $\chi(k)$ function was weighted with k^3 to account for the damping of oscillations with increasing k. The radial structure functions presented here were obtained by Fourier transformation of $k^3\chi(k)$ using a k range of 1.5 – 11.5Å^{-1}. A pre-edge background and a cubic spline EXAFS background were subtracted and the EXAFS oscillations were normalized to the appropriate Victorian function modeling the absorption decrease above the edge.[22]

4.2.4. Principal Component Analysis (PCA) Method

4.2.4.1. Concept of PCA method

The interpretation of XAS data can be challenging since XAS is a bulk technique that provides information only about the average structure. If a sample contains multiple components, it can be difficult or impossible to assign structural features to individual components. For systems with a systematic variation with relative concentration of each component, the principal component analysis (PCA) method can significantly simplify interpretation of the data. PCA is an analytical approach that allows a set of spectra to be represented by a few dominant spectra.

More importantly, PCA can be used to estimate the number of components in an unknown mixture.[23] Since the component spectra is the linear square fit of the known species present in the actual system, it provides a better idea what kind of components are present in the unknown mixture.[24-27]

The PCA method has been used extensively for the analysis of many types of spectra, including MS, IR, and UV-VIS.[25,27-29] It has found some application in XAS studies.[27,30-34] One challenge in using PCA to determine the number of components in a mixture is that any difference between samples can give rise to spurious components. One of the problems with PCA is that any change in sample thickness or condition has to be re-measured. The present study is ideally suited to PCA since the sample condition and preparation are completely identical. One key goal of using PCA is to determine unambiguous components that are needed to reproduce the variability in the experimental spectra.[25,28,35] The main function of PCA is to reduce the dimension of a dataset by approximating the spectra with a weighted sum of orthogonal eigenvectors. The overall procedure is as follows: first, abstract eigenvectors were derived from the set of XAS spectra by principal component analysis. These eigenvectors were used to estimate the number of species present: second, a varimax rotation was applied to get qualitative concentrations of the factors; and third, additional information was used to derive real concentrations and real factors such as the XAS spectra of the pure species, whose relative contributions can be obtained through the process of Iterative Target Factor Analysis (ITFA).[36] In the factor analysis, factors are representing the spectral components. If the amplitude of the factor's spectra are linearly dependent on the concentration of corresponding pure species, the

measured spectra $\mathbf{d}_k$ are the sum of the product terms of the *n* linear independent factors $\mathbf{r}_j$. Their concentration distributions c_{jk} are shown below in **Eq. 4.1**: [27]

$\mathbf{d}_k = \sum_{j=1}^{n} r_j c_{jk,}$ with *k* = 1,..., c (number of samples), value of c > n. **…….….Eq. 4.1**

D = RC……. Eq. 4.2

$\mathbf{d}_k$: measured spectra, collected in the r×c data matrix **D**, with c spectra in the columns at r measuring points.

R: r×n matrix, containing the spectra of the factors in the columns

C: n×c matrix, containing the corresponding relative concentrations of the factors

If only the experimental spectra, which are collected in the data matrix **D**, are known, the first step of the analysis is to determine the rank of **D**. It equals the number of linearly independent spectral components in the measured system. The number of the linear independent factors in the data can be determined by using eigenvalues and the semi-empirical indicator function ***IND***.

$\boldsymbol{IND_n} = R\,E_n/(c\text{-}n)^2$ **……** with *n=1……c-1***……...……..Eq. 4.3**

when the **IND** function reaches its minimum value, then the number of primary factors n can be obtained. As soon as the correct number for n is determined, the experimental error in the data can be calculated with the real error function $R\,E_n$.[27,36] An alternative name for the Real Error (***RE***) is the ***RSD*** (used by Malinowski). The ***RSD*** is defined in **Eq.4.4**:

$\boldsymbol{RSD_n} = \left(\frac{\sum_{j=n+1}^{c} \lambda j}{r(c-n)}\right)^{1/2}$ **……** with *n=1……c-1***……...Eq.4.4**

where λ_j is the j^{th} largest eigenvalue, n is the number of abstract factors (number of components we need) used to reproduce the data, and c spectra with r channels are used to construct the data matrix. $\boldsymbol{RSD_n}$ must be compared against the estimated experimental error. [27,36]

4.2.4.2. PCA into Vanadium XAS

PCA was performed separately on the data for each cycle. For each cycle, all of the XANES spectra collected during charge and discharge were used to find how many components were necessary to explain the variability for that cycle. For the PCA analysis we utilized the software code PRESTOPRONTO.[37] The XANES scans for a single charge/discharge cycle were imported for PCA analysis over the energy range of 5455-5525 eV. As discussed earlier, the eigenvectors were used to estimate the number of vanadium species present, for each cycle.[37]. In addition, the number of components was chosen carefully, as shown by the RSD (Residual Standard Deviation) plot in **Figure 4.7**. It shows that the number where the arrow indicates the minimum RSD value, meaning that the indicated number is the minimum number of abstract factors used to reproduce the data.

As discussed previously, the ITFA method was used to align theoretical components obtained from PCA analysis to the real experimental XANES. The reconstruction of the experimental spectra by ITFA is seen in **Figure 4.12**. Here the reconstructed components (C1, C2 and C3) are shown for two different cut-off voltages and under two different rates (0.1C and 0.2C). PCA were performed 4 times individually based on each cycle (**A**-**D**). Therefore, as shown in **Figure 4.12**, there are 4 different sets of components. The variations between C1 from cycle **A** and cycle **B** are due to the fact that the starting point of charge between cycle **A** and cycle **B** is different. This difference comes from the capacity loss happening in cycle **A**. so, the starting point for Cycle **B** is more right shifted than the one for cycle **A**.

Since XAS technique can be used in the mixture of unknown samples, the spectra interpretation from those samples is often unspecific and complex, particularly if proper model systems are not available or if the samples get changed by certain chemical reactions and no longer stays as the parent sample. Then it is difficult to understand the spectra specifically. To overcome this difficulty, PCA method has been applied on the measured XANES spectra (for each cycle) [23] to determine the number of principal components in the LVP system while cycling. PCA technique was used to examine in real time the evolution of the different species (or components) of V while LVP was changing between $Li_3V_2(PO_4)_3$, $LiV_2(PO_4)_3$, and $V_2(PO_4)_3$, under cycling. A well-known difficulty with PCA is that, while it is useful for determining the number of components, determining the spectra for these components typically requires additional information. The calculated spectra for Components 1 and 2 are similar to authentic spectra for V^{3+} and V^{4+}.

4.2.5 Least Squares Fitting

Once the PCA components were obtained by ITFA (shown in **Figure 4.12**), these were used to do a least squares fit of the experimental XANES measured at each state of charge, to find the fractional composition of each component, allowing the determination of the apparent fractional composition of the sample in terms of each component. The results of these fits are shown in **Figures 4.8 - 4.9 and Figures 4.10 - 4.11**. The ITFA components are not really useful in a practical sense because what they represent is not known. Therefore, the V model compounds were used as reference spectra and fitted with experimental XANES in order to give qualitative information. Since the structure of the model compounds were not the same as

$Li_3V_2(PO_4)_3$, the model compounds were not ideal but allowed the calculation of oxidation changes that happened during cycling. Once the number of principal components present in each cycle is known, model V^{3+} and V^{4+} were chosen as the two components for the 3.0 - 4.5 V cut-off (for both the rates 0.1C and 0.2C), while for the 3.0-4.8V cut-off three models V^{3+}, V^{4+} and V^{5+} were chosen.as the three components, for the least squares to fit the experimental XANES spectra. Least square fitting using the authentic V^{3+} and V^{4+} reference spectra (see **Figure 4.13**) gave equivalent results, but allowed an estimate of the average oxidation state. This enabled us to track the charge compensation taking place *in-situ*. The results are shown in **Figures 4.8 - 4.9 and Figures 4.10 - 4.11**. The least squares fitting of the PCA components and the model compounds were performed with the program suite "SixPack" from IFEFFIT package. [20]

4.3. RESULTS

4.3.1 Electrochemical Characterization

The *in-situ* XAS results verify the vanadium conversion between V^{3+}/V^{4+} and V^{4+}/V^{5+} redox couples during charge/discharge cycling. The electrochemical data for all the *in-situ* is shown in **Figure 4.1**. These observations were essentially identical to those seen previously. [12,16,38-48] confirming that our cell does not interfere with electrochemical cycling of LVP. When LVP is cycled between 3.0 $\rightleftharpoons$ 4.5 V (traces **A** and **B** in **Figure 4.1**) there are three distinct plateaus at ~3.6 V, 3.7 V and 4.1 V, (*vs.* Li/Li^+). These have previously been attributed to oxidation from V^{3+} to $V^{3.25+}$, from $V^{3.25+}$ to $V^{3.5+}$, and from $V^{3.5+}$ to V^{4+}, respectively.[12,16,38-48] The three plateaus are proposed as the two-phase transition (of $Li_3V_2(PO_4)_3$ and $LiV_2(PO_4)_3$)

processes during the electrochemical reactions between 3.0 - 4.5 V.[8,49-51] The first cycle **A** shows significant hysteresis (~25 mAh/g) and even larger capacity loss (~40 mAh/g). The second cycle **B** at higher rate shows similar behavior, with modest capacity recovery on the charge cycle and somewhat smaller capacity loss on the discharge cycle. As long as the voltage is limited to 4.5 V, well defined thresholds are seen on both charge and discharge demonstrating electrochemical reversibility. However, when the electrode is cycled above 4.5 V (**C** and **D**) no plateaus are observed on discharge. Intriguingly, the electrode appears to recover somewhat on sitting at 2.0 V, since 4 plateaus are observed on charge cycle **D**. It means that cycle **C** process is reversible showing that the framework structure is essentially preserved throughout. Because re-extraction of Li in the cycle D, two phase behavior is evident.[52]

4.3.2 XANES of Charge/Discharge

The XANES spectra for all four cycles are shown in **Figures 4.2 - 4.5**. In each case, there is a significant shift in the edge to higher energy during charge and a shift back to lower energy during discharge, consistent with formation of V^{4+} and re-reduction to V^{3+}. The isolated 1s → 3d transitions for the spectra in **Figures 4.2 - 4.5** are shown in **Figure 4.6**. As with the edge energy, the 1s → 3d transition shifts to higher energy and lower energy on discharge. There is no change in the intensity of the 1s → 3d transition during cycle **A**. As discussed in Chapter I, this provides direct evidence that the vanadium remains in an approximately octahedral environment during electrochemical cycling. In sharp contrast, the 1s → 3d intensity more than doubles when the

potential is raised to 4.8 V, and this increase is not reversed during the reductive half of the cycle. This increase in 1s → 3d intensity is consistent with a distorted V environment.

4.3.3 Principal Component Analysis

XAS is a bulk method, giving the average spectrum for a mixture that could, in principle, contain many different components. To analyze the data, we first used PCA[23] to determine the number of unique components that were required to account for the observed data. For both cycles **A** and **B**, only two components are necessary to fit the data; for cycles **C** and **D** a third component is required. In **Figure 4.7**, the Residual Standard Deviation (RSD) plot showing the maximum number of principal components needed in the PCA analysis for the four cycles. This supports the qualitative conclusion above that when the potential is raised above 4.5 V the cathode suffers some sort of irreversible change, resulting in formation of a third component.

We used Iterative Target Factor Analysis (ITFA),[36,53] with the assumption that the components vary monotonically with voltage to estimate the true component spectra. Using these calculated components to fit the measured spectra, we obtain the apparent compositions shown in **Figure 4.8**(a). Component 1 starts at ~100% and remains largely unchanged until ~50 mAh/g, at which point Component 1 decreases with a corresponding increase in Component 2 until ~100 mAh/g, at which point the conversion largely stops, with further conversion to pure Component 2 not happening until the beginning of the reductive half (during discharge) of the cycle.

Least square fitting using the authentic V^{3+} and V^{4+} reference spectra (see **Figure 4.13**) gave equivalent results, but allow an estimate of the average oxidation state. Not surprisingly, the

starting state is consistent with ~100% V^{3+}. This remains the case until ~50 mAh/g, at which point V^{3+} is converted to V^{4+}, with about~75% of the V having been oxidized by 100 mAh/g. This percentage does not change significantly during the 4.0 V plateau. It is only after the sample has been equilibrated for ~ 1 h at 4.5 V that the V is fully oxidized to $V^{4+}$and the final state (at the start of the reductive or discharge cycle) is consistent with ~100% V^{4+} (see **Figure 4.8**(a))). The calculated average V oxidation states at the start and end of each charge and discharge cycle are tabulated in **Table 4.1**.

In addition to these quantitative approaches to the data, we also explored two phenomenological comparisons. The total change in edge energy (judged as the energy at absorbance of 650 cm^2/g is 1.74 eV (for charge), 1.26 eV (for discharge) in cycle **A**. From this, we can calculate the fractional change in edge energy for each successive scan. Similarly, the total change in average V-O bond length is 0.049 Å for charge (0.048 Å for discharge), allowing us to calculate the fractional change in bond-length for each successive scan. These model-independent phenomenological approaches are also shown in **Figures 4.8 - 4.9**, and give essentially identical results to the quantitative fits, with two obvious plateaus during charging but generally much more continuous variation in composition during discharge. In contrast to the obvious plateaus that are seen on charging, the apparent composition during discharge varies much more uniformly with capacity.

Similar results are found for cycle **B**-**D** (in **Figure 4.9** (c), **Figure 4.10**, and **Figure 4.11** (f)). The increase in rate from 0.1 C to 0.2 C does not cause any significant changes in the calculated composition profiles, although the starting composition for B is more oxidized than for A, consistent with the capacity loss. Although there are fewer points at 0.2 C the results are

the same: two plateaus on charging and little or no plateaus on discharges. In both cases, there is little change in V structure during charging until the potential exceeds ~3.9 V and then there is significant change, consistent with partial oxidation of the V^{3+} to V^{4+}. The full oxidation to V^{4+} does not take place, however, until the potential reaches ~4.5 V.

Above 4.5 V (cycles **C** and **D**) the behavior is similar, although in this case a third species is formed where the potential exceed ~4.5 V. With three species present, the fitting is significantly more sensitive to minor variations in the model spectra and consequently, the calculated percentage composition is less reliable. However, even from the phenomenological comparisons of edge energy and bond length, it is apparent the reductions from 4.8 V seem to show even more gradual changes in vanadium environment, without the abrupt changes in average composition that were seen during charging that during discharging there are significant plateaus during which there is little or no changes in the vanadium, despite the flow of current, and that the rate of changes in the average vanadium accelerates when the potential exceeds ~ 3.9 V and again when it exceeds ~ 4.5 V. In addition, cycle **B** and **D** have half as many data points than cycle **A** and **C**, since they have twice the charge/discharge rate.

After the end of each charge and discharge cycle, the electrochemical reaction cell was allowed to equilibrate for ~150 minutes in order to investigate if there is any change happening in the electrode even though the current is not flowing through the cell. **Figures 4.8**(b) and **4.10**(e) show the apparent composition, calculated in the same way as for **Figs. 4.8**(a) and **4.10**(a), with time=0 defined as the last composition point for components 1 and 2 at the end of the charge or the discharge cycle. During the relaxation time the vanadium environment continued to change. For cycle **A**, the change was mostly complete after 40 minutes, with only

small additional change after this for either charge or discharge. In contrast, for cycle **B** all of the relaxation is complete within 40 minutes on charge but requires at least 100 minutes to equilibrate during discharge.

4.3.4 EXAFS for four cycles (A, B, C, and D)

The result of the outer shell changes shown in cycle **C** and **D** compared to those in cycle **A** and **B** (see **Figures 4.16** and **4.17)** varies a lot. The significant outer shell changes shown in the Fourier transform of the EXAFS data in **Figures 4.16** and **4.17** with two different cut offs (cycle **A**, **B**: as 3.0 ⇌ 4.5 V vs cycle **C**, **D**: as 3.0 ⇌ 4.8 V) can then be ascribed to the some fraction of V atoms to other sites. Perhaps empty tetrahedral Li sites which would be significantly more disordered than the structure without facing any anti-site mixing. And this also relates to the intensity change happening in the 1s → 3d region in the XANES plot for cycle C and D in the Figure 4.6 ((e), (f), (g), and (h)).

The EXAFS data give a similar picture. In all cases(see **Figures 4.16 - 4.17**) samples show the expected V-O nearest neighbors, together with V⋯P and V⋯V outer shell scattering. There are significantly reversible changes in the average V-O nearest neighbor distance (see **Table 4.2**) consistent with oxidation and reduction of the V ions. When the potential reaches 4.8 V, the pre-edge intensity shows a significant increase compared to that of 3.0 ⇌ 4.5 V cycling, as shown in **Figure 4.6**. Therefore, by comparing pre-edge intensity at 4.8 V with the intensity of the T_d V^{5+} model compound, it is possible to calculate the V migration into the tetrahedral site. During cycle **C**, 23 % of the O_h V migrated to empty T_d Li sites and during cycle **D**, 16 % of the

O_h V migrated to empty T_d Li sites. This estimate is just an estimate not a quantitatively reasonable value.

4.4 DISCUSSION

The monoclinic (space group $P2_1/n$) structure for LVP has distorted VO_6 octahedra and PO_4 tetrahedra sharing oxygen vertexes, and the XANES spectra for cycles **A** and **B** are consistent with this structure. In contrast, there is a dramatic increase in 1s → 3d intensity when the potential exceeds 4.5V. Two possibilities exist that could account for the increased intensity. It is known that strongly covalent vanadyl-like species exhibit on extremely intense 1s → 3d transition. Formation of such a species, however, would require decomposition of the phosphate backbone, since there is no other oxygen source. A simpler explanation for the increase in intensity is a change in V geometry. Thus, it is known that tetrahedral metal sites have significantly more intense 1s → 3d transitions due to the possibility of d+p orbital mixing in non-centrosymmetric environments as discussed in Chapter I. In the present case, this could happen with anti-site mixing, in which a portion of the V migrates to Li(3) sites within the three Li sites(tetrahedral (Li(1)) and five-coordinate (Li(2) and Li(3))).[54] The observation that this putative migration only occurs above 4.5 V is consistent with the model in which it is only at these voltages that the Li sites are vacant and that the smaller V^{5+} cation is formed. Without knowing the details of the V site, it is impossible to estimate the fraction of anti-site mixing. However, if the migrated V had a spectrum similar to V in VO_2 (see **Figure 4.13**), it is possible that as little as 10 % of the V could be present in the Li site.

Perhaps the most surprising observation is that well defined electrochemical transitions are not well correlated with bulk V oxidation state. We attribute this to slow lithium/electron transfer kinetics in individual $Li_3V_2(PO_4)_3$ particles. The plateaus at 3.6 and 3.7 V, previously attributed to $V^{3+} \rightleftharpoons V^{3.25+}$ and $V^{3.25+} \rightleftharpoons V^{3.5+}$, respectively, are seen to correspond to only a small change in average V oxidation state, while by the start of the 4.0 V plateau, attributed to $V^{3.5+} \rightleftharpoons V^{4+}$, a significant fraction of the V has been oxidized, although little further oxidation occurs during the plateau. We interpret this as evidence that the electrochemical measurements reflect only the state of the V ions on the surface of the $Li_3V_2(PO_4)_3$ particles while XAS is sensitive to all of the V in the sample. These data thus imply that an important limitation in $Li_3V_2(PO_4)_3$ batteries will be the rate of lithium (and perhaps electron) transfer from bulk to surface. Another interesting point that we observed is that we see plateaus on charging, not for discharge. This can be as attributed to the charge ordering effect,[8,9] that is, when Li is intercalated, there is not as much kinetic limitation, which would be consistent with the disappearance of charge ordering effect on discharge.

An interesting corollary of these results is that they suggest an alternative explanation for the observed hysteresis. Earlier work, using chemically-prepared $Li_xV_2(PO_4)_3$ (x=0,1,2,3) had attributed the hysteresis to the presence of oxidation state ordering.[8] Our data suggests a simpler explanation, at least for our measurements. Based on our XAS data, the V is not fully oxidized by the end of the oxidative half of the cycle. It is only after the cathode has been allowed to equilibrate at 4.5 V for ~ 1 h that we see full formation of V^{4+}. The same thing happens at low voltage. The average V oxidation state (as determined from XANES fits, see **Table 4.1**) is 3.58 at

the end of the first discharge but 3.28 at the start of the second charge. The apparent hysteresis in our measurements is thus the result of equilibration of the bulk material with the surface, such that the electrochemically active surface sites are different at the start of the reductive cycle than they were at the end of the oxidative cycle.

The information from XAS can be combined with the electrochemistry utilizing Faraday's law (**Figures 4.14-4.15**) to provide additional insight. Using Faraday's law, the theoretical capacity of $Li_3V_2(PO_4)_3$ is 197 mAh/g for V^{3+} being converted to $V^{4.5+}$. So theoretically for the average valence change of V ($V^{3+} – V^{4+}$, $V^{4+} – V^{4.5+}$), in this compound, the capacity used for a V valence change of one will be a 0.67 times the total theoretical capacity, i.e.,131.33 mAh/g. Hence utilizing the experimentally measured capacity at each state of charge in the cycling process and the theoretical capacity, we can represent the average valence change of V during the cycling:

$$V_{Val,Change} = \left[\frac{Experimental\ Measured\ Capacity\ (mAh/g)}{131.33\ mAh/g}\right] \quad \textbf{Eq. 4.5}$$

We can then compare the results from the Faraday's law calculation with that obtained from the XAS results (**Figures 4.14 - 4.15**).

4.5 CONCLUSION

Monoclinic $Li_3V_2(PO_4)_3$ has emerged as one of the most promising phosphate candidates for the cathode in lithium-ion batteries. We have used *in-situ* X-ray Absorption Spectroscopy to

characterize the evolution of the vanadium as a $Li_3V_2(PO_4)_3$ cathode is cycled electrochemically. These data demonstrate the presence of significant kinetic effects such that the measured electrochemical behavior does not represent the bulk vanadium. When the battery is cycled between 3.0 and 4.5 V, there are two distinct vanadium species which we attribute to octahedral V^{3+} and V^{4+}. When the voltage is raised above 4.5 V, the third species is observed, consistent with formation of V^{5+}. Based on the 1s → 3d intensity, we suggest that at least a portion of the V^{5+} migrates to the (new empty, Li(3)) Li sites giving a tetrahedral V. This lithium-vanadium anti-site mixing may be responsible for some of the electrochemical irreversibility that is seen above 4.5 V.

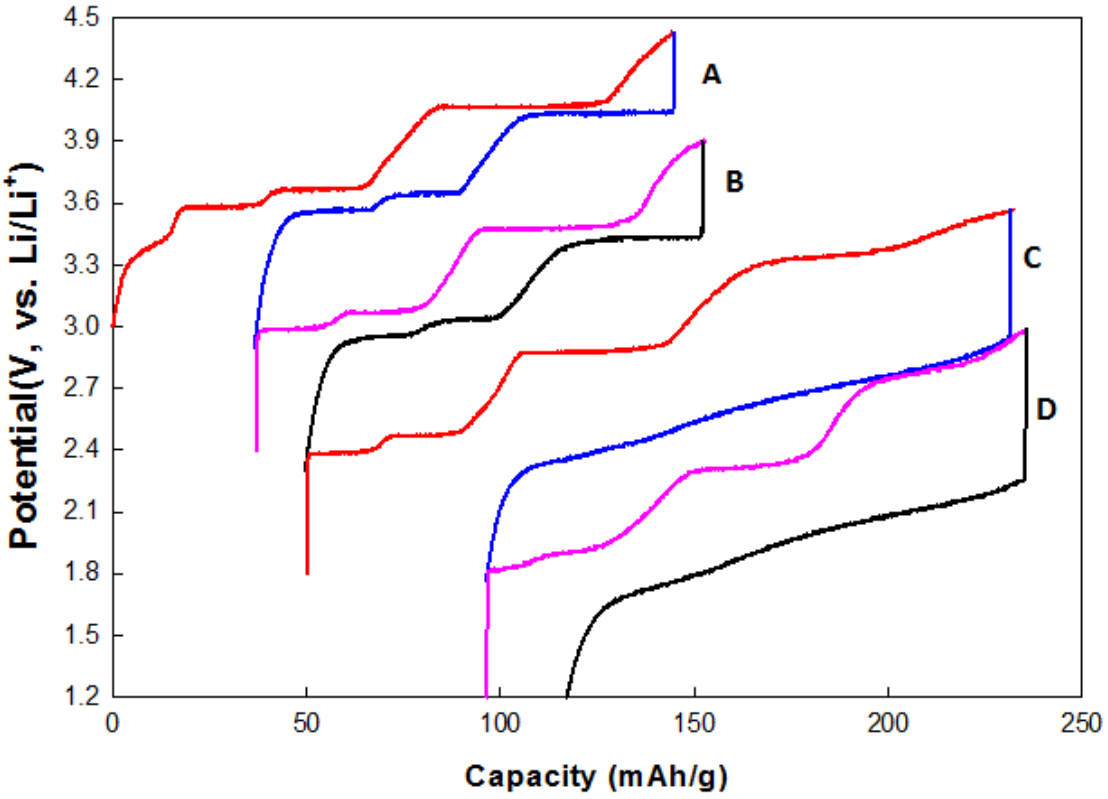

Figure 4.1 Charge-discharge profiles for $Li_3V_2(PO_4)_3$ at 0.1 C (**A** and **C**) and 0.2 C (**B** and **D**). **A** & **B** are from 3.0 ⇌ 4.5 V; **C** & **D** from 3.0 ⇌ 4.8 V. Successive cycles are offset vertically by 0.6 V for clarity.

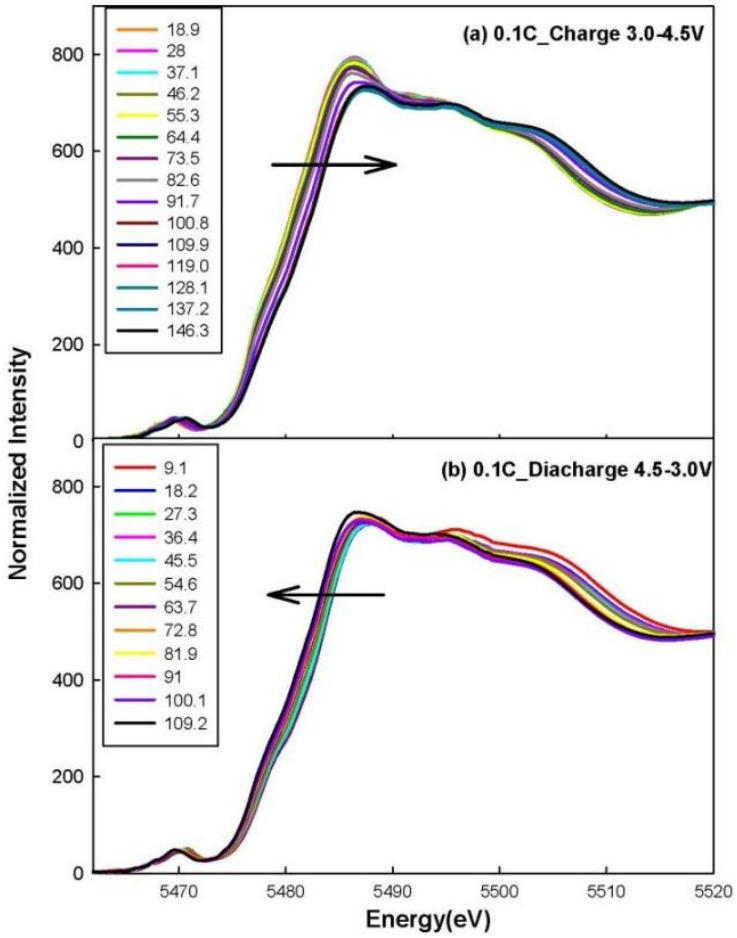

Figure 4.2 *In-situ* V-K edge XANES during charge/discharge cycling, **Cycle A** (3.0 ⇌ 4.5 V) (a) 0.1C charge, (b) 0.1C discharge

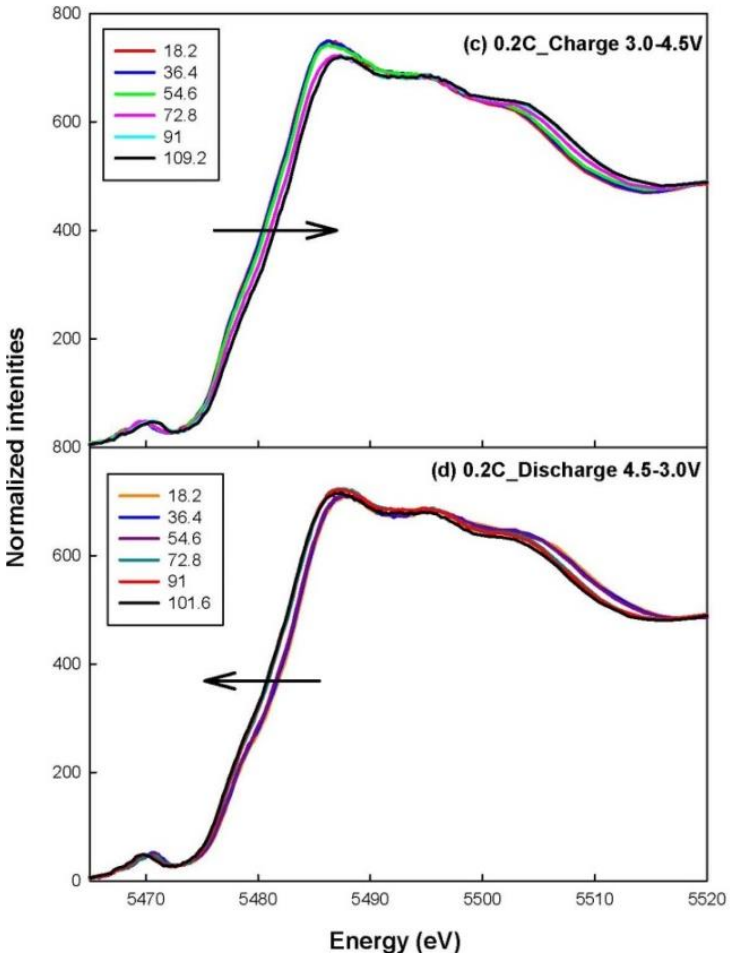

Figure 4.3 *In-situ* V-K edge XANES during charge/discharge cycling, **Cycle B** (3.0 ⇌ 4.5 V) (c) 0.2C charge, (d) 0.2C discharge

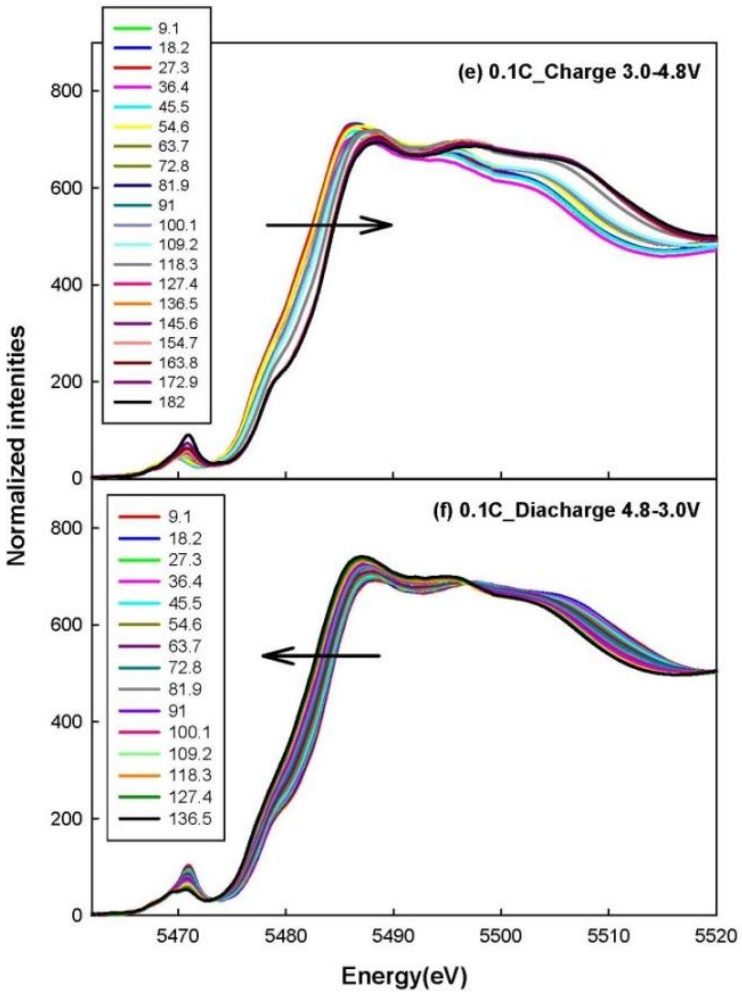

Figure 4.4 *In-situ* V-K edge XANES during charge/discharge cycling, **Cycle C** (3.0 ⇌ 4.8 V) . (e) 0.1C charge, (f) 0.1C discharge

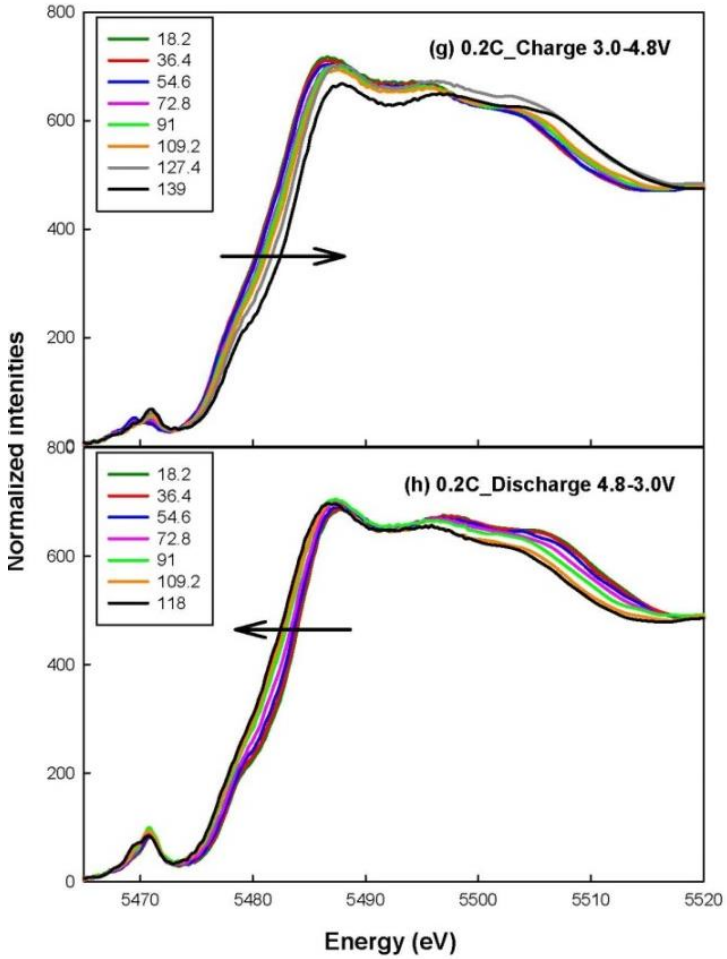

Figure 4.5 *In-situ* V-K edge XANES during charge/discharge cycling, **Cycle D** (3.0 ⇌ 4.8 V) (g) 0.2C charge, (h) 0.2C discharge

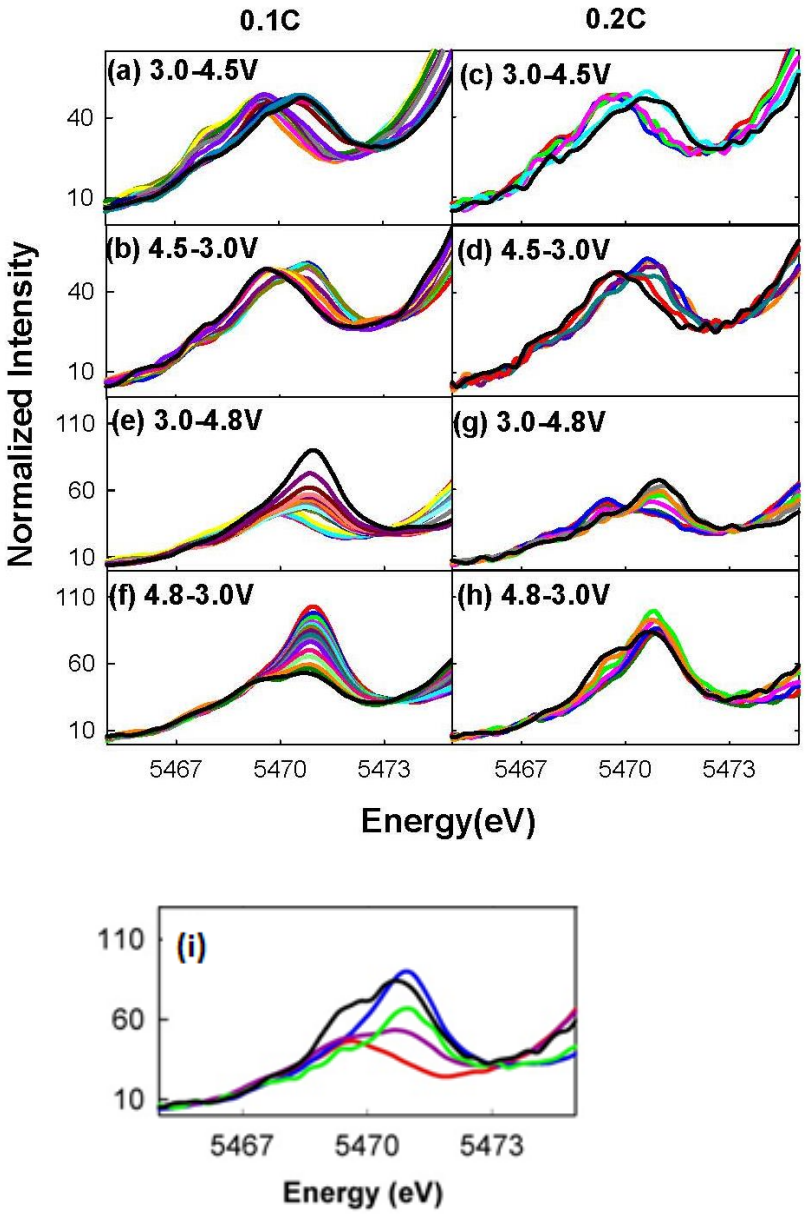

Figure 4.6 (a)-(h)Expanded 1s → 3d transitions for the data in **Figures 4.2-4.5** (*In-situ* V-K pre-edge XANES observed for 0.1C (**Cycle A,C)** and 0.2C (**Cycle B,D)** cycling); (i) expanded 1s → 3d transitions for cycles **C** and **D**: 3.0 V at the start of **C** (red); 4.8 V at the end of the charge cycle for **C** (blue) and **D** (green); 3.0 V at the end of the discharge cycle for **C** (purple) and **D** (black).

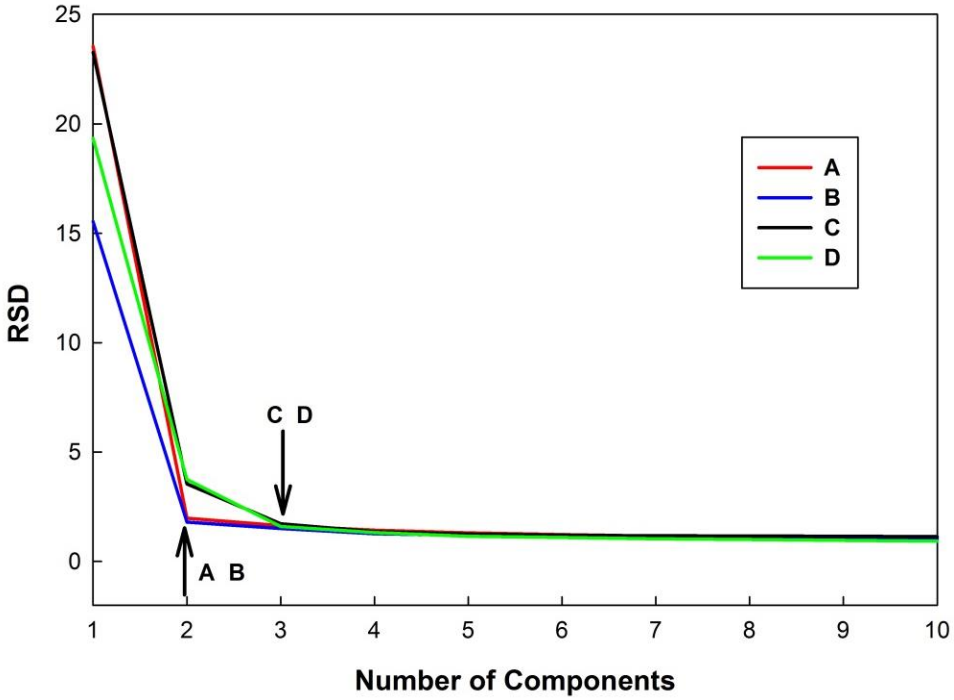

Figure 4.7 The Residual Standard Deviation (RSD) plot showing the maximum number of principal components needed in the PCA analysis for the four cycles. The arrows show that for the cycles **A**, **B** two components are needed, while for cycles **C**, **D** three components are necessary.

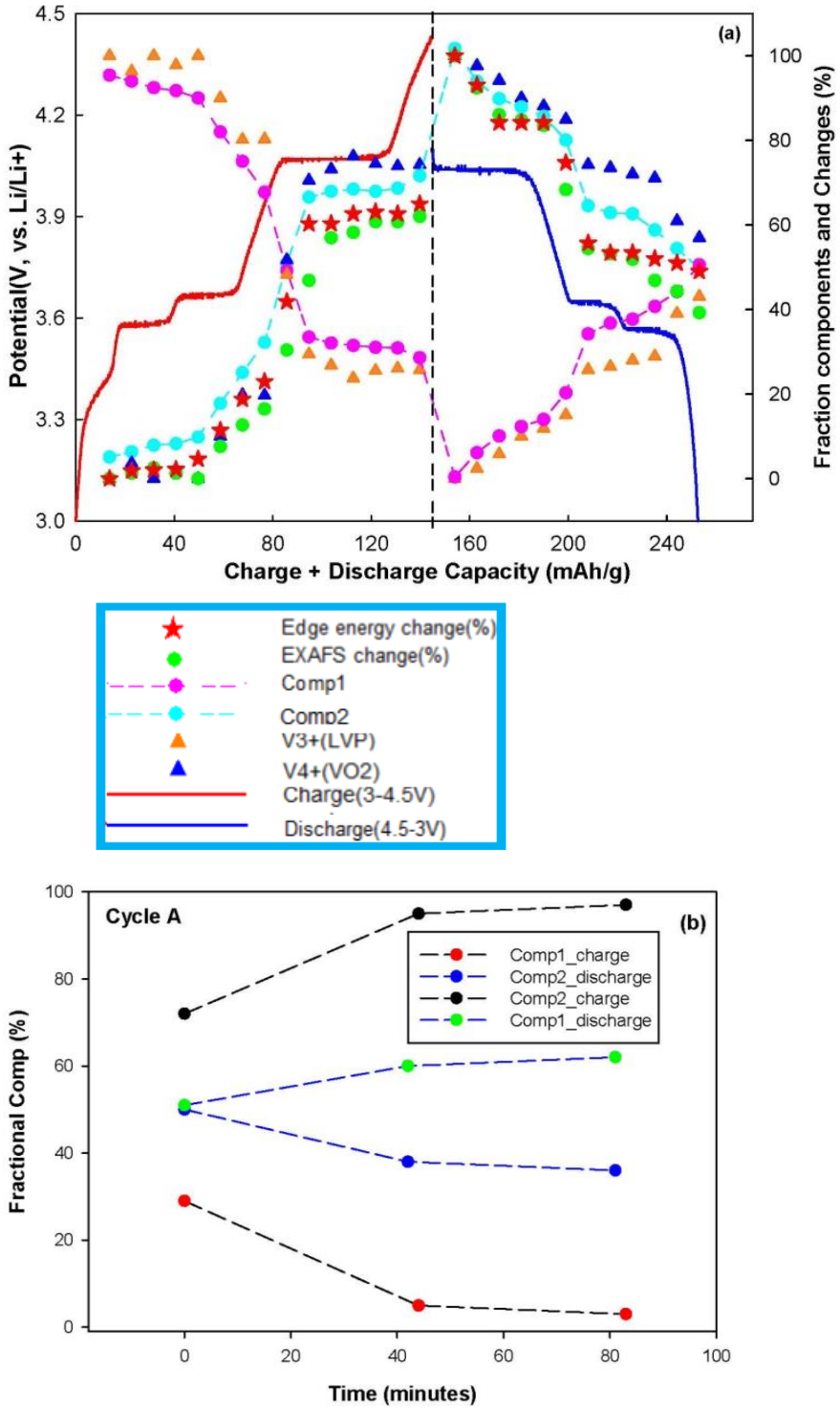

Figure 4.8 0.1C rate charge/discharge profile while cycling, cycle **A** (a) PCA & Model fit, (b) results for extra XANES spectra measured during equilibration time.

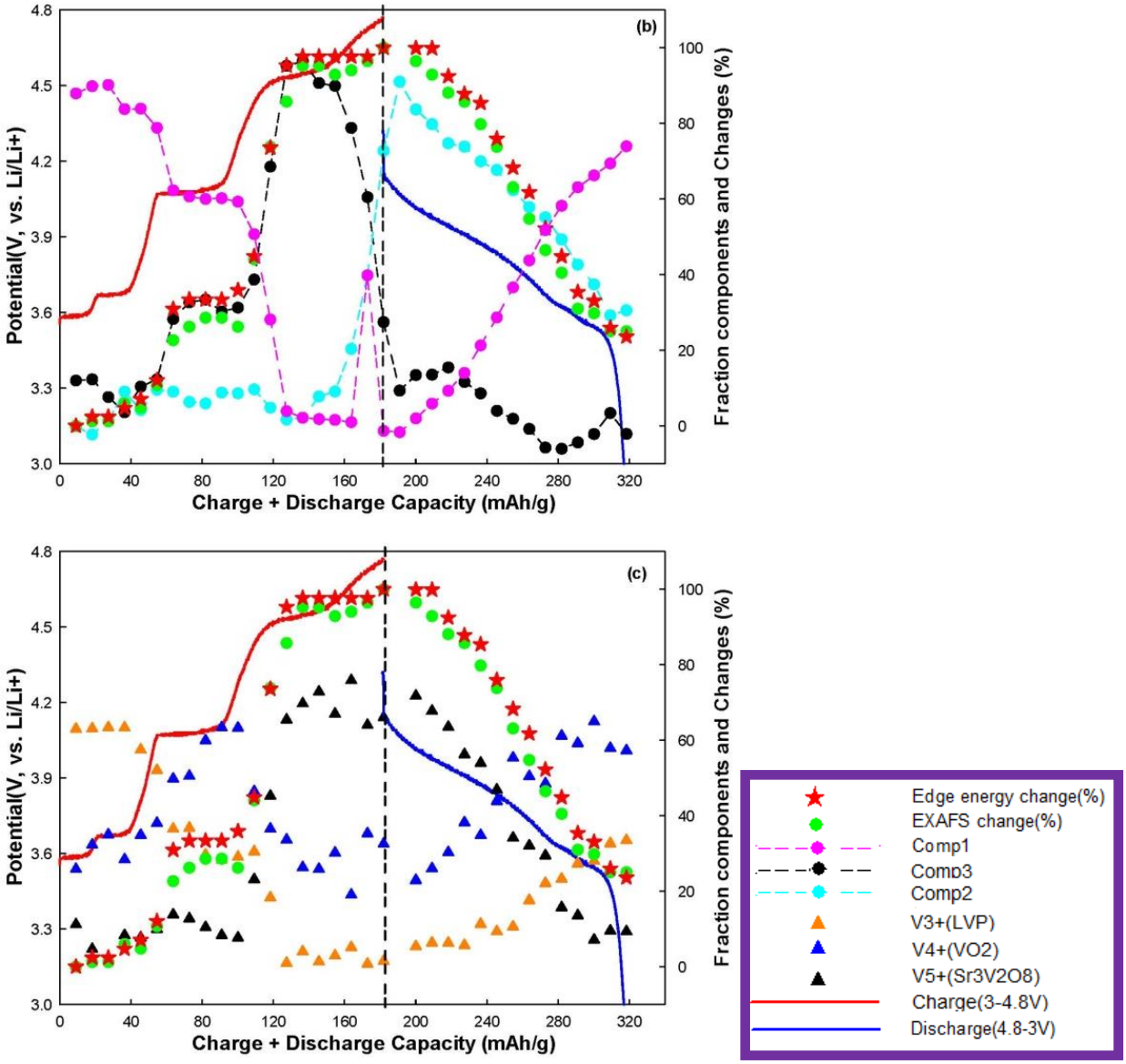

Figure 4.9 0.1C rate charge/discharge profile while cycling, cycle **C** (b) PCA fit (c) Model fit

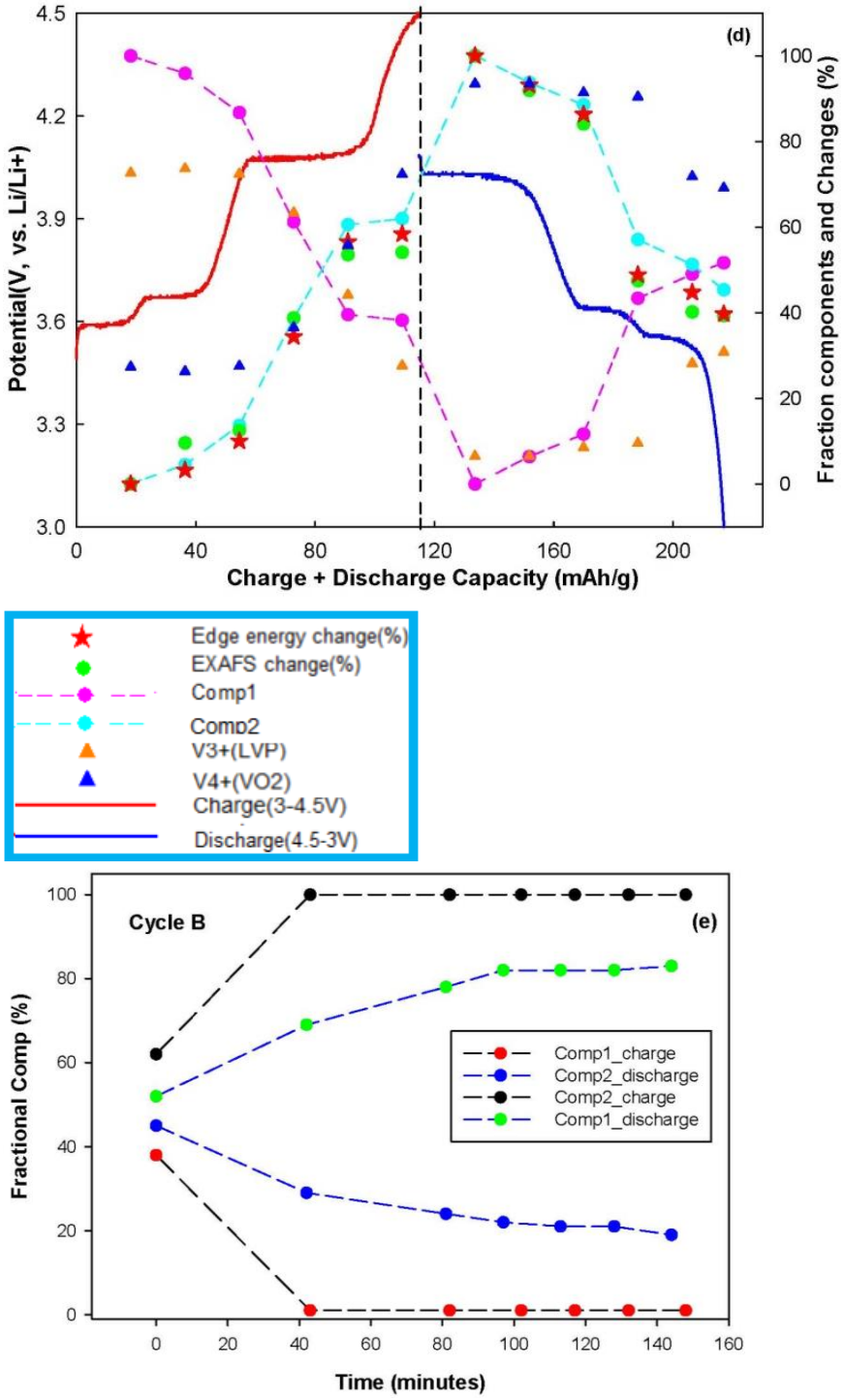

Figure 4.10 0.2C charge/discharge profile while cycling, cycle **B,** (d) PCA & Model fit, (e) results for extra XANES spectra measured during equilibration time..

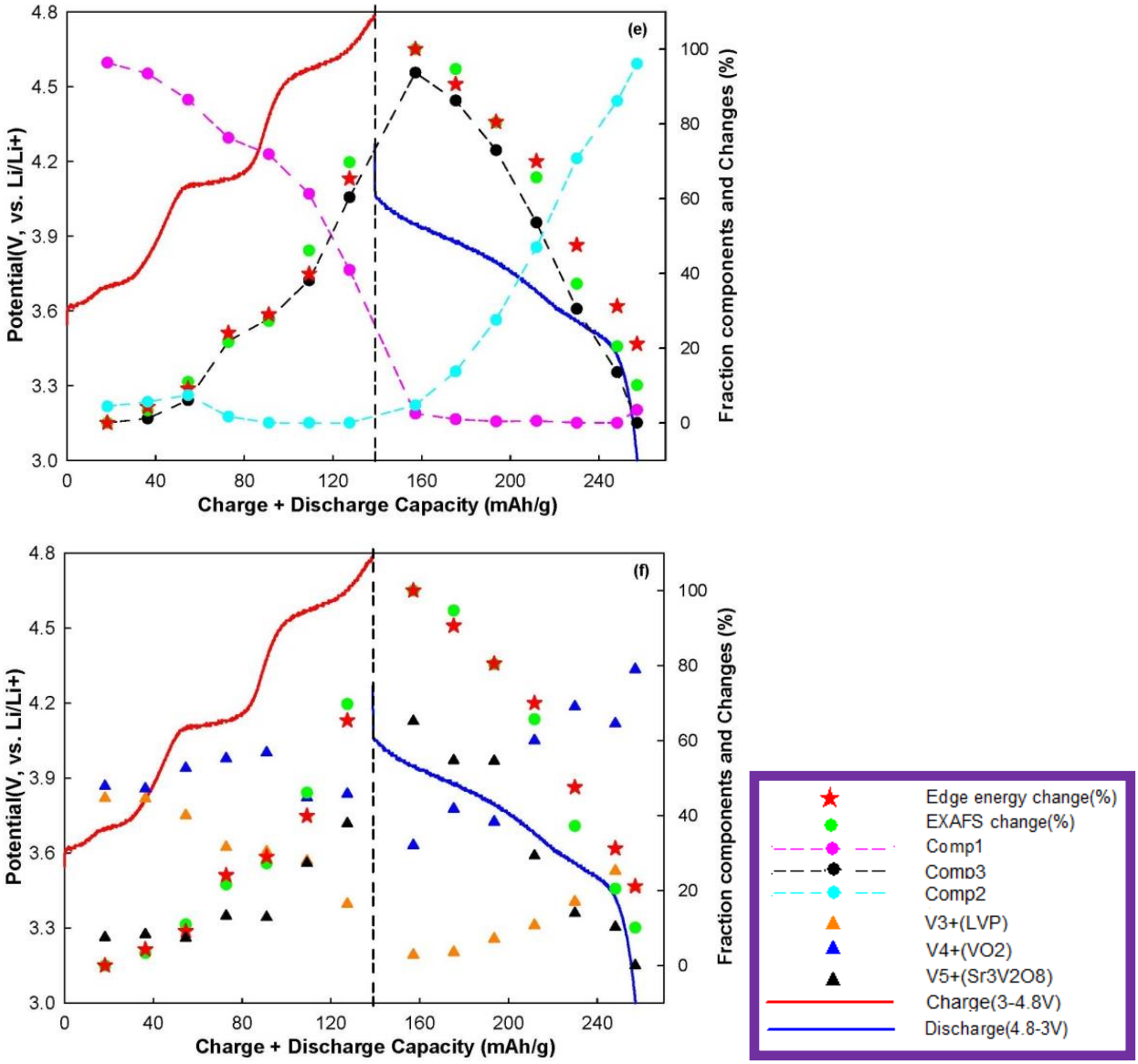

Figure 4.11 0.2C charge/discharge profile while cycling, cycle **D** (e) PCA fit, and (f) Model fit

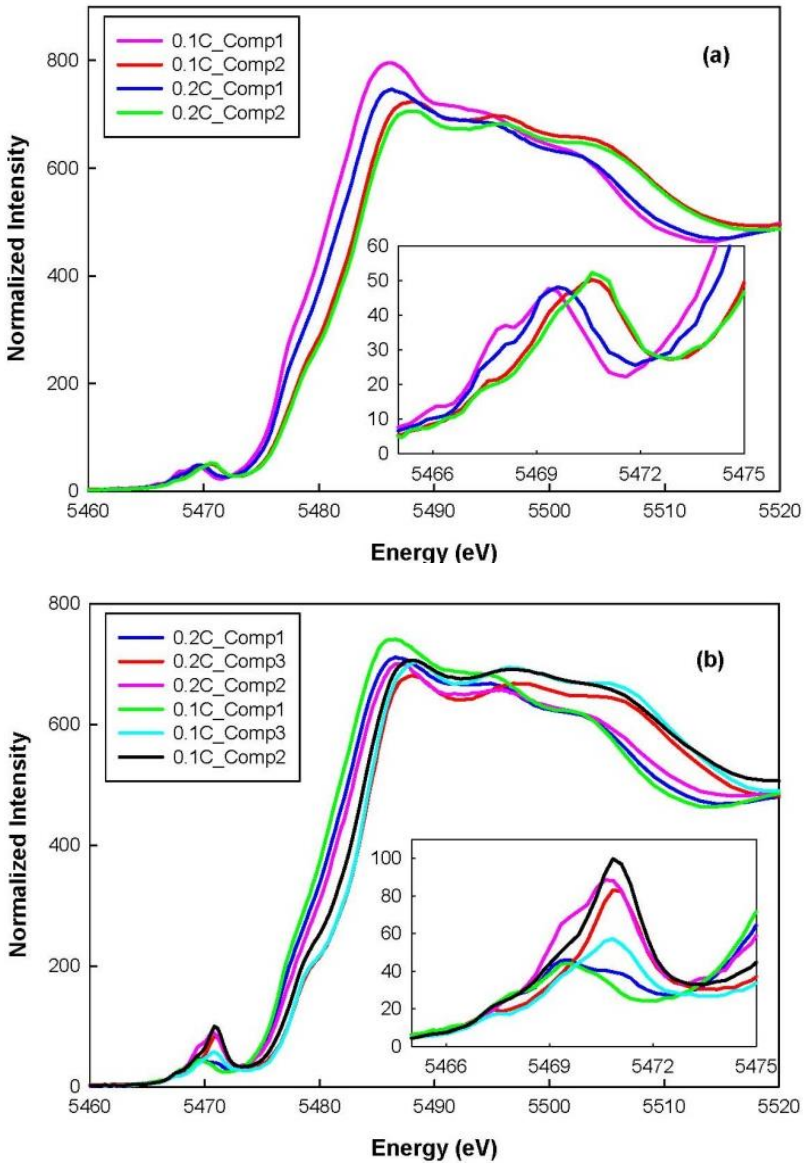

Figure 4.12 Comparison of PCA components, (a) two components for cycle **A&B** (b) three components for cycle **C&D**

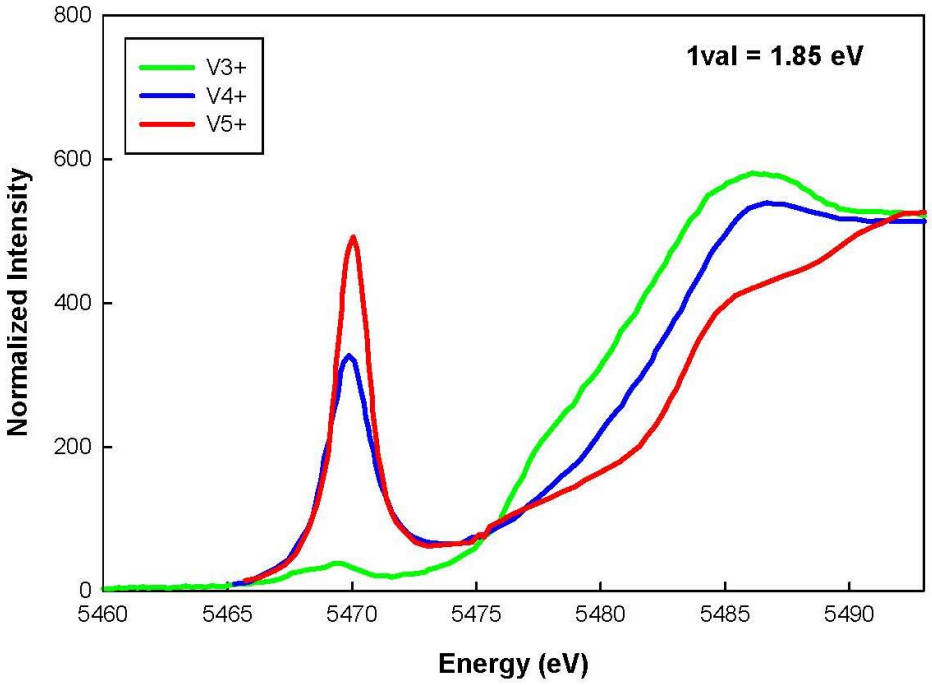

Figure 4.13 Model compound spectra used in the least squares fit, V^{3+} ($Li_3V_2(PO_4)_3$ pristine), V^{4+} (VO_2), V^{5+} ($Sr_3V_2O_8$)[55].

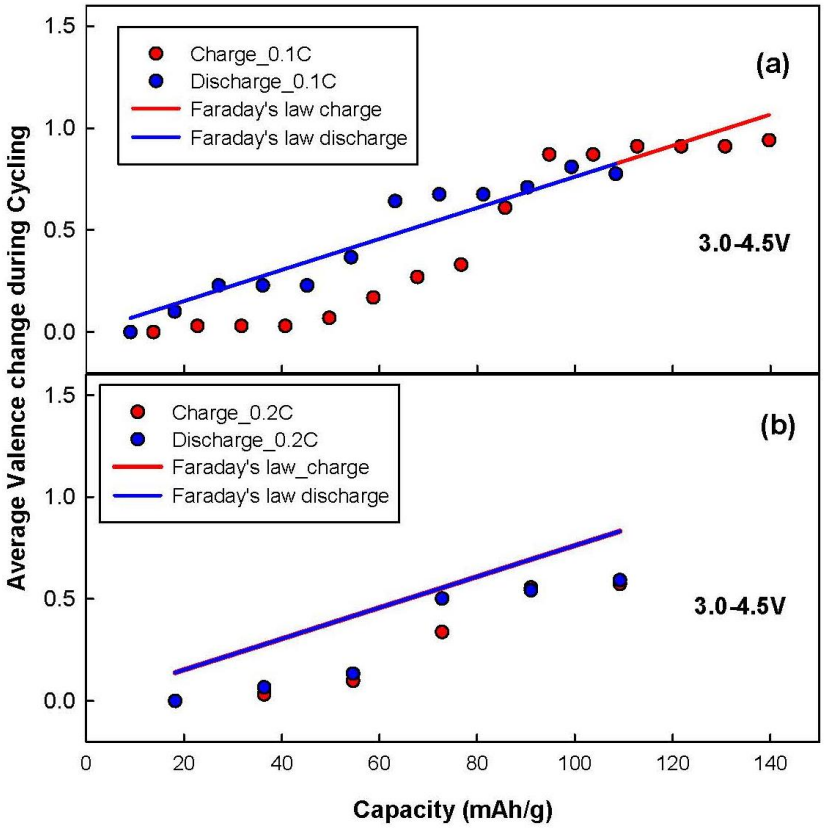

Figure 4.14 Comparison of the average valence change of V vs capacity profiles for the four cycles under two different cut-off voltages, from the Faraday's law calculation and XAS results, (a), (b) 3.0 ⇌ 4.5 V at 0.1C rate

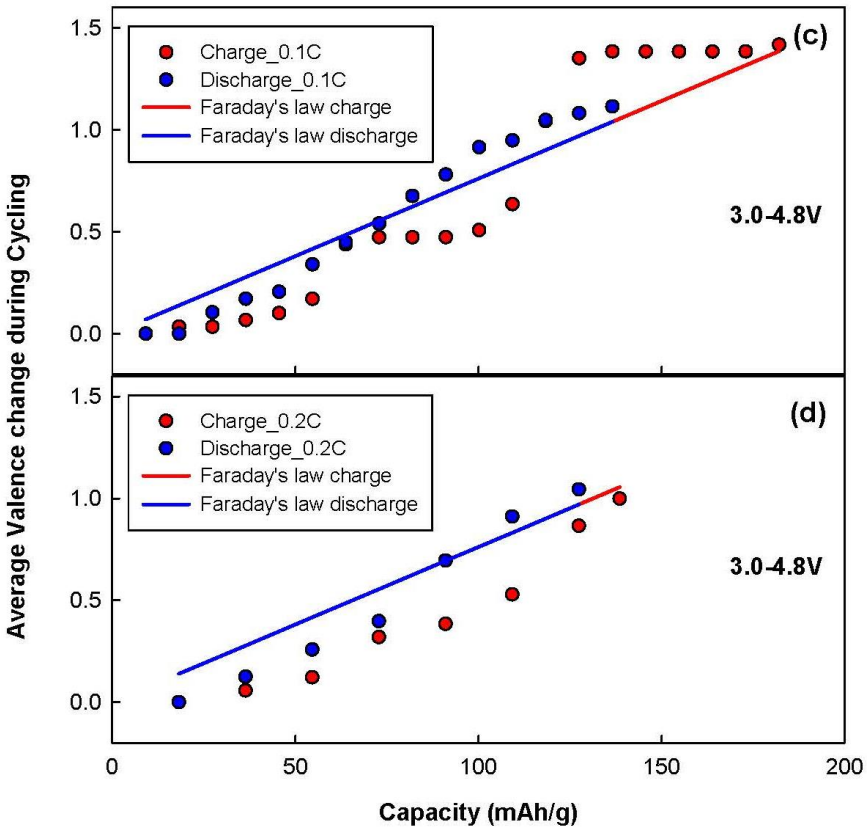

Figure 4.15 Comparison of the average valence change of V vs capacity profiles for the four cycles under two different cut-off voltages, from the Faraday's law calculation and XAS results, (c) and (d) 3.0 ⇌ 4.8 V at 0.2C rate.

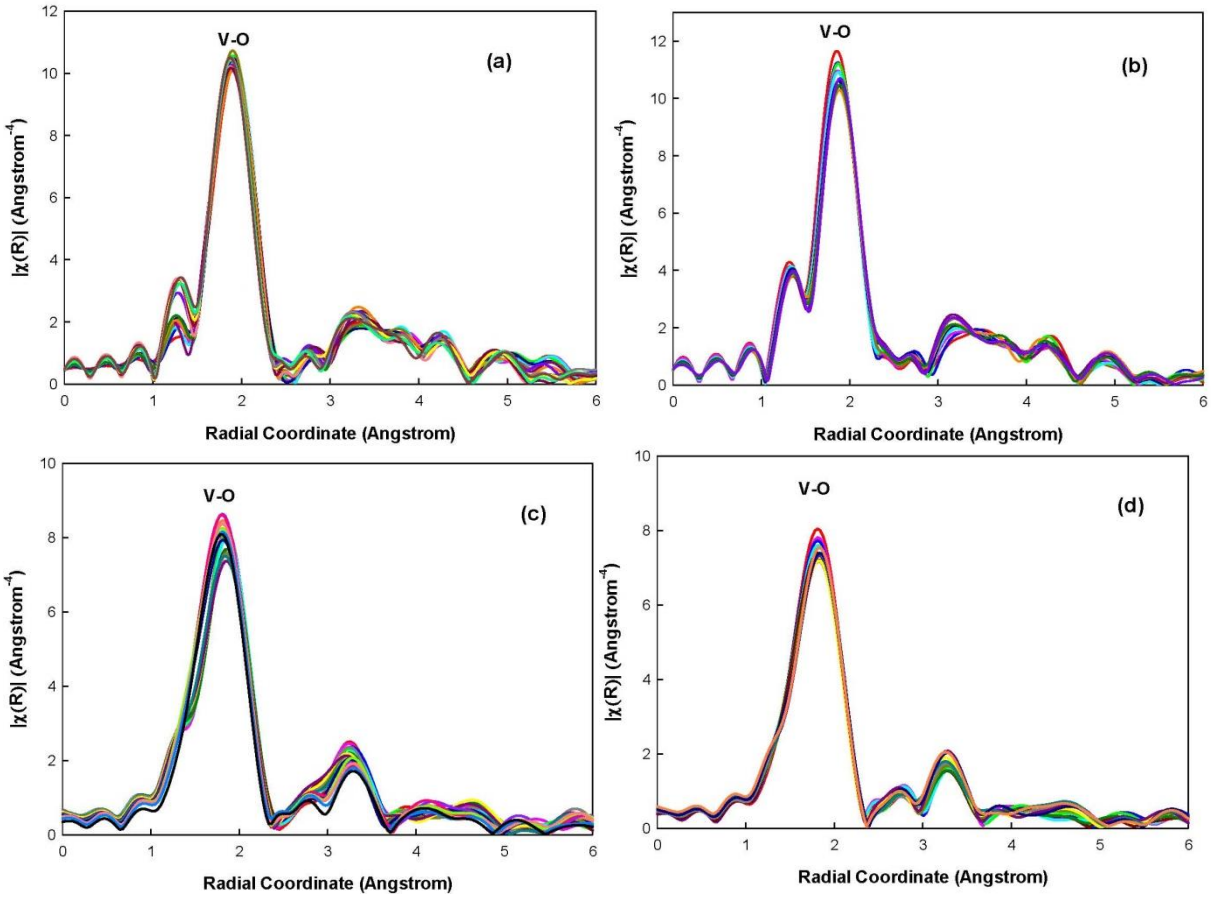

Figure 4.16 V-K edge k^3 -weighted Fourier transform for cycle **A** (a) charge ;(b) discharge, and cycle **C** (c) charge, (d) discharge

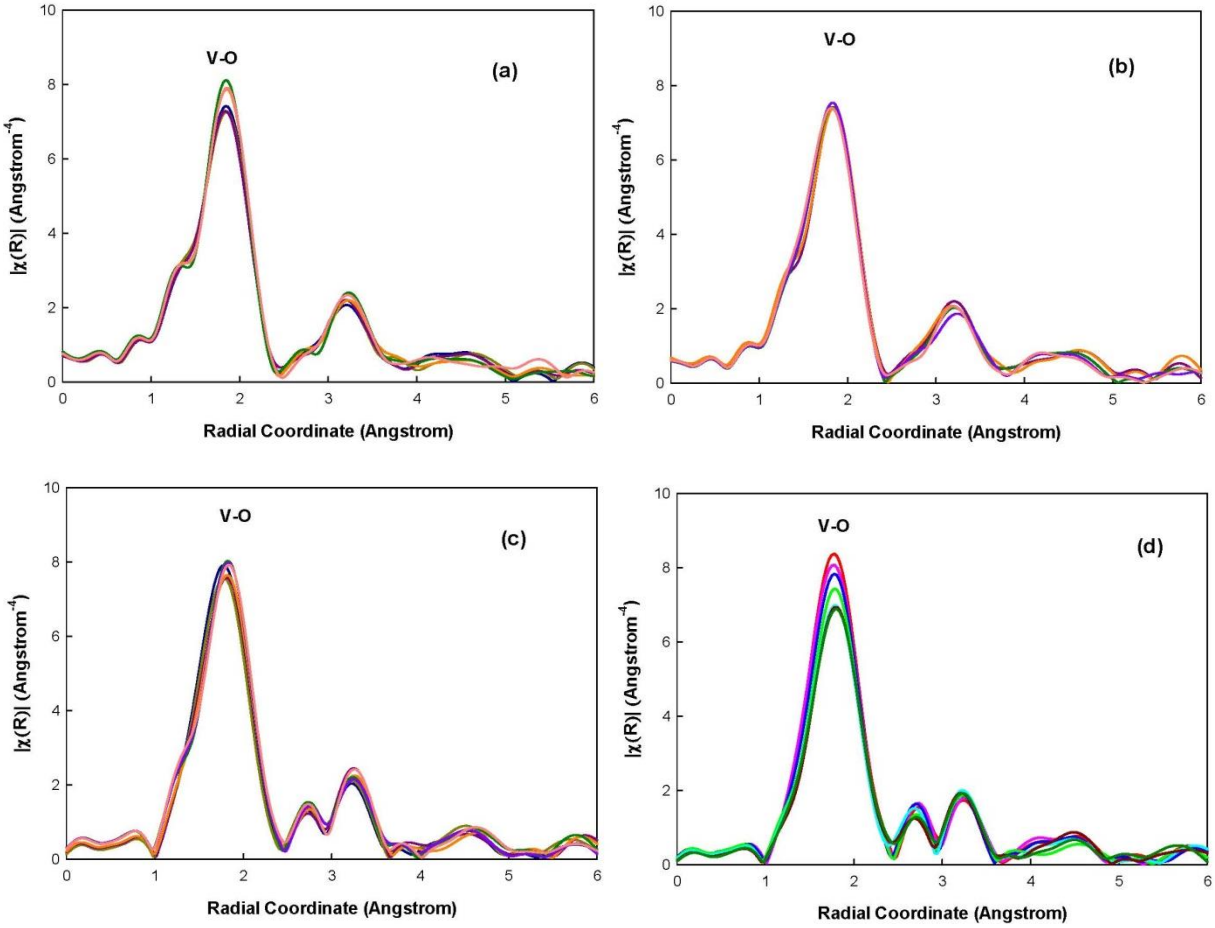

Figure 4.17 V-K edge k^3 -weighted Fourier transform for cycle **B** (a) charge ;(b) discharge, and cycle **D** (c) charge, (d) discharge

Table 4.1 Apparent composition of the electrode at the beginning columns 3-5 give end of each cycle the least squares fit using V^{3+}, V^{4+} and V^{5+} model compounds. The last column shows the average vanadium oxidation state is calculated from the fitted composition. Alteration (last column) the change in vanadium oxidation state can be estimated from the shift in edge energy, assuming 1.85 eV per oxidation state change. For a detailed charge compensation mechanism for each cycle, see **Figures 4.8-4.11**

Cycle	Voltage	V^{3+} (model)	V^{4+} (model)	V^{5+} (model)	Average V oxidation state	Charge Compensation of V in Energy Shift
1st (0.1C) Charge	**3.0**	100	0	–	3**.0**	3**.0**→3.94
	4.5	25	75	–	3.75	
1st(0.1C) Discharge	**4.5**	0	100	–	4**.0**	3.94→3.26
	3.0	42	58	–	3.58	
2nd(0.2C) Charge	**3.0**	72	28	–	3.28	3.26→3.83
	4.5	27	73	–	3.73	
2nd(0.2C) Discharge	**4.5**	6	94	–	3.94	3.83→3.29
	3.0	34	66	–	3.66	
3rd(0.1C) Charge	**3.0**	63	32	5	3.42	3.29→4.70
	4.8	2	32	66	4.64	
3rd(0.1C) Discharge	**4.8**	6	26	68	4.62	4.70→3.50
	3.0	29	69	2	3.73	
4th(0.2C) Charge	**3.0**	45	48	7	3.62	3.50→4.36
	4.8	16	46	38	4.22	
4th(0.2C) Discharge	**4.8**	3	32	65	4.62	4.36→3.50
	3.0	21	79	1	3.84	

Table 4.2: The change in the average V-O nearest neighbor distances observed during the four (**A**, **B**, **C**, and **D**) cycles. 3.0 → 4.5 V and 3.0 → 4.8 V represent the charge cycle, and 4.5 → 3.0 V and 4.8 → 3.0 V represent the discharge cycle. For the charge cycle the value represents the decrease of the V-O bond distance, and for discharge cycle it represents the increase of the V-O bond distance.

Average V-O nearest distance change from EXAFS (Å)							
A (0.1C)		**B (0.2C)**		**C (0.1C)**		**D (0.2C)**	
3.**0**→4.5 V	4.5→3.**0** V	3.**0**→4.5 V	4.5→3.**0** V	3.**0**→4.8 V	4.8→3.**0** V	3.**0**→4.8 V	4.8→3.**0** V
0.049	0.048	0.030	0.034	0.084	0.065	0.049	0.062

4.6 REFERENCES

(1) Wang, D. Y.; Buqa, H.; Crouzet, M.; Deghenghi, G.; Drezen, T.; Exnar, I.; Kwon, N. H.; Miners, J. H.; Poletto, L.; Graetzel, M. *J Power Sources* 2009, *189*, 624.

(2) Zhou, F.; Cococcioni, M.; Kang, K.; Ceder, G. *Electrochem Commun* 2004, *6*, 1144.

(3) Padhi, A. K.; Nanjundaswamy, K. S.; Goodenough, J. B. *J Electrochem Soc* 1997, *144*, 1188.

(4) Chen, J.; Wang, S.; Whittingham, M. S. *J Power Sources* 2007, *174*, 442.

(5) Wang, L.; Zhang, L. C.; Lieberwirth, I.; Xu, H. W.; Chen, C. H. *Electrochem Commun* 2010, *12*, 52.

(6) Huang, H.; Faulkner, T.; Barker, J.; Saidi, M. Y. *J Power Sources* 2009, *189*, 748.

(7) Gaubicher, J.; Wurm, C.; Goward, G.; Masquelier, C.; Nazar, L. *Chem Mater* 2000, *12*, 3240.

(8) Yin, S. C.; Grondey, H.; Strobel, P.; Anne, M.; Nazar, L. F. *J Am Chem Soc* 2003, *125*, 10402.

(9) Yin, S. C.; Grondey, H.; Strobel, P.; Huang, H.; Nazar, L. F. *J Am Chem Soc* 2003, *125*, 326.

(10) Sato, M.; Ohkawa, H.; Yoshida, K.; Saito, M.; Uematsu, K.; Toda, K. *Solid State Ionics* 2000, *135*, 137.

(11) Morgan, D.; Ceder, G.; Saidi, M. Y.; Barker, J.; Swoyer, J.; Huang, H.; Adamson, G. *Chem Mater* 2002, *14*, 4684.

(12) Saidi, M. Y.; Barker, J.; Huang, H.; Swoyer, J. L.; Adamson, G. *Electrochem Solid St* 2002, *5*, A149.

(13) Barker, J.; Gover, R. K. B.; Burns, P.; Bryan, A. *J Electrochem Soc* 2007, *154*, A307.

(14) Barker, J.; Gover, R. K. B.; Burns, P.; Bryan, A. J. *J Electrochem Soc* 2007, *154*, A882.

(15) Barker, J.; Gover, R. K. B.; Burns, P.; Bryan, A. J. *Electrochem Solid St* 2007, *10*, A130.

(16) Huang, J. S.; Yang, L.; Liu, K. Y.; Tang, Y. F. *J Power Sources* 2010, *195*, 5013.

(17) Deb, A.; Bergmann, U.; Cairns, E. J.; Cramer, S. P. *J Synchrotron Radiat* 2004, *11*, 497.

(18) Weng, T. C.; Waldo, G. S.; Penner-Hahn, J. E. *J Synchrotron Radiat* 2005, *12*, 506.

(19) G.N., G.; I.J., P. 1993.

(20) Newville, M. *Journal of Synchrotron Radiation* 2001, *8*, 322.

(21) Rehr, J. J.; Kas, J. J.; Vila, F. D.; Prange, M. P.; Jorissen, K. *Physical Chemistry Chemical Physics* 2010, *12*, 5503.

(22) Victoreen, J. A. *J Appl Phys* 1948, *19*, 855.

(23) Manceau, A.; Marcus, M.; Lenoir, T. *J Synchrotron Radiat* 2014, *21*, 1140.

(24) Wasserman, S. R.; Allen, P. G.; Shuh, D. K.; Bucher, J. J.; Edelstein, N. M. *J Synchrotron Radiat* 1999, *6*, 284.

(25) Soderholm, L.; Antonio, M. R.; Williams, C.; Wasserman, S. R. *Anal Chem* 1999, *71*, 4622.

(26) Gampp, H.; Maeder, M.; Meyer, C. J.; Zuberbuhler, A. D. *Talanta* 1986, *33*, 943.

(27) Rossberg, A.; Reich, T.; Bernhard, G. *Anal Bioanal Chem* 2003, *376*, 631.

(28) Gemperline, P. J. *J Chem Inf Comp Sci* 1984, *24*, 206.

(29) Fernandezgarcia, M.; Alvarez, C. M.; Haller, G. L. *J Phys Chem-Us* 1995, *99*, 12565.

(30) Bardelli, F.; Cattaruzza, E.; Gonella, F.; Rampazzo, G.; Valotto, G. *14th International Conference on X-Ray Absorption Fine Structure (Xafs14), Proceedings* 2009, *190*.

(31) Goraieb, K.; Collins, K. E.; Bueno, M. I. M. S. *X-Ray Spectrom* 2007, *36*, 230.

(32) Li, Y.-F.; Wang, X.; Wang, L.; Li, B.; Gao, Y.; Chen, C. *Journal of Analytical Atomic Spectrometry* 2010, *25*, 426.

(33) Struis, R.; Ludwig, C.; Lutz, H.; Scheidegger, A. M. *Environmental Science & Technology* 2004, *38*, 3760.

(34) Weekley, C. M.; Aitken, J. B.; Witting, P. K.; Harris, H. H. *Metallomics* 2014, *6*, 2193.

(35) Isaure, M. P.; Laboudigue, A.; Manceau, A.; Sarret, G.; Tiffreau, C.; Trocellier, P.; Lamble, G.; Hazemann, J. L.; Chateigner, D. *Geochim Cosmochim Ac* 2002, *66*, 1549.

(36) Richardson, M. *Principal Component Analysis*, 2009.

(37) Prestopronto *http://www.esrf.eu/computing/scientific/PRESTOPRONTO/Prestopronto.htm*.

(38) Pivko, M.; Arcon, I.; Bele, M.; Dominko, R.; Gaberscek, M. *J Power Sources* 2012, *216*, 145.

(39) Cho, A. R.; Son, J. N.; Aravindan, V.; Kim, H.; Kang, K. S.; Yoon, W. S.; Kim, W. S.; Lee, Y. S. *J Mater Chem* 2012, *22*, 6556.

(40) Yang, G.; Ji, H. M.; Liu, H. D.; Qian, B.; Jiang, X. F. *Electrochim Acta* 2010, *55*, 3669.

(41) Qiao, Y. Q.; Wang, X. L.; Xiang, J. Y.; Zhang, D.; Liu, W. L.; Tu, J. P. *Electrochim Acta* 2011, *56*, 2269.

(42) Chen, Q. Q.; Wang, J. M.; Tang, Z.; He, W. C.; Shao, H. B.; Zhang, J. Q. *Electrochim Acta* 2007, *52*, 5251.

(43) Wang, W. H.; Zhang, J. L.; Jia, Z.; Dai, C. S.; Hu, Y. F.; Zhou, J. G.; Xiao, Q. F. *Phys Chem Chem Phys* 2014, *16*, 13858.

(44) Wang, C.; Liu, H. M.; Yang, W. S. *J Mater Chem* 2012, *22*, 5281.

(45) Liu, H. D.; Yang, G.; Zhang, X. F.; Gao, P.; Wang, L.; Fang, J. H.; Pinto, J.; Jiang, X. F. *J Mater Chem* 2012, *22*, 11039.

(46) Wei, Q. L.; An, Q. Y.; Chen, D. D.; Mai, L. Q.; Chen, S. Y.; Zhao, Y. L.; Hercule, K. M.; Xu, L.; Minhas-Khan, A.; Zhang, Q. J. *Nano Lett* 2014, *14*, 1042.

(47) Saidi, M. Y.; Barker, J.; Huang, H.; Swoyer, J. L.; Adamson, G. *J Power Sources* 2003, *119*, 266.

(48) Zhang, L.; Wang, X. L.; Xiang, J. Y.; Zhou, Y.; Shi, S. J.; Tu, J. P. *J Power Sources* 2010, *195*, 5057.

(49) Du, X. Y.; He, W.; Zhang, X. D.; Yue, Y. Z.; Liu, H.; Zhang, X. G.; Min, D. D.; Ge, X. X.; Du, Y. *J Mater Chem* 2012, *22*, 5960.

(50) Chen, Y. H.; Zhao, Y. M.; An, X. N.; Liu, J. M.; Dong, Y. Z.; Chen, L. *Electrochim Acta* 2009, *54*, 5844.

(51) Ren, M. M.; Zhou, Z.; Li, Y. Z.; Gao, X. P.; Yan, J. *J Power Sources* 2006, *162*, 1357.

(52) Huang, H.; Yin, S. C.; Kerr, T.; Taylor, N.; Nazar, L. F. *Adv Mater* 2002, *14*, 1525.

(53) https://code.google.com/p/prestopronto/.

(54) Fu, P.; Zhao, Y. M.; Dong, Y. Z.; An, X. N.; Shen, G. P. *J Power Sources* 2006, *162*, 651.

(55) Zhang, L. L.; Liang, G.; Ignatov, A.; Croft, M. C.; Xiong, X. Q.; Hung, I. M.; Huang, Y. H.; Hu, X. L.; Zhang, W. X.; Peng, Y. L. *J Phys Chem C* 2011, *115*, 13520.

CHAPTER V

CHARACTERIZATION OF $Li_3V_{(2-2x/3)}Mg_x(PO_4)_3$ (X=0.15, 0.3, and 0.45) CATHODE MATERIAL FOR LITHIUM ION BATTERIES

The work in this chapter is in preparation for publication:

Soojeong Kim, Zhengxi Zhang, Senlin Wang, Li Yang, James E Penner-Hahn, Aniruddha Deb " $Li_3V_{(2-2x/3)}Mg_x(PO_4)_3$($x$= 0.15, 0.3, and 0.45) cathode material of Lithium ion batteries electroche mical and structural analysis."

5.1 INTRODUCTION

The capacity and rate performance of polyanion materials depend strongly on their electronic conductivity, which can vary from 10^{-10} to 10^{-9} S cm^{-1} for pure $LiFePO_4$ [1,2] to 10^{-8} to 10^{-7} S cm^{-1} for $Li_3V_2(PO_4)_3$.[3,4] It has been shown that electroactive metal doping or mixing with electro-conductive materials such as Zr, Ti, Fe, Al, and Cr can be used to effectively improve electronic conductivity, specific capacity, cycle performance, and rate capability and performance with high material utilization. Furthermore comparatively low discharge-capacity fading of $Li_3V_2(PO_4)_3$,[3-10] and Mg^{2+} doping have been shown to improve the ion conductivity of $Li_3V_2(PO_4)_3$ to that of $LiFePO_4$ [1,2] and enhance its capacity and rate capability. Therefore,

replacing V^{3+} with lighter metal Mg^{2+} is considered to be favorable system applied to $Li_3V_2(PO_4)_3$ parent structure. This chapter discusses the structural properties of Mg-doped $Li_3V_2(PO_4)_3$.

This system forms a variety of active phases with good electrochemical properties, such as higher specific capacity and better cycling performance. Electrochemical tests show that Mg-doped LVP has good charge/discharge cyclic stability. With the highest discharge capacity and good cyclic stability, 30% Mg-doped system turns out to be the optimal. Even after long term cycling, structure stability was even more enhanced with Mg doping than parent LVP system in the *ex-situ* XRD studies. For example, in $Li_3V_{1.8}Mg_{0.3}(PO_4)_3$/C, charge/discharge capacity retention is 91.4% (1.0 C) after 100 cycles. In contrast, the pure LVP shows a fast decline in capacity during the cycling and has 25.6% capacity fading after 100 cycles.[11] It supports the idea that Mg doping in the LVP system helps to improve electrochemical conductivity and structural stability.

5.2 EXPERIMENTAL

5.2.1 Preparation of $Li_3V_{(2-2x/3)}Mg_x(PO_4)_3$/C (x= 0.15, 0.3, and 0.45) Composites and Electrode

The LVP composite electrodes were prepared as described in Chapter 4, with the appropriate modifications in stoichiometry to provide Mg doping.[11]

5.2.2 Electrochemistry and XAS experiment for 3 different compositions of $Li_3V_{(2-2x/3)}Mg_x(PO_4)_3/C$ (x= 0.15, 0.3, and 0.45)

Charge–discharge cycling was performed at room temperature at the DND-CAT beam line (Sector 5), at the Advanced Photon Source Argonne National Laboratory, with a potentiostat/galvanostat system (Princeton Applied Research, Model Versa) under constant current control. Charging and discharging were performed at a constant current 0.1 C (1.0 C=140 mA/g) with different cut-off voltages such as 3.0 ⇌ 4.5 V, 3.0 →4.8 V, and 4.8 → 2.0 V as shown in **Figures 5.1 – 5.3**. For better understanding, the result for cycling between 3.0 →4.8 V (charge), and 4.8 → 2.0 V (discharge) have been 0.6 V down shifted. XAS measurements were performed while the electrochemical cell was cycled at 0.1C rate with a current density of 0.018 mA/cm^2, 0.020 mA/cm^2, and 0.018 mA/cm^2 for 15%, 30%, and 45% Mg-doped $Li_3V_{(2-2x/3)}Mg_x(PO_4)_3/C$ between 3.0 → 4.5 V and 3.0 → 4.8 V cut off voltages. Model compounds (See **Figure 5.4**), pure $Li_3V_2(PO_4)_3$ (V^{3+}), VO_2(V^{4+}), and V_2O_5(V^{5+}) were measured as XANES references. The total change in edge energy was judged as the energy at 650 cm^2/g. From this, we can calculate the fractional change in edge energy for each successive scan. From the model compounds, we find that the edge shifts by ~1.85 eV between V^{3+} and V^{4+}, allowing us to estimate the average oxidation state of an unknown.

5.3 RESULTS & DISCUSSION

5.3.1 Electrochemical Characterization

The cycling for the 30%, and 45% Mg-doped LVP within the different cut-off voltage ranges of 3.0 ⇌4.5 V for the first charge and discharge cycle, 3.0 → 4.8 V & 4.8 → 2.0 V for the second discharge, all at 0.1C rate are shown in **Figures 5.1 – 5.2**. During 3.0 → 4.5 V cycling, three significant plateau regions are seen for both charge and discharge cycles of all three compositions. The plateaus are at approximately 3.6 V, 3.7 V and 4.1 V, (*vs.* Li/Li^+) for both charge and discharge. The first cycle in 30 % system shows significant hysteresis (~30 mAh/g) and even larger capacity loss (~40 mAh/g). The first cycle in the 45% system shows significant hysteresis (~25 mAh/g) and capacity loss (~20 mAh/g), with modest capacity recovery on the charge cycle and a somewhat smaller capacity loss on the discharge cycle. As long as the voltage is limited to 4.5 V, well defined thresholds are seen on both charge and discharge, demonstrating electrochemical reversibility. Earlier work, using chemically-prepared $Li_xV_2(PO_4)_3$ (x=0,1,2,3) attributed the hysteresis to the presence of oxidation state ordering.[3] Our data suggests a simpler explanation, at least for our measurements. Based on our XAS data (**Figures 5.12, 5.15**), V is not fully oxidized by the end of the oxidative half of the cycle. It is only after the cathode has been allowed to equilibrate at 4.5 V for ~ 1 h that we see full formation of V^{4+}. The same thing happens at low voltage. The average V oxidation state (as determined from XANES fits (**Figures 5.12**, **5.15**), is 3.49 (30% system), and 3.40 (45% system) at the end of the first discharge but 3.2 (30% system), and 3.1 (45% system) at the start of the second charge. The apparent hysteresis in our measurements is thus the result of equilibration of the bulk material with the surface, such that the electrochemically active surface sites are

different at the start of the reductive cycle than they are at the end of the oxidative cycle. However, when the electrode is cycled above 4.5 V, no plateaus are observed on discharge. When the voltage is increased above 4.5 V, a fourth plateau is seen at 4.55 V, as in the parent LVP material. During discharge from 4.8 →2.0 V, no plateau was present for 30% & 45% Mg-doped system, similar to what we saw for parent LVP. Based on these observations, we can conclude that electrochemical behavior is reversible for 30% and 45% LVP as long as the potential does not go above 4.5 V in the charging cycle. Above 4.5 V, there can be some changes to the system that can lead to an even larger hysteresis between charge and discharge. Therefore, based on the electrochemistry result, we can expect that a significant change has been made to the system in the cycling above 4.5 V which shows irreversible cycling.

Somewhat different behavior is seen for the 15% Mg-doped system (**Figure 5.3**). As before, there are three plateaus but they are shifted slightly to higher voltage on charging to the other LVP system. On discharge the plateaus are all shifted slightly down, in contrast with the other LVP plateaus systems where the charge and discharge plateaus occur at approximately the same voltages. When the 15% Mg system is charged above 4.5 V a fourth plateau was not observed, at least not up to 4.8 V. Finally, on discharge from 4.8 → 2.0 V, there are two significant plateaus (3.9 V and 3.5 V) (**Figure 5.3**) in contrast with other LVP materials which did not show any plateaus during discharge from this voltage.

5.3.2 XANES of Charge/Discharge

In-situ vanadium K-edge XANES are shown in **Figures 5.5 – 5.10**. Data were measured at a rate of 0.1 C and cut off voltages 3.0 ⇌ 4.5 V for the first cycle and 3.0→ 4.8 V & 4.8 → 2.0 V for the second cycle. On the first cycle, it is clear that the pre-edge intensity is low for all three compositions. As for pure LVP, both the energy of the 1s → 3d peak shifts and the overall edge energy shift to higher energy on charging and shift back to lower energy on discharging. The low 1s → 3d intensity is consistent with a VO_6 octahedral environment being preserved during cycling for all compositions. The structure for Mg-doped LVP system is monoclinic (space group $P2_1/n$) with Mg substitutes for V. As discussed in Chapter 4, this given distorted VO_6 octahedra and PO_4 tetrahedra share oxygen vertexes. The XANES spectra for 3.0 ⇌ 4.5 V cycling are consistent with this structure.

In sharp contrast, the 1s → 3d intensity is more than doubled when the potential is raised to 4.8 V, and this increase is not reversed during the reductive half of the cycle, especially in the 15% LVP system. This increase in 1s → 3d intensity is consistent with a distorted V environment. The reference spectra (**Figure 5.4**) gave equivalent results, but allowed an estimate of the average oxidation state. This enabled us to track the charge compensation taking place *in-situ*. Therefore, the pre-edge feature shown above 4.5 V can be determined as additional oxidation of vanadium more than V^{4+}. This means that the vanadium is more oxidized towards V^{4+} and/or towards V^{5+} at the end of the 4.8 V where a higher pre-edge intensity is observed (shown in (c) and (d) of the **Figures 5.6, 5.8, 5.10**). This is similar to the observation in Chapter 4. As in that case, we suggest that a portion of the V migrates to one of these Li vacant sites. Without knowing the details of the V site, it is impossible to estimate the fraction of anti-site

mixing. However, if the migrated V had a spectrum similar to V in VO_2 , as seen in **Figure 5.4**, overall it is possible that as little as 10% of the V could be present in the Li site of all three systems. Comparing the highest peak intensity of the 3.0 → 4.8V/ 4.8 → 2.0 V cycling (inset of (c) and (d) in the **Figures 5.6, 5.8, 5.10**), 15% Mg-doped system shows the highest intensity, and 45% Mg-doped system shows the lowest intensity. Especially, in the 15% Mg-doped system ((d) in **Figure 5.10**), the intensity of the 1s → 3d region shows difference compared to the feature from the 30% ((d) in **Figures 5.6**) and 45% ((d) in **Figures 5.8**) Mg-doped system. **Figures 5.6, 5.8** (d) show no splitting and the intensity decreases as low as the intensity from the original octahedral structure. This means that the intensity in the 30% system and 45% system mostly recovers their original VO_6 geometry in the bulk system even though the potential goes above 4.5 V / below 3.0 V. Once potential approaches 4.8 V, the biggest change was made in the V geometry. This can be estimated roughly by comparing pre-edge peak intensity. For example, as shown in (c) and (d) from **Figures 5.6,5.8,** 30 % system shows ≈ 135, and 45 % system shows ≈ 95. Since tetrahedral V^{5+} model compound peak intensity is ≈ 500, it allows us to estimate the fraction of the vanadium migration into the tetrahedral geometry. When the potential reaches near or at 4.8 V, 27%, and 19% of vanadium stays in the T_d in the 30% and 45% Mg-doped system. For discharging cycle during 4.8 → 2.0 V, we see significant irreversible cycling features from electrochemistry(**Figures 5.1, 5.2**). By comparing XANES and electrochemistry result, we can understand that the majority of the distorted vanadium in the bulk recovers its original octahedral structure, whereas the small fraction of the vanadium in the surface show irreversible cycling feature in the electrochemistry result as shown in **Figures 5.1, 5.2**.

In contrast, in the 15 % system, the intensity grows pretty sharply during 3.0 → 4.8 V charge and decreases distinctly during 4.8 → 2.0 V discharge. When potential reaches near at 4.8 V, intensity close to 180 in the pre-edge region is shown; meaning that ≈ 36%, of vanadium stays in the T_d in the 15% Mg-doped system. And, when voltage approaches to 3.0 V, it shows a sudden 1s → 3d splitting and then a further step (below 3.0 V) shows a sudden intensity increase which corresponds to the idea that 15% Mg-doped system has faced significant structural changes based on anti-site mixing during 4.8 → 2.0 V discharge (irreversible cycling). At this point, it may be possible to estimate that 15% change is close to the change happening in **Figure 4.6** (h) in Chapter 4 where, the intensity does not recover its original octahedral structure. Furthermore, to clarify the irreversibility that happens in the 15% materials, we can look at the electrochemistry result and XANES during the discharging cycle (4.8 → 2.0 V). Here, we see irreversible cycling feature from electrochemistry but it is somewhat different than the 30% and 45% systems(**Figures 5.3**). When comparing the results of electrochemistry and XANES together, we can understand that the majority of the vanadium in the bulk is highly distorted, with V migration based on anti-site mixing leading to irreversible features from both results. The general difference between XAS and electrochemistry happens because the electrochemistry result reflects only surface chemistry, while the XAS result reflects bulk chemistry, as discussed in the previous chapter.

The XANES edge energy shifts were used to estimate the change in average vanadium oxidation state during charge/discharge cycling. This was achieved by comparing the energy at 650 cm^2/g. (**Table 5.1** (a)) Assuming that the energy shift is 1.85 eV per oxidation state, the average V oxidation state can be estimated as shown in **Table 5.1** (b).

5.3.3 Principal Component Analysis

Our data analysis procedure for Principal Component analysis is the same as the one used in Chapter 4. We first use PCA[12] to determine the number of unique components that are required to account for the observed data. For 3.0 ⇌ 4.5 V cycling; only two components are necessary to fit the data for all three systems; for 3.0 → 4.8 V and 4.8 → 2.0 V cycling, four components are required for the 15% system; and, three components are required for the 30% and 45% systems. **Figure 5.11** (a) and (b) shows the Residual Standard Deviation (RSD) plot showing the maximum number of principal components needed in the PCA analysis. This supports the qualitative conclusion above that when the potential is raised above 4.5 V, the cathode suffers some sort change and, that for 15% Mg-doped system, this change is not recovered.

Once the number of principal components has been utilized, the next step is to obtain the reconstructed XANES components by ITFA shown in (b) of **Figures 5.14, 5.17, 5.20** and (c) of **Figures 5.14, 5.17, 5.20** and these components are used to do a least square fit to obtain the fractional composition for fitting with the measured XANES spectra. The results of the PCA analysis are shown in (a) of **Figures 5.12, 5.13, 5.15, 5.16, 5.18, 5.19**. As proposed for LVP charge compensation,[13] from the electrochemical data in **Figures 5.1 – 5.3**, there are two well-defined plateaus near 3.6 V/3.7 V, representing the extraction of one Li, followed by removal of a second Li at the plateau of 4.1 V. The PCA analysis for the 3 ⇌ 4.5 V cycling, (a) of **Figures**

5.12, 5.15, 5.18 shows that there are two principal components for V. In addition, **Figure 5.11** (a), RSD plot also supports the idea of two components for all three systems.

Figures 5.12(a) and 5.15(a) both contain least square fits of PCA components and EXAFS change (V – O bond distances (in green dot)) in fraction. These changes follow each other closely. For the discharge, unlike the charge cycle, the PCA analysis shows that the two components change monotonically throughout the cycle. Within the qualitative analysis (PCA, EXAFS change in percentage), the 30% material shows a shorter plateau at the beginning rather than a long plateau for 0% LVP. These plateaus are due to same reason discussed in Chapter 4, where the mass transport within the particles of the active material does not permit rapid equilibration of the particle composition, corresponding to the Li extraction, and so the bulk composition at a certain state of charge is different than the one from surface composition. Also, the starting voltage of the charge cycle doesn't match exactly the 0% LVP material, but is similar. There seems to be less relaxation between the last charge scan and the first discharge.

Since PCA analysis shows the presence of two principal components (which resembles the V^{3+} and V^{4+} species) for the 4.5 V cut-off, to obtain a quantitative picture of the charge compensation, V^{3+} and V^{4+} model compounds fitting is necessary. The results of the fit are shown in (b) of **Figures 5.12, 5.15**. The results clearly show that, in the 30% Mg-doped system, V^{3+} dominates at the start of the charge cycle, and, $V^{4+;}$ at the end. Furthermore, V^{4+} starts the discharge and at the end, a mixture of 50%:50%= V^{3+}:V^{4+} is shown.

For cycling above 4.5 V, in **Figure 5.11**(b), more than two components are needed to reconstruct the XAS plot for the cycling between 3.0 → 4.8 V/4.8 → 2.0 V cut-offs. There are

three principal components both in the 30 % and 45% Mg-doped systems (see **Figures 5.13** (a)**, 5.16** (a)). It shows that after 100-130 $mAhg^{-1}$, the new component (Comp 2) starts to increase until the end of the charge cycle. On the way back to discharge, Comp2 decreases monotonously, and Comp1 increases monotonously. This corresponds to the idea mentioned previously from XANES pre-edge description that, during 4.8 → 2.0 V discharge in the 30% and 45% system both recover their original octahedral structure. This idea matches with the model fit in **Figures 5.13, 5.16** (b)) which show the increase of the C1 (the most reduced component, close to V^{3+} with O_h geometry) at the end of discharge.

In contrast, it is interesting that the 15% Mg-doped system is a little different. **Figure 5.18** (a) shows no plateau until 4.2 V, unlike all the rest (0%, 30%, and 45%) during 3.0 ⇌ 4.5 V cycling. In addition, it is interesting that, for cycling above 4.5 V, and below 3.0 V, (**Figure 5.11**(b)), this system requires at least four components in order to reconstruct actual experimental spectra. From the component fit plot in the **Figure 5.20**(c) four components can be understood as Comp1(close to O_h V^{3+}), Comp4(close to O_h V^{4+}/V^{5+}), Comp3(close to distorted T_d V^{3+}/V^{4+}), and Comp2(close to T_d V^{4+}/V^{5+}). And, when we apply this idea to **Figure 5.19**(a), for example, it is reasonable to understand that Comp1(close to O_h V^{3+}) decreases during charge(3.0 - 4.8 V) and Comp4 (close to O_h V^{4+}/V^{5+}) increases (due to regular oxidation) and then decreases (due to vanadium partial migration into T_d) during charge cycle, Comp2 (close to T_d V^{4+}/V^{5+}) starts to increase near 4.8 V (due to vanadium partial migration into T_d), and no Comp3 (close to T_d V^{3+}/V^{4+}) is present because it appears when V^{3+}/V^{4+} migration happens. Thus, Comp3 especially appears during discharge (4.8 →2.0 V) when potential goes below 3.0 V. During discharge (4.8 → 2.0 V) the most important thing that should be noticed is that appearance of Comp3 near 2.0

V. This is absolutely logical in regards to both PCA fit (**Figure 5.19**(a)) and model fit (**Figure 5.19**(b)) in that they both show irreversible changes based on anti-site mixing into empty Li sites.

As discussed in chapter 4, additional scans were recorded to investigate the rate of electrode relaxation, After the end of charge and discharge cycle, the electrochemical reaction cell was allowed to equilibrate for ~260 minutes. In all cases, relaxation is seen. For 30% and 45%, the relaxation is too fast for us to obtain any kinetic information using these data. In contrast, for the 15% doped sample (**Figure 5.18**(b)) the relaxation rate is noticeably slower, particularly on discharge, with relaxation continuing for at least 200 minutes. Surprisingly, the relaxation on charge is partially reversed beyond ~100 minutes for this sample, perhaps suggesting a small leakage current.

5.3.4 EXAFS for 3 different Compositions

The EXAFS data shown in **Figures 5.21–5.23** give a similar picture. In all three systems, we expect V – O nearest neighbors, together with V⋯P and V⋯V outer shell scattering. There isn't much change in the distance during charge/discharge cycles. However, by comparing two different cut off results, we see that the outer shell (~2.2 Å – 3.8 Å) features in (a), (b) from **Figures 5.21 – 5.23** and (c), (d) from **Figures 5.21 – 5.23** show a significant differences. However, the changes shown in all three systems aren't the same; as shown in (a) and (b) in **Figures 5.24**, the outer peak for 45% system is much weaker and has a much shorter length than the others. And, 30% system is also a bit different from 15% system. Secondly, it should be noticed that 15% system loses the outer shell while cycling above 4.5 V and below 3.0 V,

consistent with more V in the Li sites for this composition.ge.[3,4] Also, there are reversible changes in the average V – O nearest neighbor distance shown in **Table 5.2** which is consistent with oxidation and reduction of the V ions. The change in the V –·O distances from EXAFS also closely follows the PCA components from all three components, as shown previously in **Figures 5.12, 5.13, 5.15, 5.16, 5.18, 5.19** with green dots. Based on **Table 5.2**, it is easily noticeable that the average distance changes during 3.0 ⇌ 4.5 V cycling; the biggest change is shown in the 30% Mg-doped system (≈ 0.80 Å) and for next cycling all three show similar distance changes (≈ 0.90 Å) during charge/discharge cycling. The V-O distance change follows the charge/discharge capacity change which means that if there is big charge/discharge capacity, it matches with bigger V – O distance change.

5.4 CONCLUSION

We interpret the result as evidence that the electrochemical measurements reflect only the state of the V ions on the surface of the $Li_3V_2(PO_4)_3$ particles, while XAS is sensitive to all of the V in the sample. These data thus imply that an important limitation in $Li_3V_2(PO_4)_3$ batteries will be the rate of electron (or perhaps Li) transferring from the bulk to the surface of the $Li_3V_2(PO_4)_3$. The apparent hysteresis in our measurements is the result of equilibration of the bulk material with the surface, such that the electrochemically active surface sites at the start of the reductive cycle are different from those at the end of the oxidative cycle.

XANES and PCA results for 30% and 45% show the recovery of their original octahedral geometry even though the potential goes above 4.5 V and below 3.0 V. This is because, during

discharge from 4.8 → 2.0 V, the 30% and 45% systems recover their original low intensity in the 1s → 3d region in the XANES ((d) in **Figures 5.6, 5.8**) not like 15% system (**Figure 5.10** (d)). Also, in the PCA and model fit result, the component close to V^{3+} (most reduced) increases as the discharge cycle continues. Therefore, we can expect that 30% and 45% Mg-doped systems do not lose their reversibility in the bulk system even at high potential, unlike 15%. Combining electrochemistry result and cyclability result, the 30% Mg-doped system shows high stability characteristics. For a better understanding of these systems' stability and electrochemical performances at high potential, more cycling tests and XAS experiments are recommended. In addition, the unique features of the 15% system at high/low potential can be understood by the fact that kinetics does not limit it, unlike the others. Furthermore, it also is related to ion mobility that allows for a more rapid V transport into the empty Li sites, ultimately leading to a majority of V to face anti-site mixing at the high/low potentials. However, many other common issues happening in the battery system besides the material contents, such as electrolyte degradation, forming SEI layer, etc.,[14] could be involved. Therefore, more work needs to be performed in the higher potential range, not only with electrochemistry experiment which shows surface reaction but also with the XAS experiment which gives a detailed idea about the bulk system.

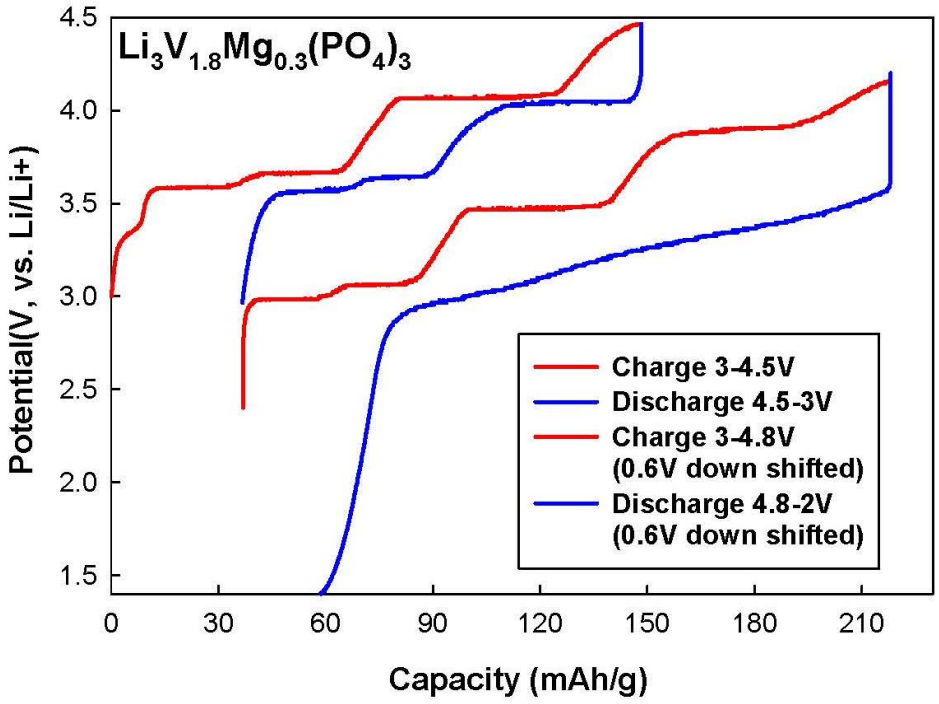

Figure 5.1 30% Mg-doped LVP, $Li_3V_{1.8}Mg_{0.30}(PO_4)_3$, Electrochemistry experiment for 0.1C cycling between 3.0 ⇌ 4.5 V(1st cycle), 3.0 → 4.8 V & 4.8 → 2.0 V(2nd cycle).

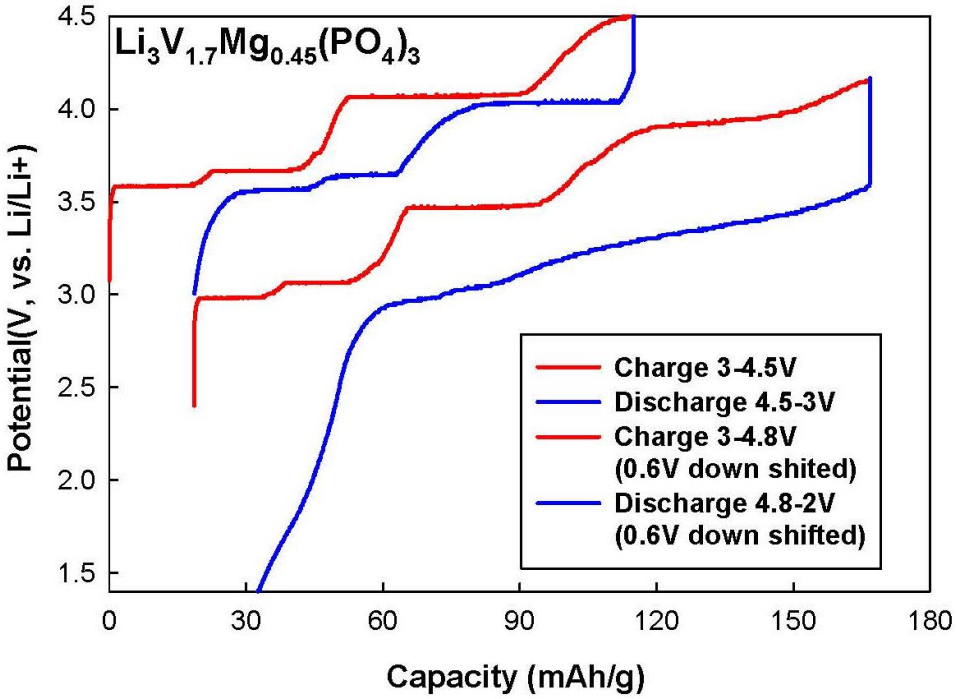

Figure 5.2 45% Mg-doped LVP, $Li_3V_{1.7}Mg_{0.45}(PO_4)_3$, Electrochemistry experiment for 0.1C cycling between 3.0 ⇌ 4.5 V(1st cycle), 3.0 → 4.8 V & 4.8 → 2.0 V(2nd cycle).

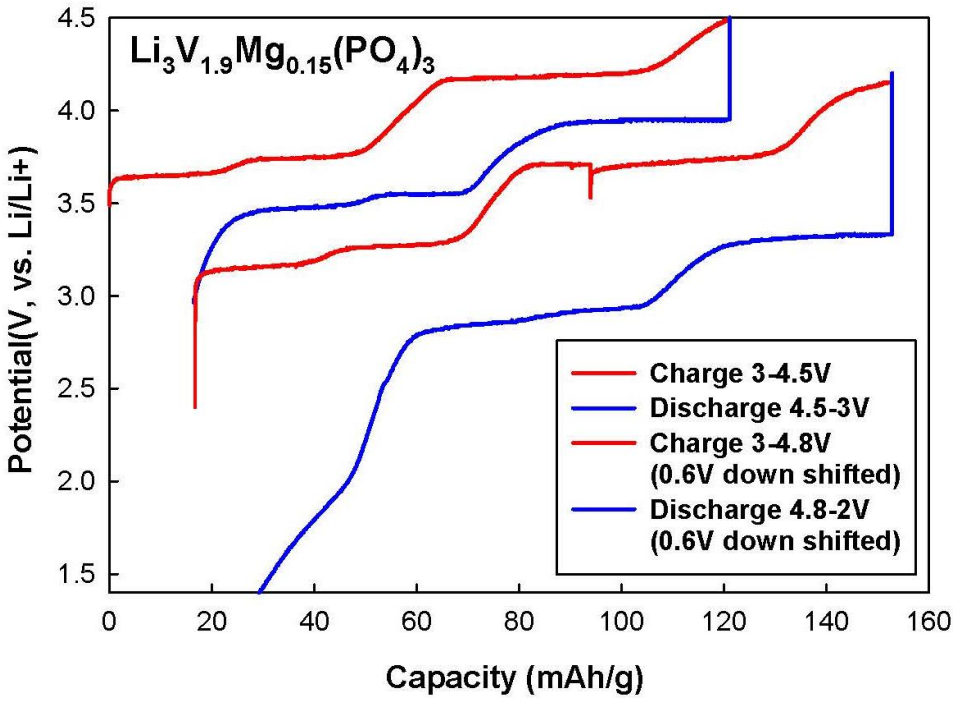

Figure 5.3 15% Mg-doped LVP, $Li_3V_{1.9}Mg_{0.15}(PO_4)_3$, Electrochemistry experiment for 0.1C cycling between 3.0 ⇌ 4.5 V(2nd cycle), 3.0 → 4.8 V & 4.8 → 2.0 V(3rd cycle).

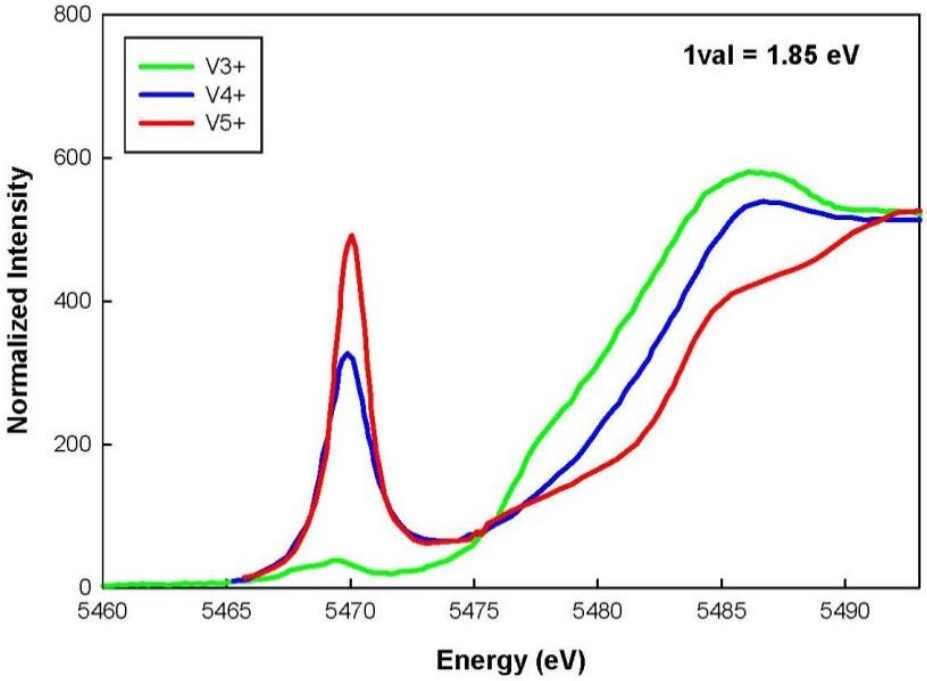

Figure 5.4 Model compound spectra for Vanadium, pure $Li_3V_2(PO_4)_3$ (V^{3+}), VO_2 (V^{4+}), V_2O_5(V^{5+}) valence calculation based on model compound, 1 valence= 1.85eV in average.

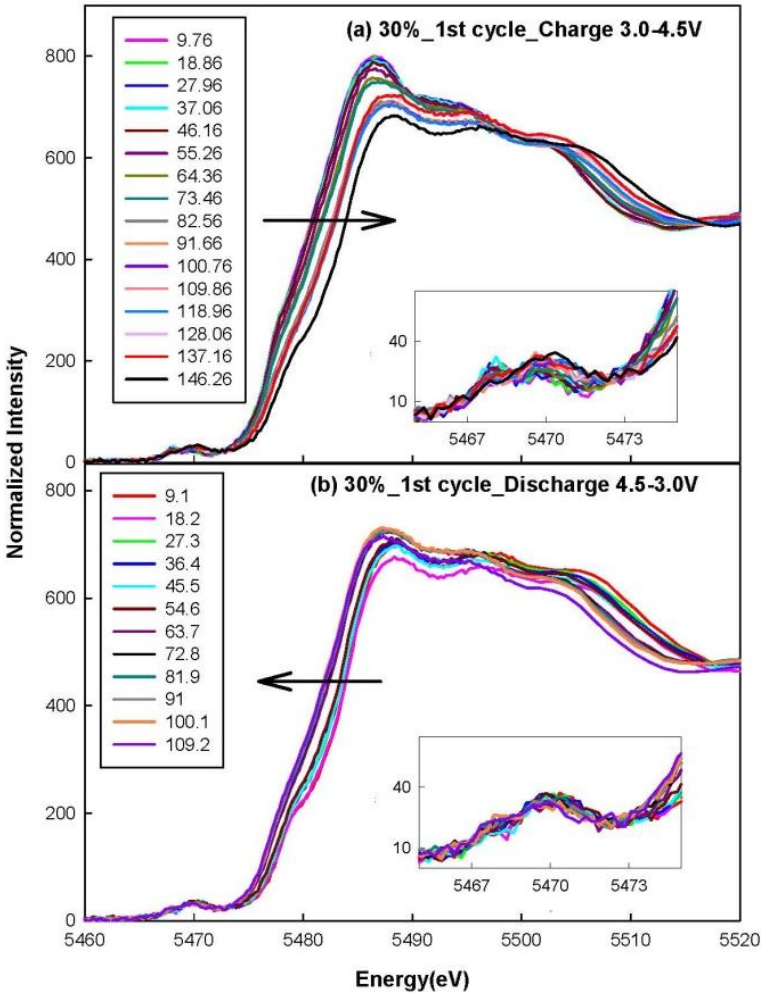

Figure 5.5 V-K edge XANES during charge/discharge for 0.1C cycling in 30% Mg-doped system: (a) 1st cycle charge 3.0 → 4.5 V, (b) 1st cycle discharge 4.5 → 3.0 V

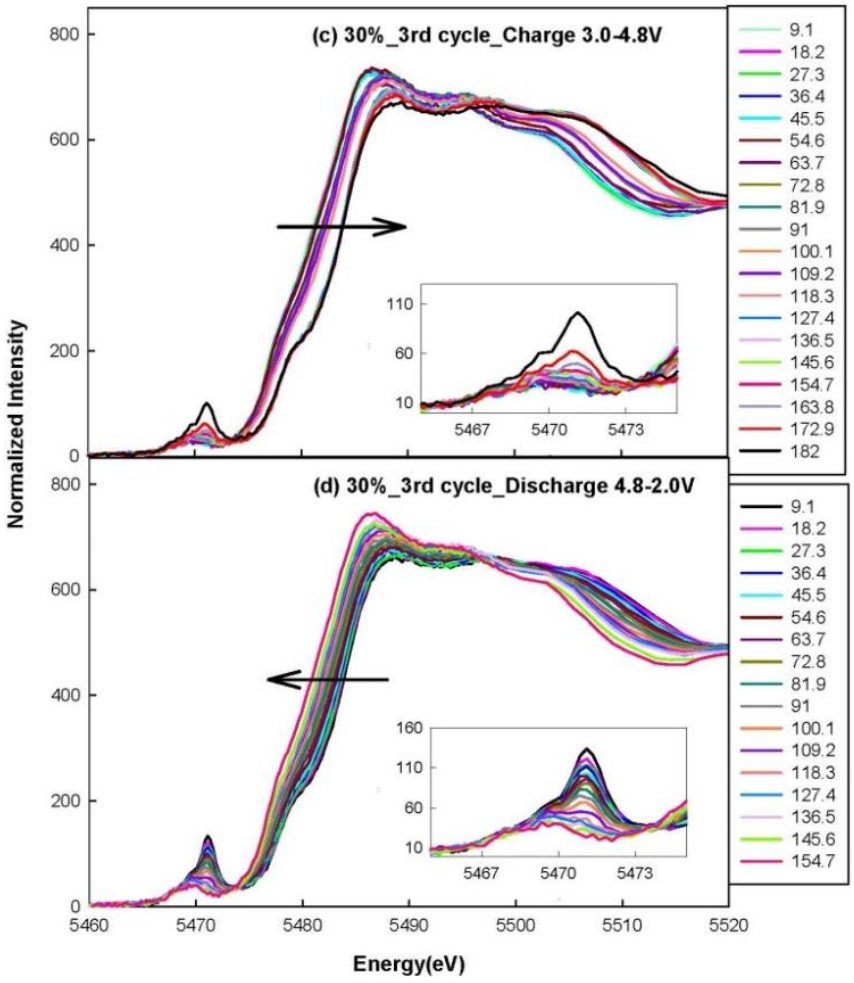

Figure 5.6 V-K edge XANES during charge/discharge for 0.1C cycling in 30% Mg-doped system: (c) 2nd cycle charge 3.0 → 4.8 V, (d) 2nd cycle discharge 4.8 → 2.0 V, y- axis scale between 0-160.

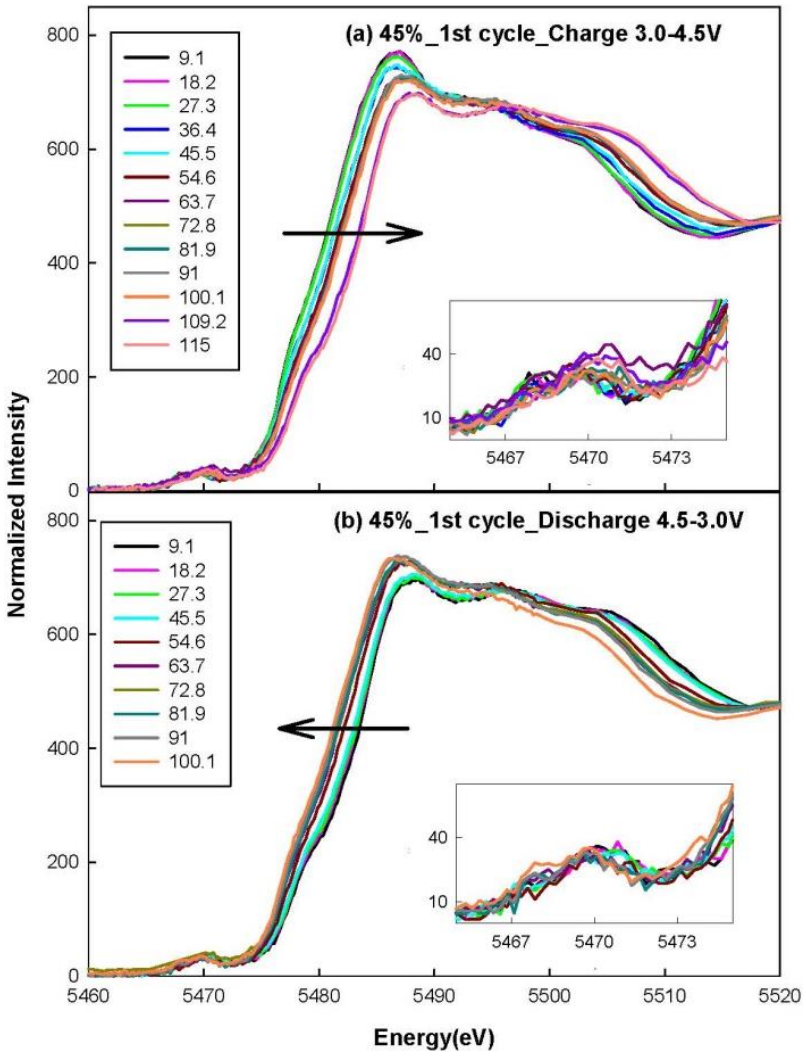

Figure 5.7 V-K edge XANES during charge/discharge for 0.1C cycling in 45% Mg-doped system: (a) 1st cycle charge 3.0 → 4.5 V, (b) 1st cycle discharge 4.5 → 3.0 V

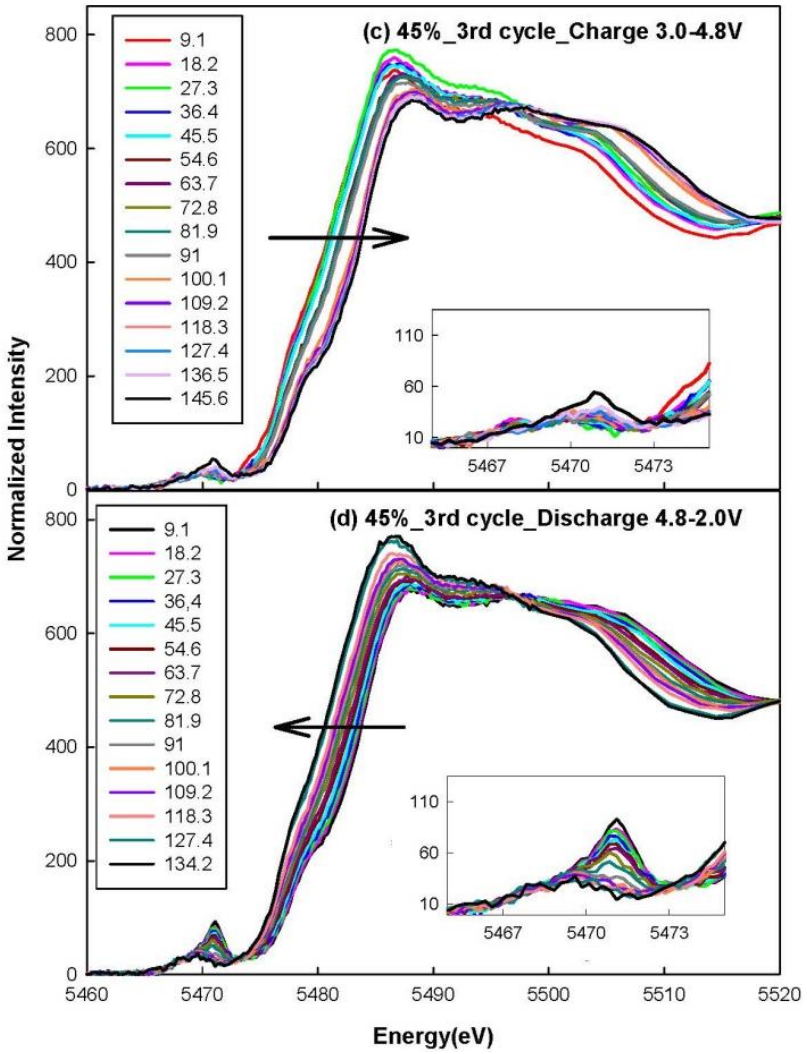

Figure 5.8 V-K edge XANES during charge/discharge for 0.1C cycling in 45% Mg-doped system: (c) 2nd cycle charge 3.0 → 4.8 V, (d) 2nd cycle discharge 4.8 → 2.0 V

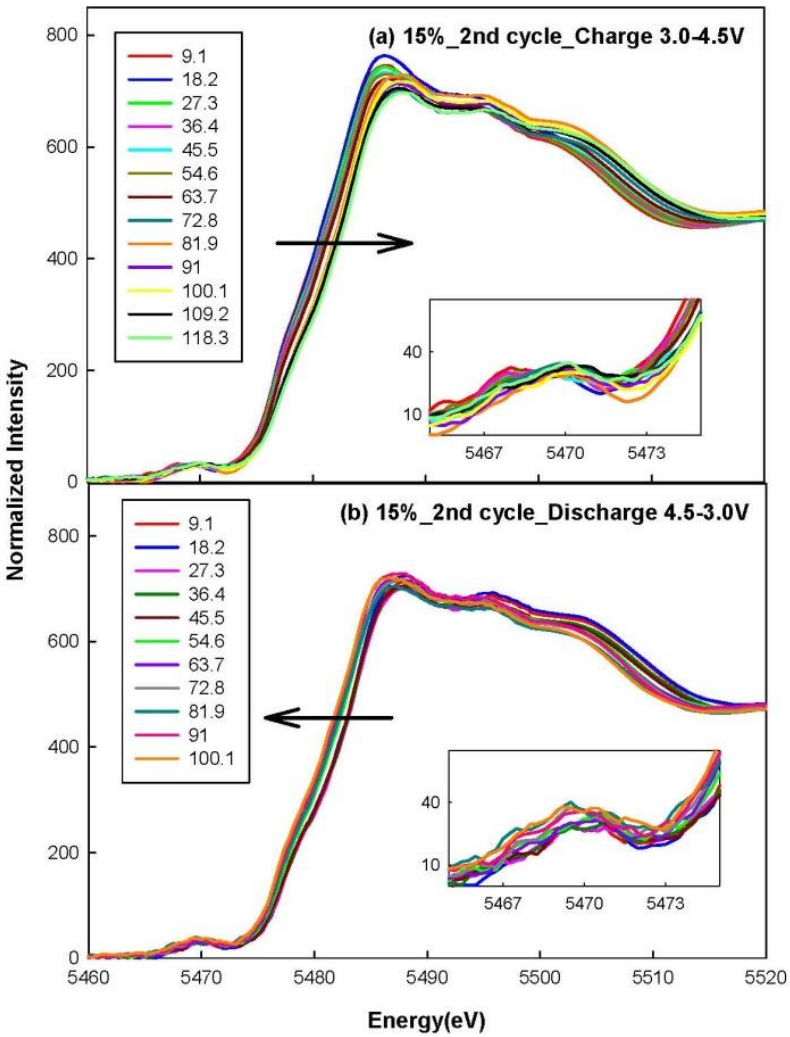

Figure 5.9 V-K edge XANES during charge/discharge for 0.1C cycling in 15% Mg-doped system: (a) 2nd cycle charge 3.0 → 4.5 V, (b) 2nd cycle discharge 4.5 → 3.0 V

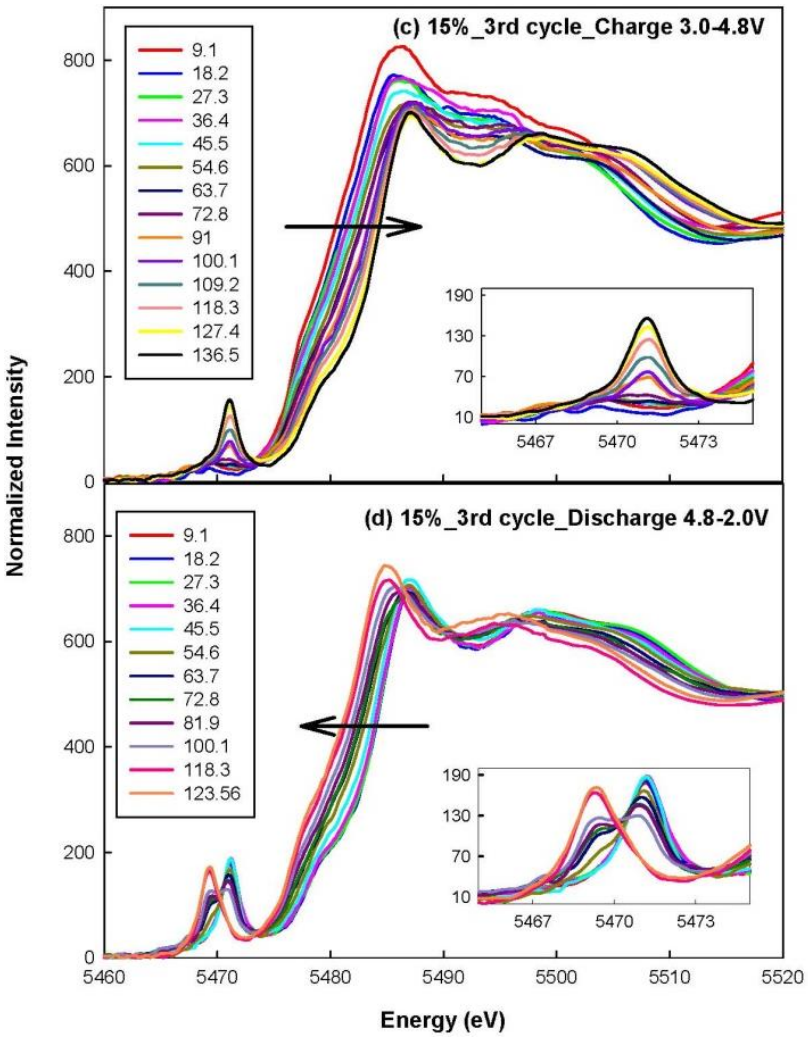

Figure 5.10 V-K edge XANES during charge/discharge for 0.1C cycling in 15% Mg-doped system: (c) 3rd cycle charge 3.0 → 4.8 V, (d) 3rd cycle discharge 4.8 → 2.0 V, y- axis scale between 0-200.

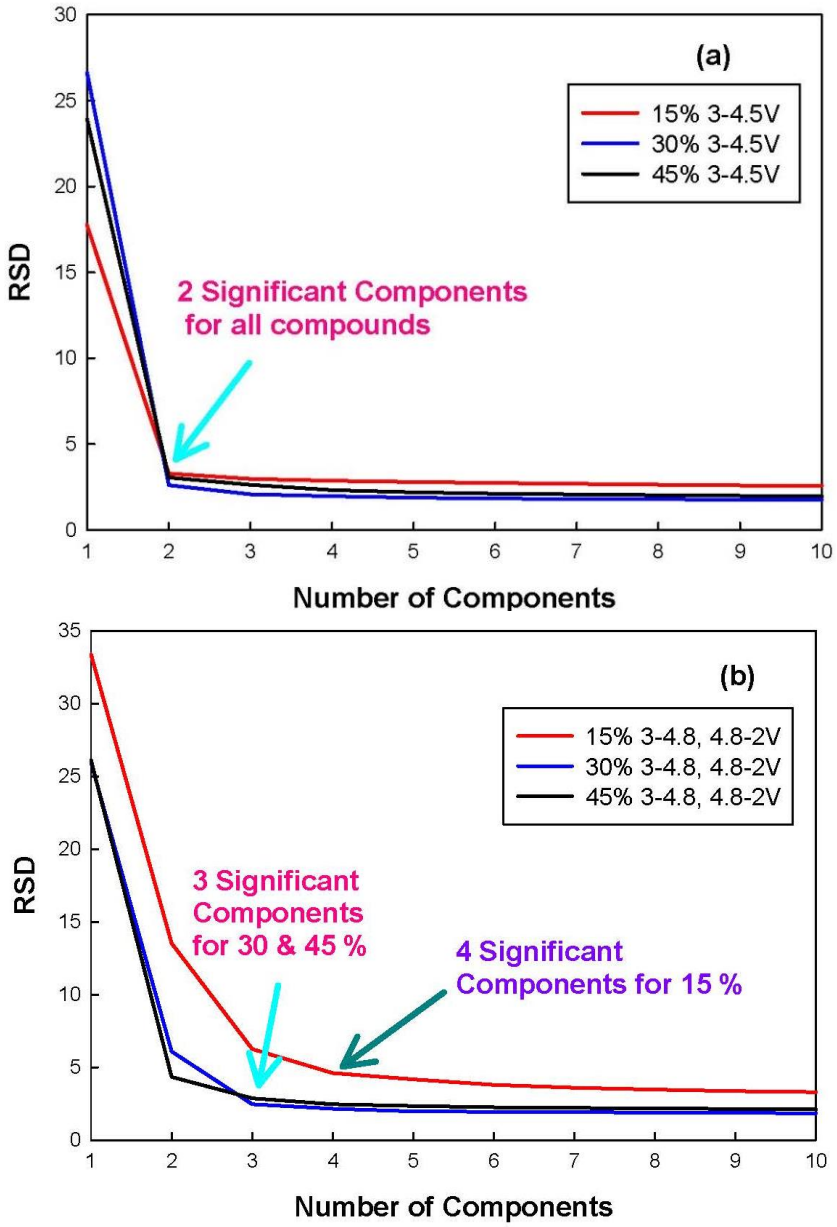

Figure 5.11 The Residual Standard Deviation plot showing the maximum number of principal components needed in the PCA analysis for the all 3 (15 %, 30 %, and 45 %) systems. (a) 3.0 ⇌ 4.5 V charge discharge cycle (b) 3.0 → 4.8 V (charge) & 4.8 → 2.0 V (discharge). The arrows show the number of components required during cycling.

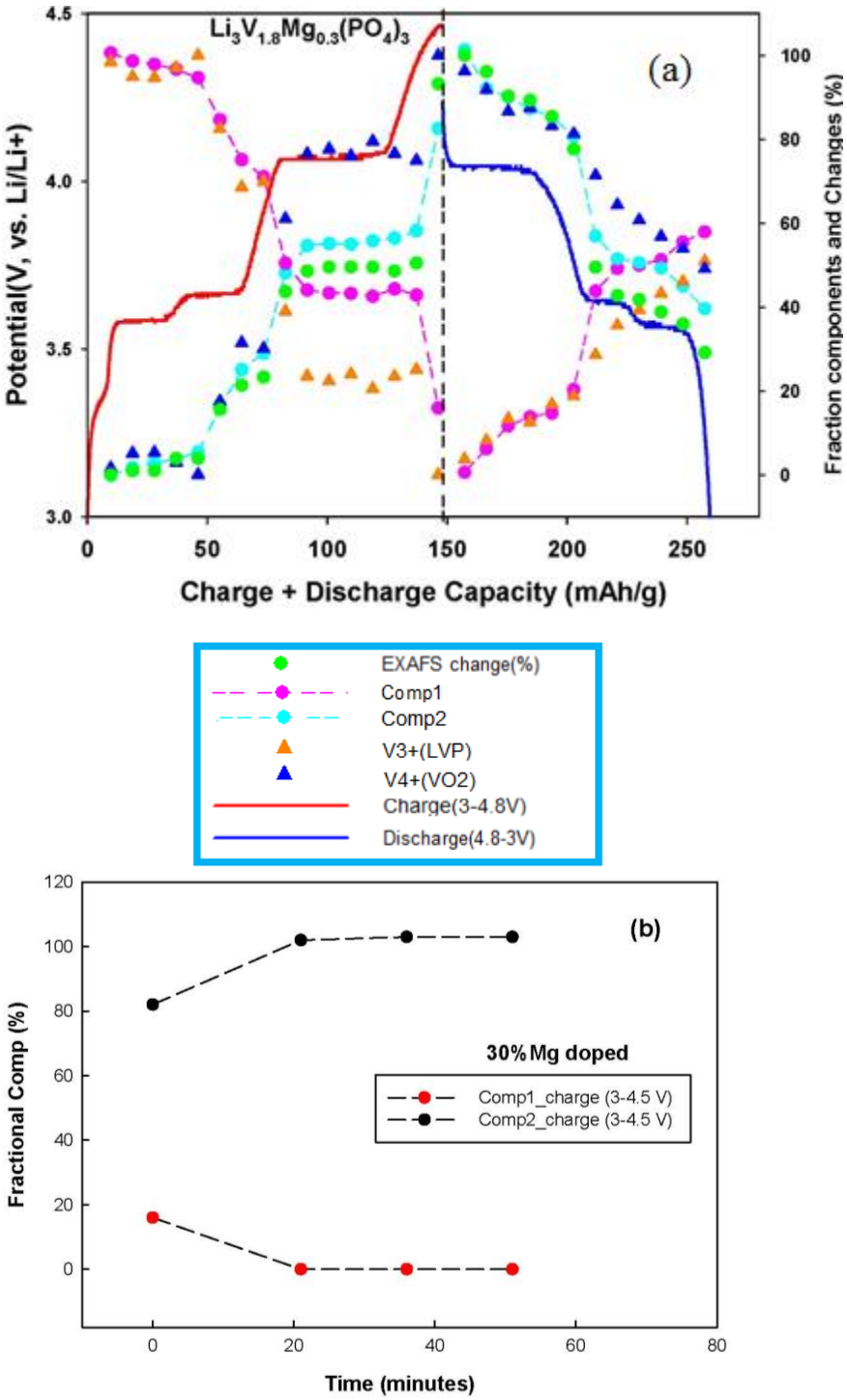

Figure 5.12 (a) 30% Mg-doped LVP, PCA components fractional fit and fit with 2 model compounds such as $Li_3V_2(PO_4)_3$ (V^{3+}), and VO_2 (V^{4+}), 0.1C rate 1st charge/discharge profile while cycling, (b) results for extra XANES spectra measured during equilibration time.

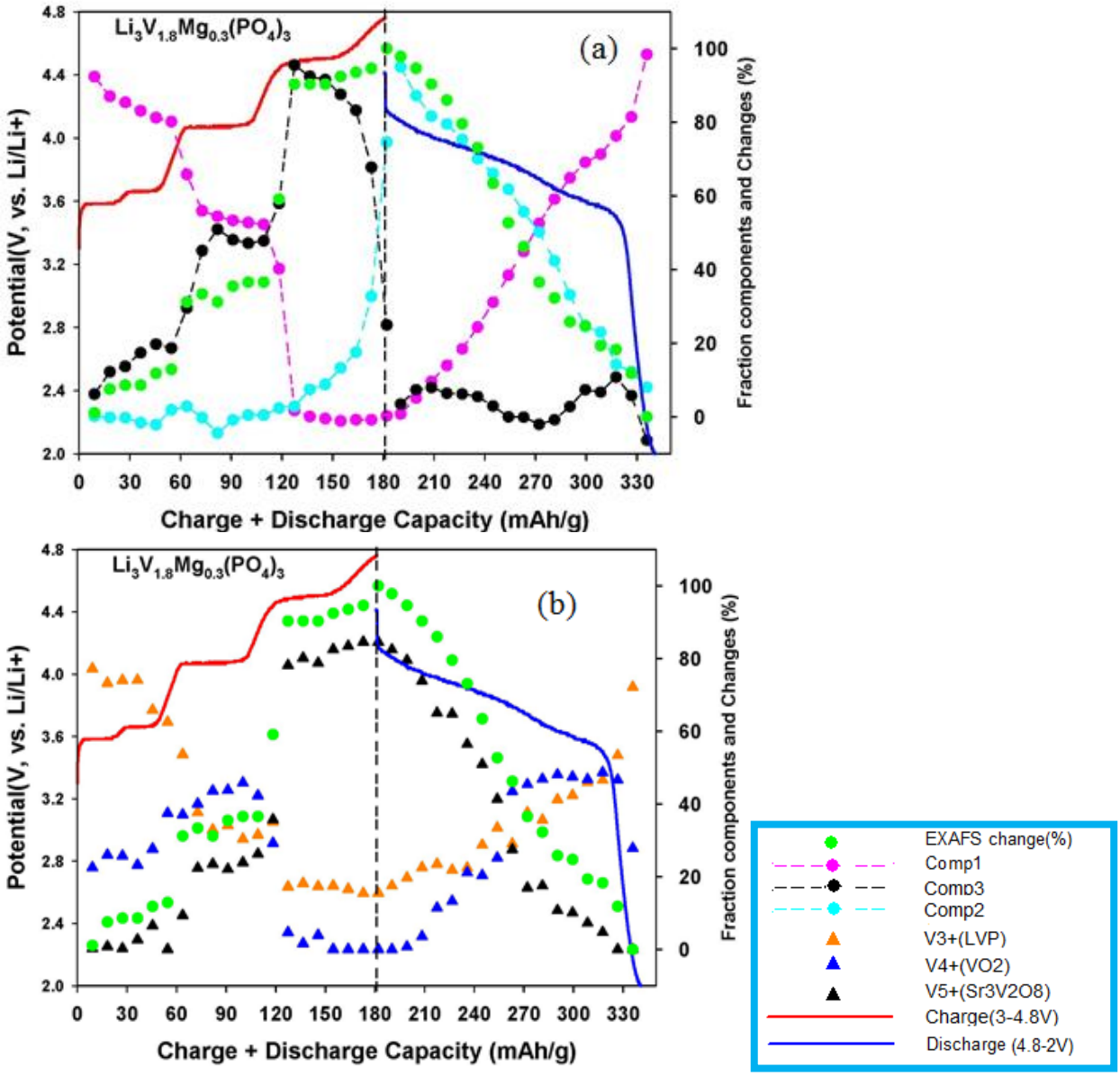

Figure 5.13 30% Mg-doped LVP, (a) PCA components fit; (b) fit with model compounds LVP(V^{3+}), VO_2 (V^{4+}), and $Sr_3V_2O_8$ (V^{5+}))

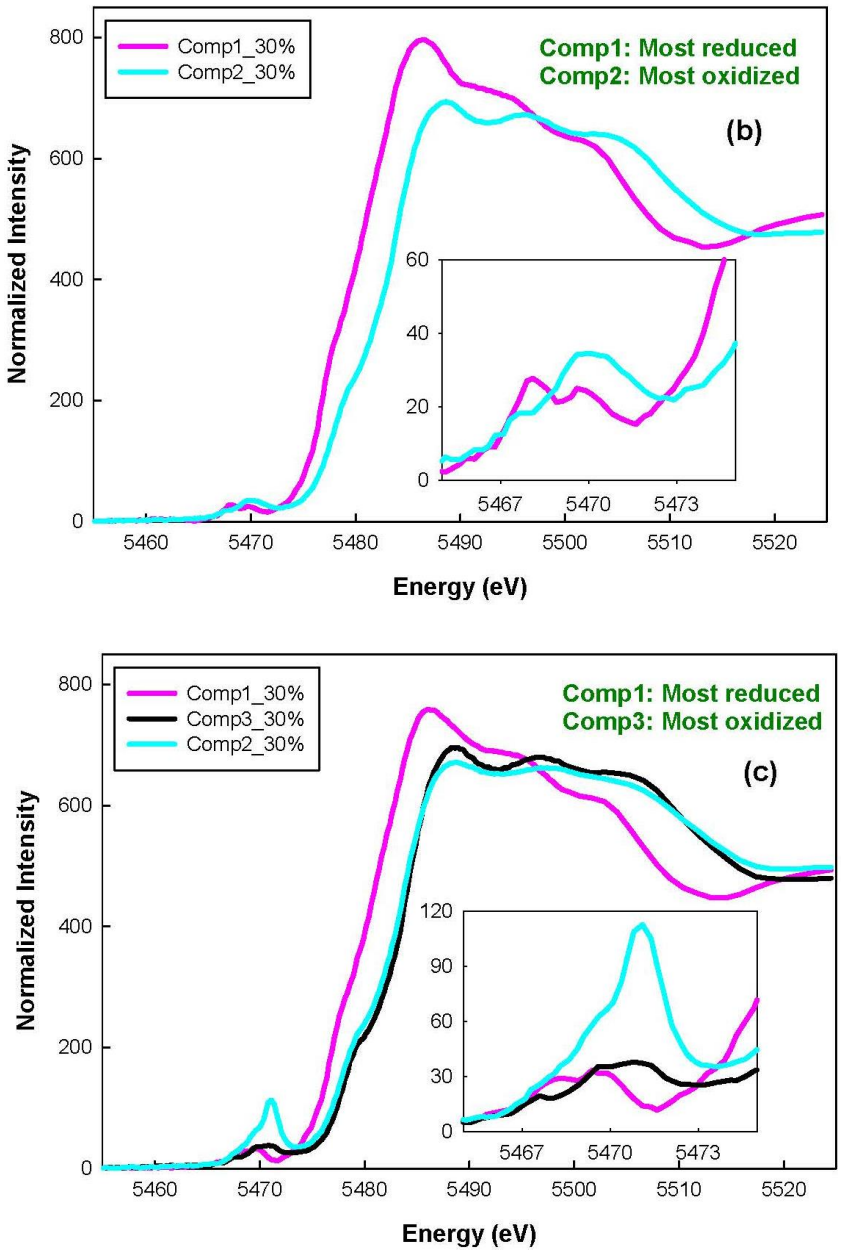

Figure 5.14 30% Mg-doped LVP; (b) fit of 2 PCA components between 3.0 ⇌ 4.5 V; (c) fit of 3 PCA components (3.0 →4.8 V/4.8 →2.0 V)

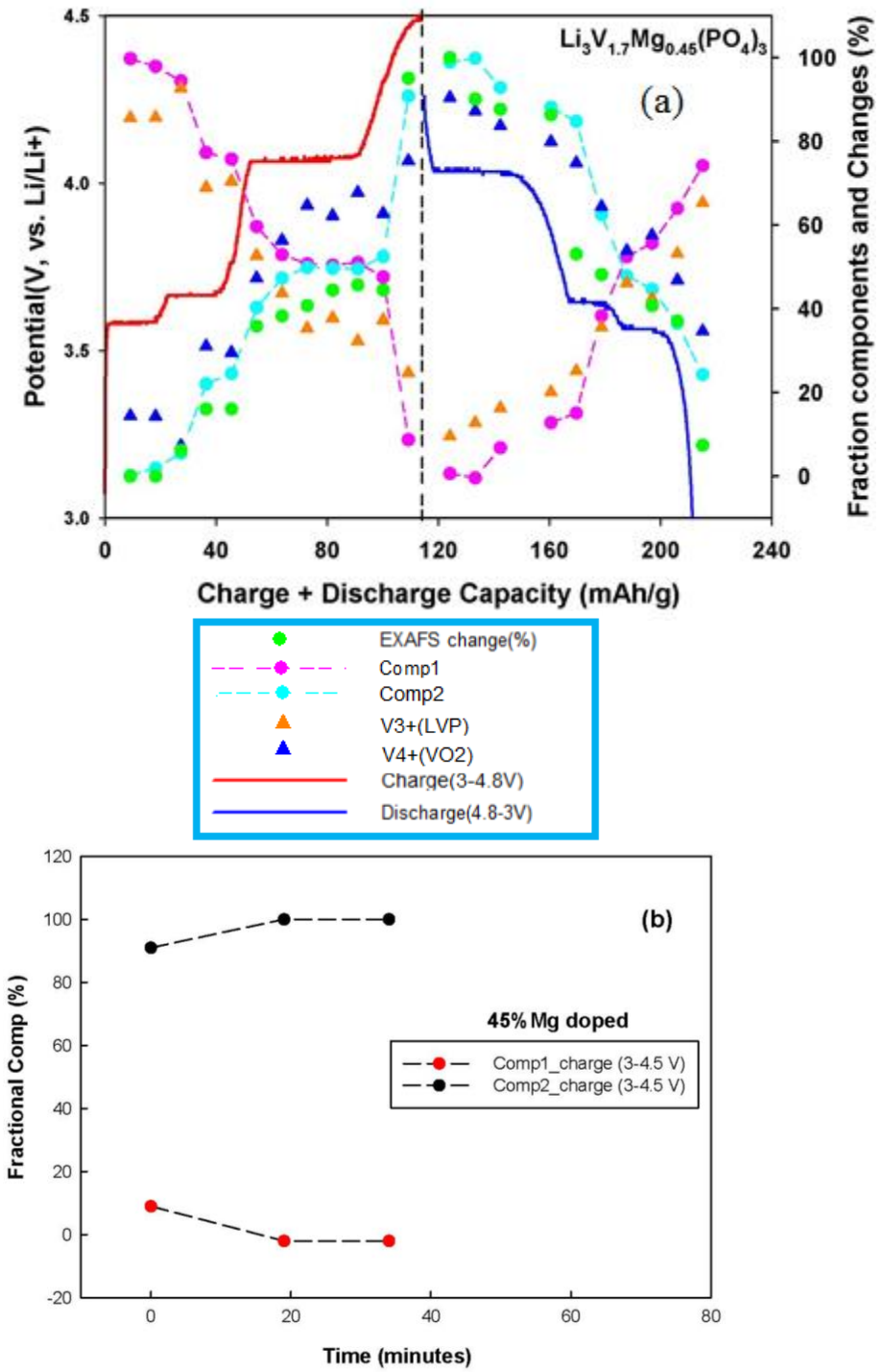

Figure 5.15 (a) 45% Mg-doped LVP, PCA components fractional fit and fit with 2 model compounds such as $Li_3V_2(PO_4)_3$ (V^{3+}), and VO_2 (V^{4+}), 0.1C rate 1st charge/discharge profile while cycling, (b) results for extra XANES spectra measured during equilibration time.

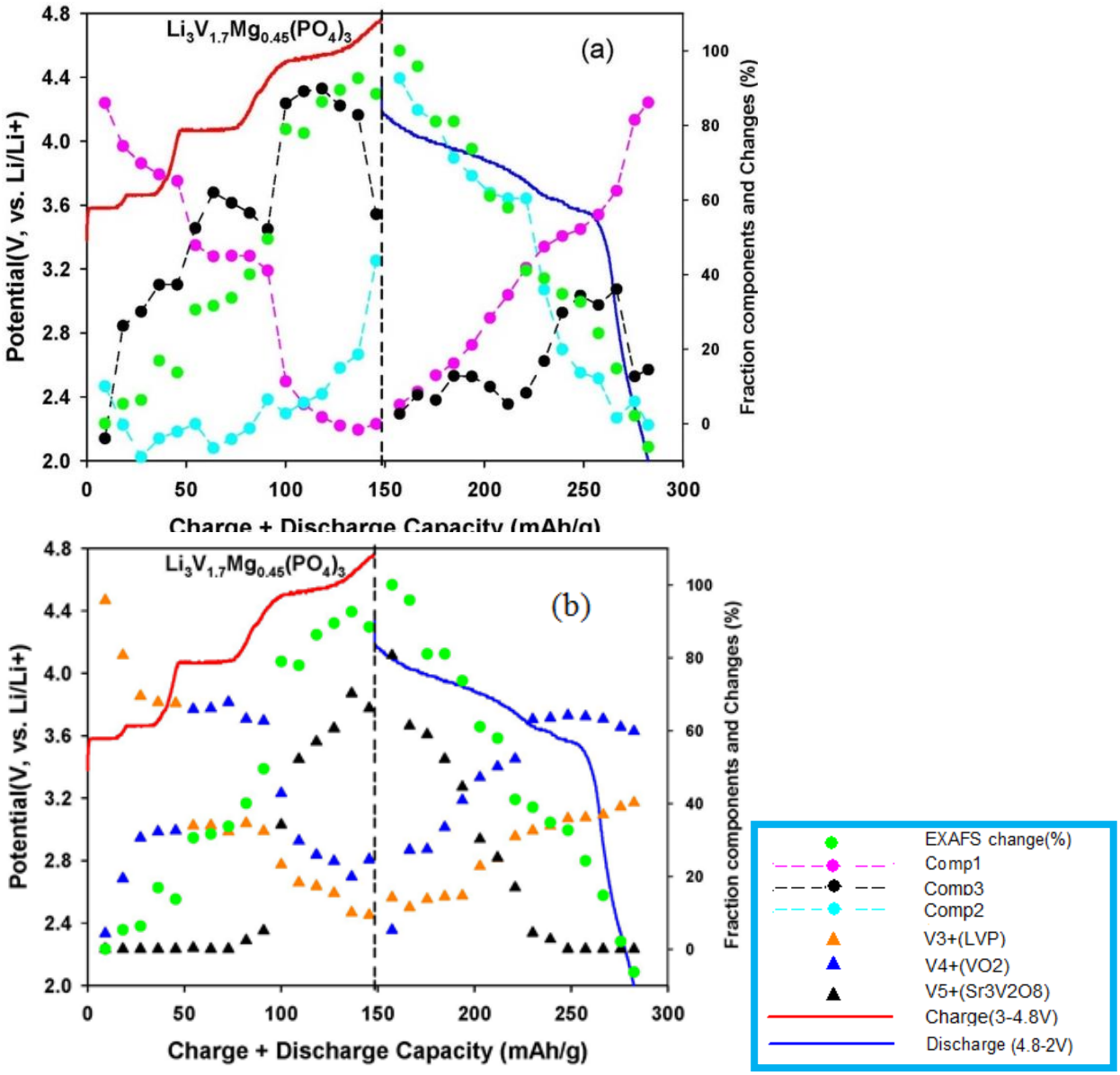

Figure 5.16 45% Mg-doped LVP, (a) PCA components fit (b) fit with model compounds LVP(V^{3+}), VO_2 (V^{4+}), and $Sr_3V_2O_8$ (V^{5+}))

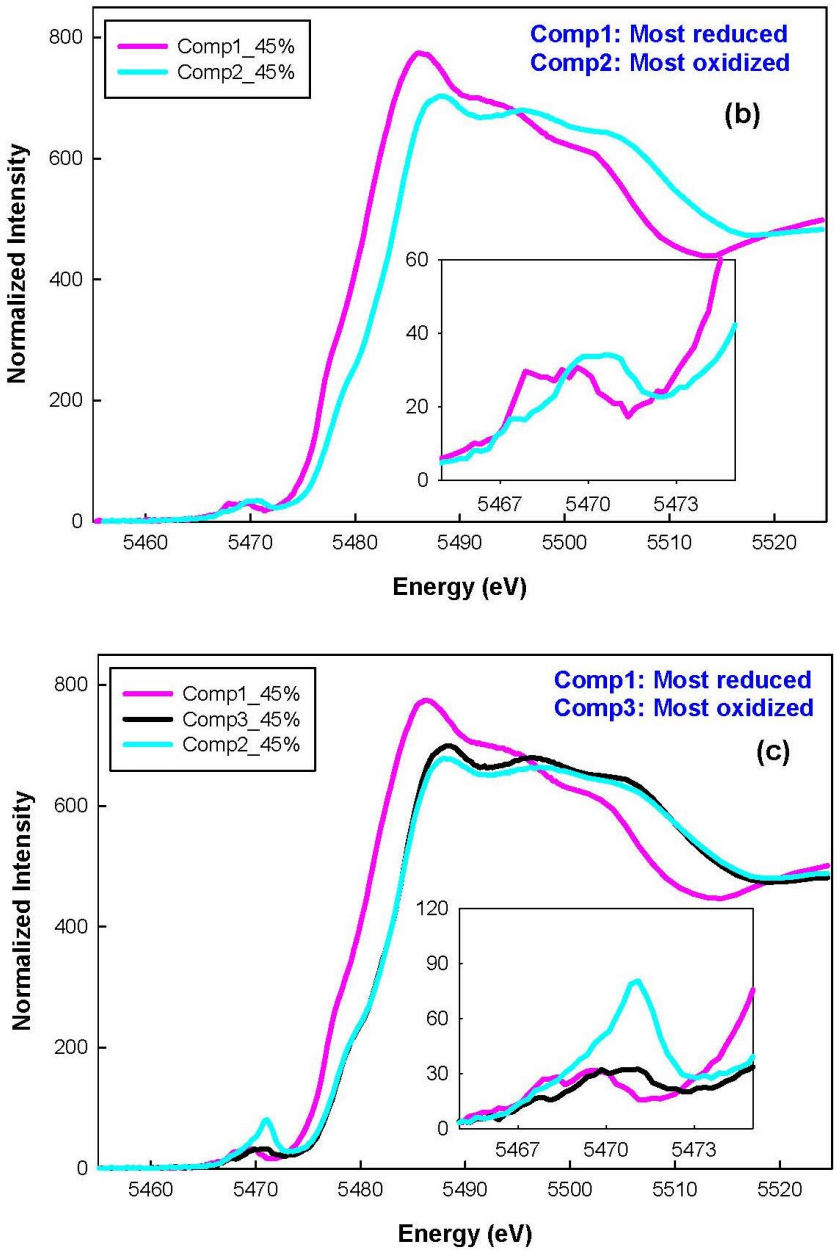

Figure 5.17 45% Mg-doped LVP; (b) fit of 2 PCA components between 3.0 ⇌ 4.5 V; (c) fit of 3 PCA components (3.0 →4.8 V/4.8 →2.0 V)

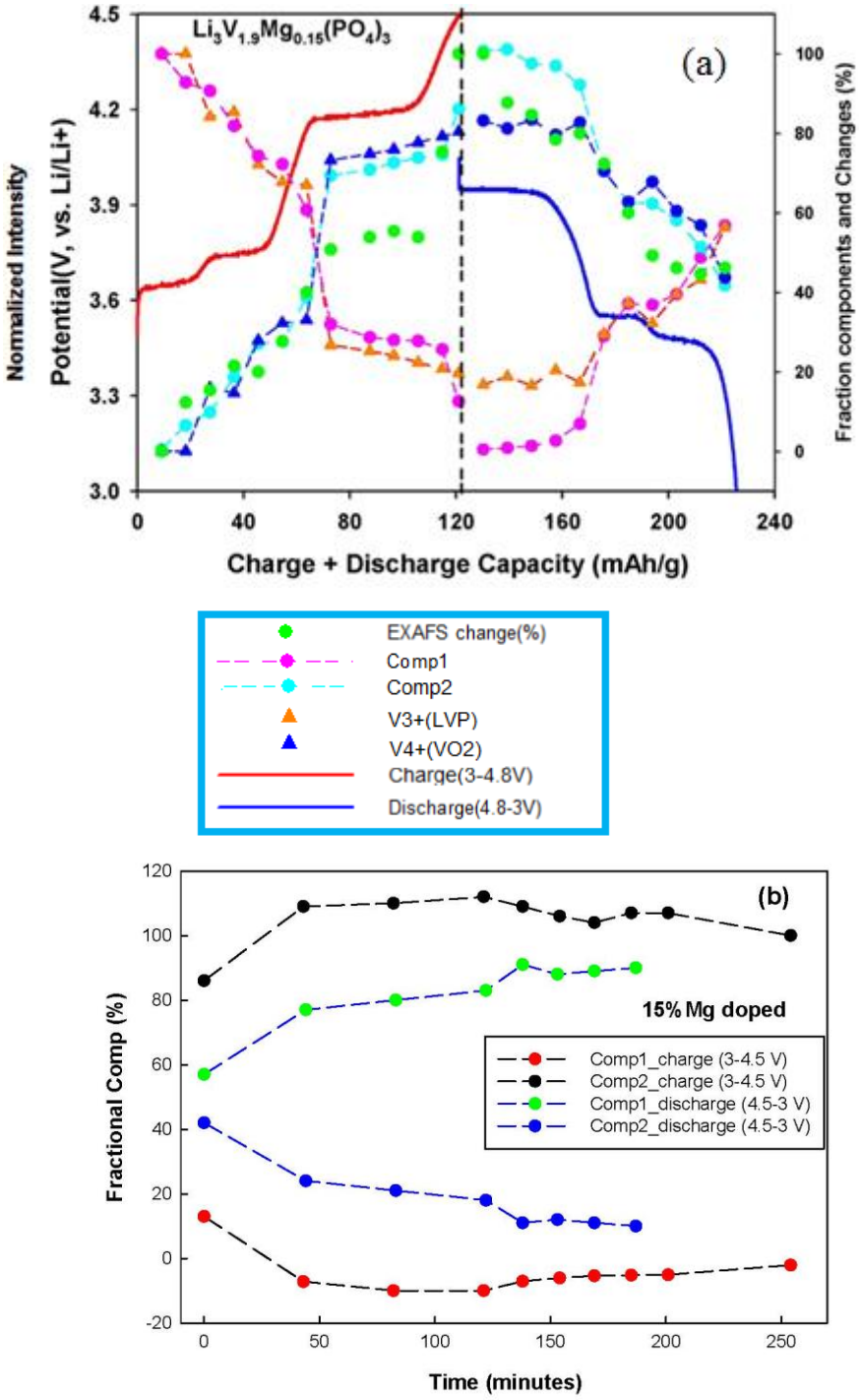

Figure 5.18 (a) 15% Mg-doped LVP, PCA components fractional fit and fit with 2 model compounds such as $Li_3V_2(PO_4)_3$ (V^{3+}), and VO_2 (V^{4+}), 0.1C rate 2nd charge/discharge profile while cycling, (b) results for extra XANES spectra measured during equilibration time.

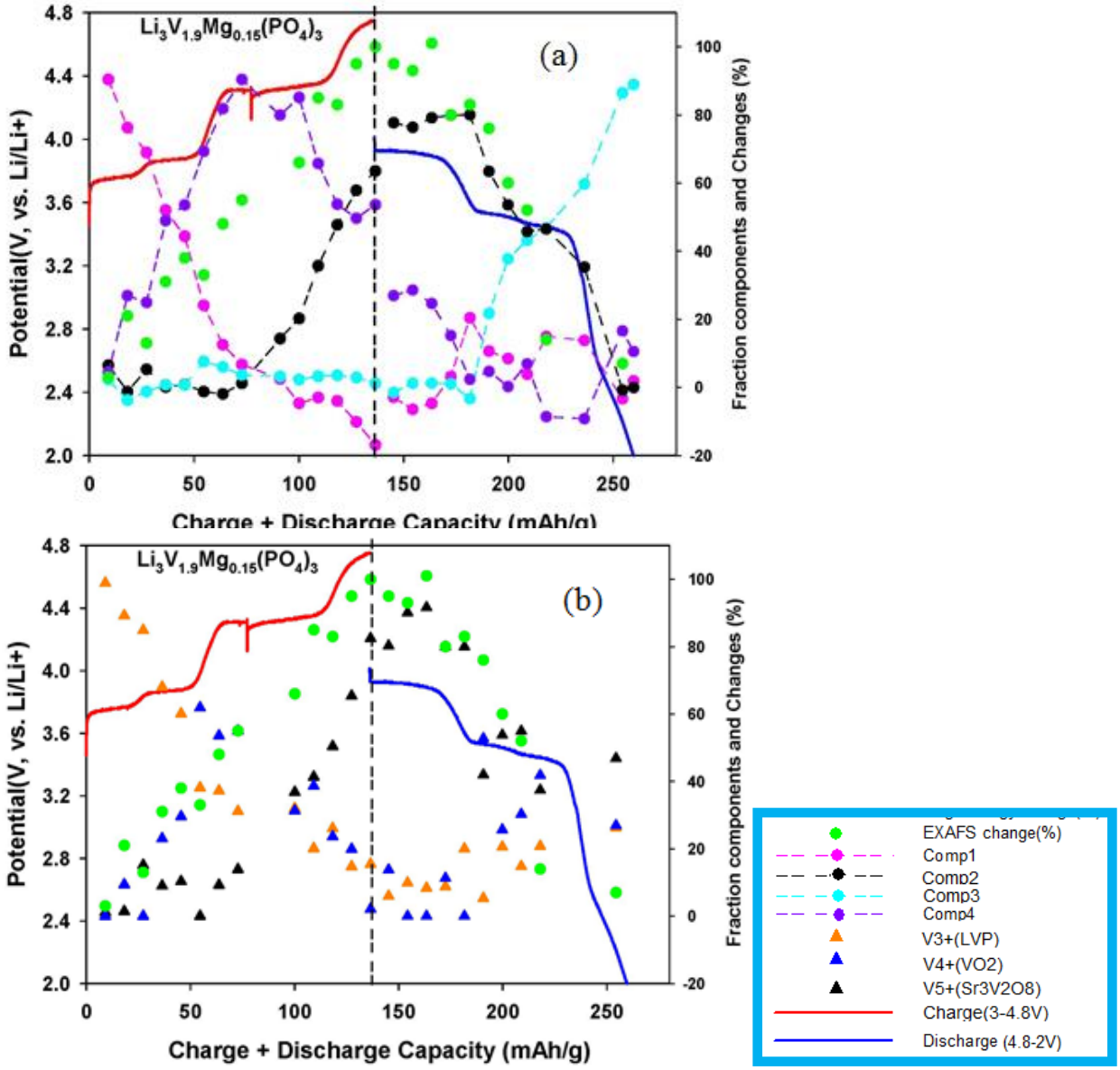

Figure 5.19 15% Mg-doped LVP, (a) PCA components fit (b) fit with model compounds LVP(V^{3+}), VO_2 (V^{4+}), and $Sr_3V_2O_8$ (V^{5+}))

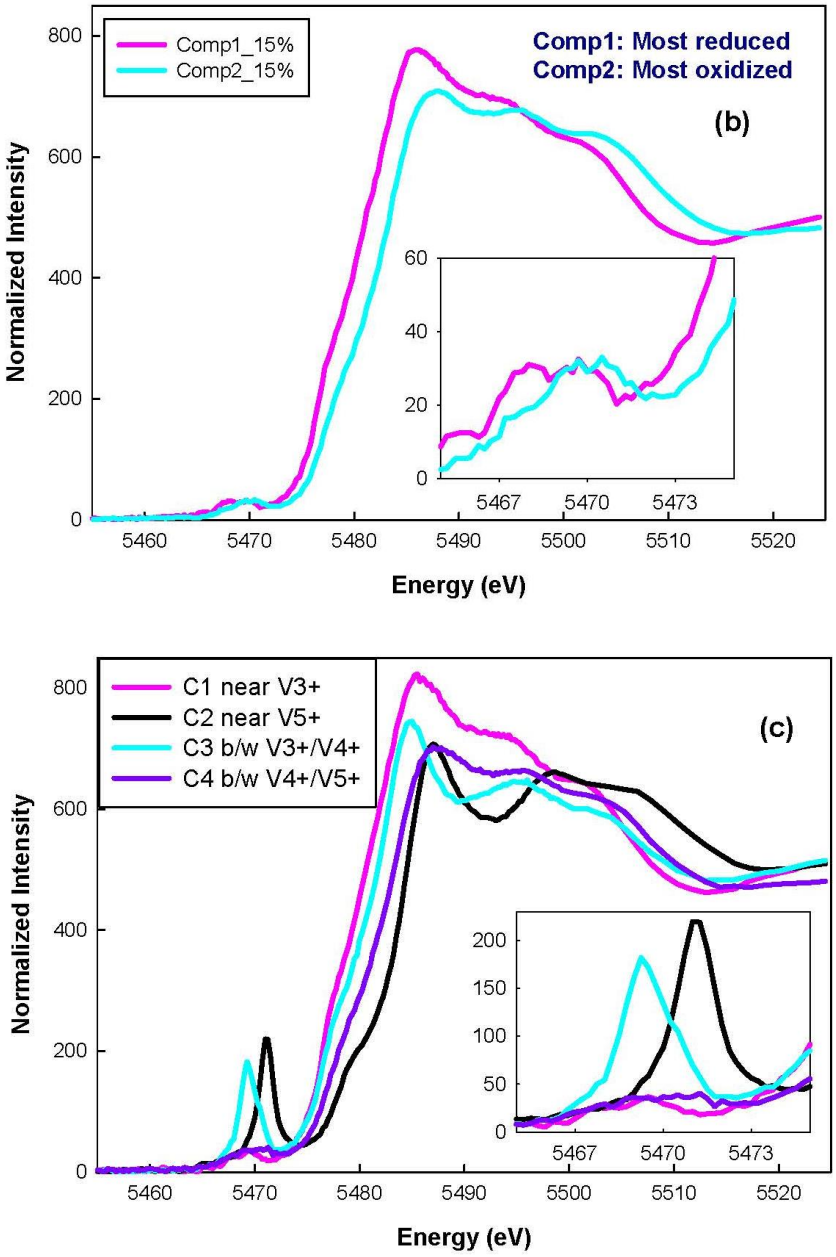

Figure 5.20 15% Mg-doped LVP, (b) fit of 2 PCA components between 3.0 ⇌ 4.5 V. (c) fit of 3 PCA components (3.0 →4.8 V/4.8 →2.0 V)

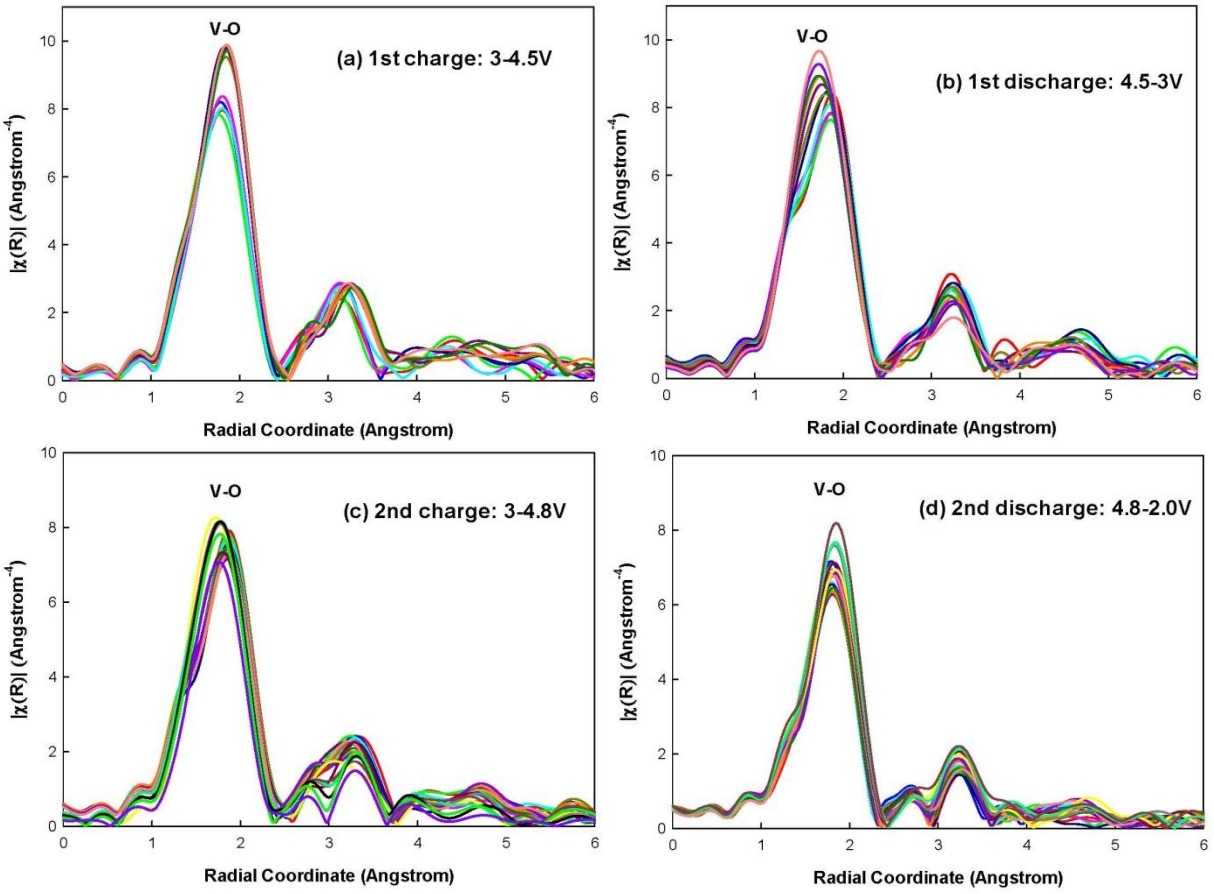

Figure 5.21 V– K edge k^3 -weighted Fourier transform for 30% doped LVP.

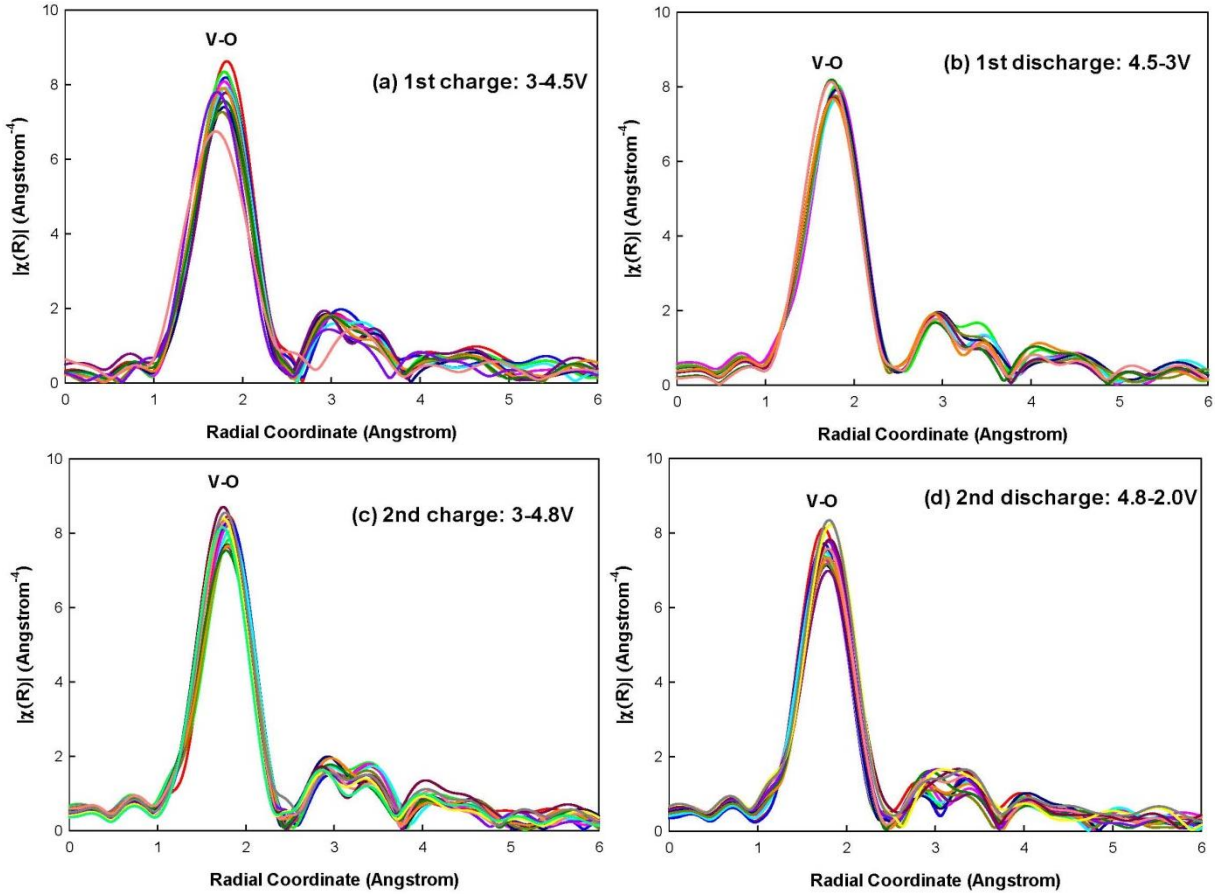

Figure 5.22 V– K edge k^3 -weighted Fourier transform for 45% doped LVP.

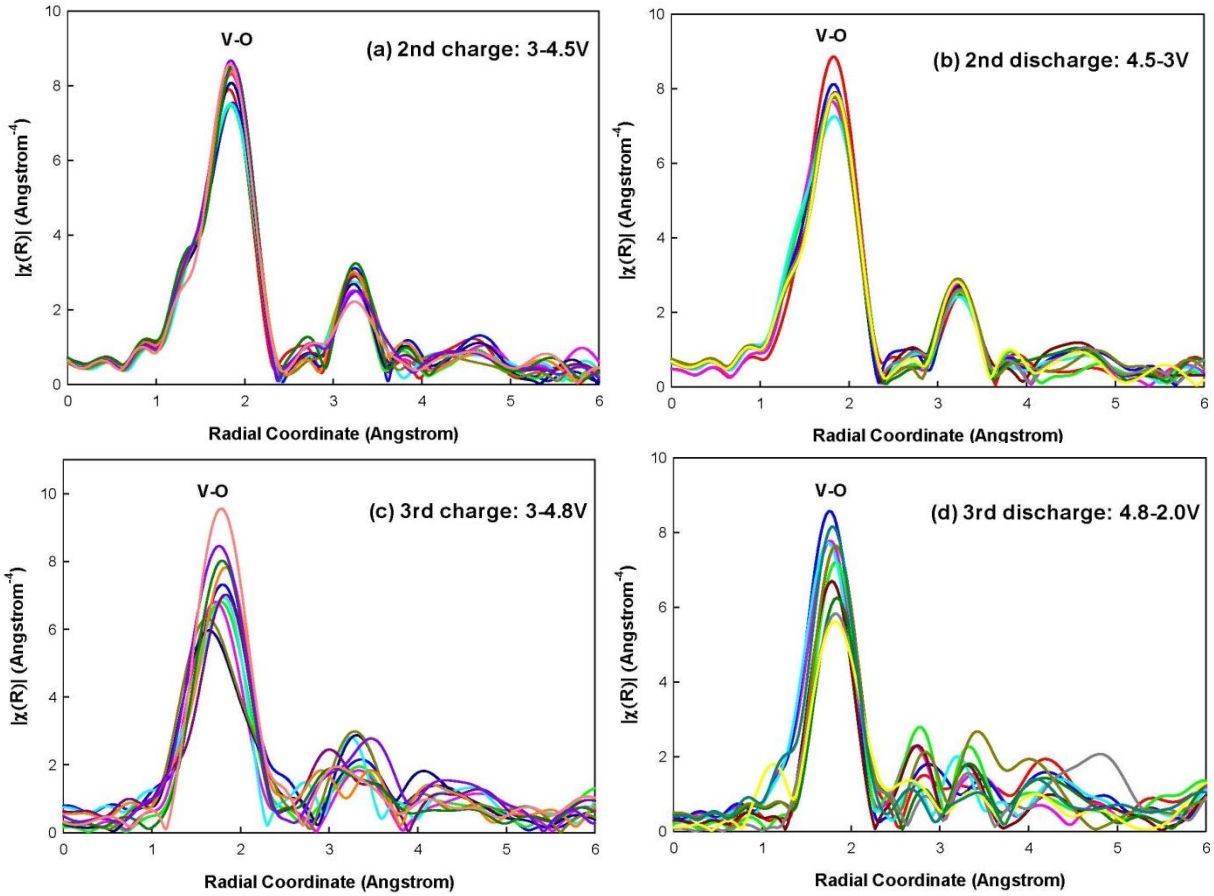

Figure 5.23 V– K edge k^3 -weighted Fourier transform for 15% doped LVP.

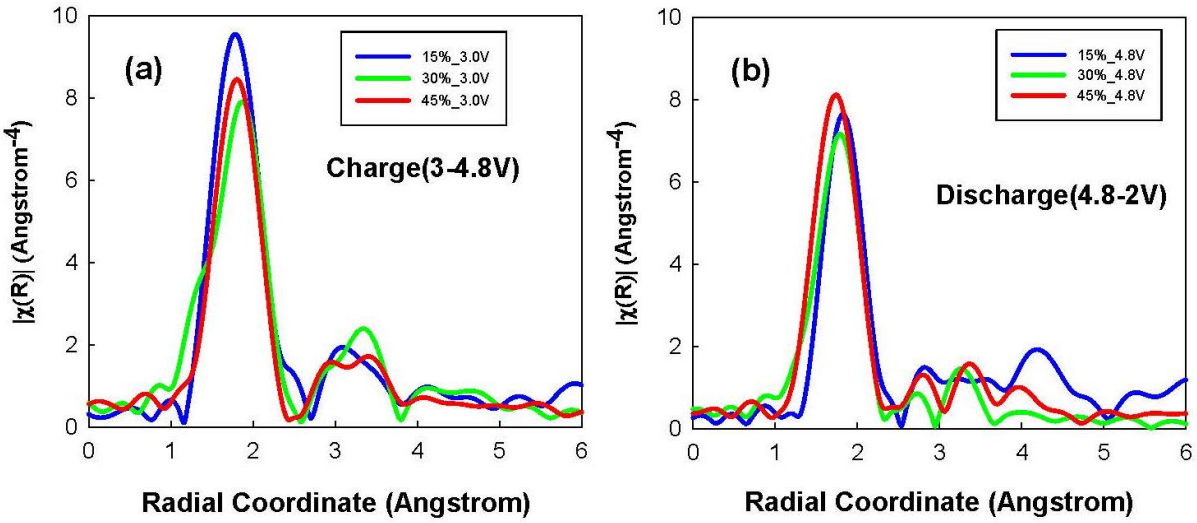

Figure 5.24 V– K edge k^3 -weighted Fourier transform comparison at specific voltage; (a) at 3.0 V, and (b) 4.8 V

Table 5.1 (a) Edge energy change for each individual cycle (b) Summary of the V charge compensation obtained at the end of each charge and discharge cycle from the least squares model fit after performing the PCA analysis. For a detailed charge compensation mechanism per each cycle, see **Figures 5.5 - 5.10**

% Mg-doped	(a) **Edge Δ E**							
	Charge(3.0-4.5)		**Discharge(4.5-3.0)**		**Charge(3.0-4.8)**		**Discharge(4.8-2.0)**	
15%	2nd	2.00 eV	2nd	1.30 eV	3rd	2.6 eV	3rd	2.5 eV
30%	1st	2.39 eV	1st	1.88 eV	2nd	2.9 eV	2nd	3.0 eV
45%	1st	2.45 eV	1st	1.97 eV	2nd	3.0 eV	2nd	2.8 eV
% Mg-doped	(b) **Vanadium Valence Change**							
	Charge(3.0-4.5)		**Discharge(4.5-3.0)**		**Charge(3.0-4.8)**		**Discharge(4.8-2.0)**	
15%	2nd	3.0→3.8	2nd	3.83→3.4	3rd	3.1→4.86	3rd	4.77→4.13
30%	1st	3.0→4	1st	3.95→3.49	2nd	3.23→4.68	2nd	4.65→3.28
45%	1st	3.08→4	1st	3.9→3.35	2nd	3.02→4.56	2nd	4.64→3.59

Table 5.2 The change in the average V-O nearest neighbor distances observed during charge/discharge cycling for all three systems during 3.0 ⇌4.5 V and 3.0 → 4.8 V, 4.8 → 2.0 V. For the charge cycle the values represent the decrease of the V-O bond distance, and for discharge cycle it represents the increase of the V-O bond distance.

EXAFS	V-O Distance (Å)			
	Charge(3.0-4.5)	Discharge(4.5-3.0)	Charge(3.0-4.8)	Discharge(4.8-2.0)
15%	0.065	0.060	0.097	0.084
30%	0.090	0.073	0.092	0.091
45%	0.077	0.075	0.088	0.097

5.5 REFERENCES

(1) Chung, S. Y.; Bloking, J. T.; Chiang, Y. M. *Nat Mater* 2002, *1*, 123.

(2) Chung, S. Y.; Blocking, J. T.; Andersson, A. S.; Chiang, Y. M. *Solid State Ionics: Trends in the New Millennium, Proceedings* 2002, 85.

(3) Yin, S. C.; Grondey, H.; Strobel, P.; Anne, M.; Nazar, L. F. *J Am Chem Soc* 2003, *125*, 10402.

(4) Yin, S. C.; Grondey, H.; Strobel, P.; Huang, H.; Nazar, L. F. *J Am Chem Soc* 2003, *125*, 326.

(5) Wang, D. Y.; Buqa, H.; Crouzet, M.; Deghenghi, G.; Drezen, T.; Exnar, I.; Kwon, N. H.; Miners, J. H.; Poletto, L.; Graetzel, M. *J Power Sources* 2009, *189*, 624.

(6) Zhou, F.; Cococcioni, M.; Kang, K.; Ceder, G. *Electrochem Commun* 2004, *6*, 1144.

(7) Wang, L.; Zhang, L. C.; Lieberwirth, I.; Xu, H. W.; Chen, C. H. *Electrochem Commun* 2010, *12*, 52.

(8) Huang, H.; Faulkner, T.; Barker, J.; Saidi, M. Y. *J Power Sources* 2009, *189*, 748.

(9) Gaubicher, J.; Wurm, C.; Goward, G.; Masquelier, C.; Nazar, L. *Chem Mater* 2000, *12*, 3240.

(10) Sato, M.; Ohkawa, H.; Yoshida, K.; Saito, M.; Uematsu, K.; Toda, K. *Solid State Ionics* 2000, *135*, 137.

(11) Huang, J. S.; Yang, L.; Liu, K. Y.; Tang, Y. F. *J Power Sources* 2010, *195*, 5013.

(12) Manceau, A.; Marcus, M.; Lenoir, T. *J Synchrotron Radiat* 2014, *21*, 1140.

(13) Fu, P.; Zhao, Y. M.; Dong, Y. Z.; An, X. N.; Shen, G. P. *J Power Sources* 2006, *162*, 651.

(14) Patoux, S.; Sannier, L.; Lignier, H.; Reynier, Y.; Bourbon, C.; Jouanneau, S.; Le Cras, F.; Martinet, S. *Electrochim Acta* 2008, *53*, 4137.

CHAPTER VI

CONCLUSION AND FUTURE WORK

6.1 CONCLUSION

This dissertation has focused on providing new information about existing anode and cathode materials for Li-ion battery characterization that relies on synchrotron-based X-ray Absorption Spectroscopy. Although lithium ion battery materials have been studied extensively and the materials that have been discussed in this dissertation are not new, we have shown that careful application of *in-situ* XAS can nevertheless provide new insight. For example, previous neutron diffraction studies of lithium titanate showed that the Li ions move as Ti is reduced. Our data showed that the Ti-O distance increases without an increase in the Ti-Ti distance, an increase made possible by the Li distortion. Results in this dissertation support the previous studies, and careful comparison of Ti-O and Ti-Ti suggest an explanation for the zero-strain behavior. Detailed, careful analysis for lithium manganese oxide revealed minor changes in Mn structure that are consistent with a small oxidation state change. For lithium vanadium phosphate, *in-situ* XAS studies revealed unexpected non-linearities in the XANES that had been missed in earlier XAS studies, and demonstrated kinetic effects that had been missed in earlier diffraction studies. Our data demonstrate that well-behaved electrochemistry alone is not sufficient to conclude that the sample is homogeneous. Finally, the XAS data provided suggest an atomic-level explanation for the change in behavior above 4.5 V that was quite different from

the explanation proposed based on neutron diffraction of chemically prepared samples. In each case, our ability to provide new insight relied on careful analysis of the XAS and, in most cases, the use of *in-situ* measurements to characterize functioning electrodes.

6.2 FUTURE WORK

Further research applying *in-situ* X-ray techniques to newly invented materials and/or composition modification in existing electrode system will continuously provide suggestions for future battery optimization. The theoretical capacity for $Li_3V_2(PO_4)_3$ is 197 mAh/g which is quite low, when compared to layered structure $LiCoO_2$ of 272 mAh/g. Co is not a preferred atom in electrode materials, finding alternatives with high capacity is necessary. One example would be Li-rich and Mn-rich compounds, such as $Li[Li_xMn_{(1-x-2y)}Co_yNi_y]O_2$ and $LiMn_{1.5}Ni_{0.5}O_4$. These two compounds show high voltage, 4.7 V and a quite high discharge capacity, 250 mAh/g. Thus, these materials have an energy density much higher than other reported cathode oxides. Another example would be material such as polyoxyanion cathodes based on the orthosilicates, Li_2FeSiO_4 (theoretical capacity of 320 mAh/g) and Li_2MnSiO_4, which have recently received a great deal of attention from battery research. Iron silicate, Li_2FeSiO_4 is especially promising because of its high capacity (theoretical capacity of 320 mAh/g and discharge capacity of 250 mAh/g) and because of the low cost and high abundance of, iron and silicon. Therefore, this material has potential for the preparation of cheap and safe cathodes. In addition, applying XAS technique to the above materials will give detailed ideas of changes happening in the structural geometry and chemical reactions. Therefore, these are promising cathode candidates for high-energy density

Li-ion batteries in EV applications. In addition, applying *in-situ* XAS technique to these materials will provide a better understanding of the chemical reactions and structural changes happening in the material while cycling.

One of the well-known limitations of XAS technique is that it gives only an averaged distance of short range (1-3 Å) order. Therefore, in order to provide a detailed analysis of both short and long range structural evolution during the cycling, a combination of *in-situ* XAS and *in-situ* XRD would be desirable. This would provide the average unit cell in addition to the average distances of the central atom to the nearest neighboring atom. The addition of imaging capability using X-ray microscopy could be even more beneficial. Imaging techniques allow one to see what is happening inside the battery on a micron scale. In that case, it can visually show the Li ion intercalation/de-intercalation process with the corresponding particle's reaction in the material during the charge and discharge cycling. Tracking the non-active particle in the material gives an idea about capacity loss. For example, when Li goes in and out of the material, particles may crack, expand, or shrink. This means that this expansion and shrinking process is an indication of one active particle which is participating in the electrochemical reaction. If a particle doesn't change its volume while cycling, that particle is no longer active, and will contribute to capacity loss in the battery. Therefore, tracking the particle's participation pathway using X-ray imaging technique during the charge and discharge cycling will help ultimately design better materials to avoid significant capacity loss.